



Max Planck Institute
of Colloids and Interfaces



MEMBRANE ADHESION MEDIATED
via
LIPID-ANCHORED SACCHARIDES

Dissertation

zur Erlangung des akademischen Grades
Doktor der Naturwissenschaften (Dr. rer. nat.)
in der Wissenschaftsdisziplin Theoretische Physik

eingereicht an der
Mathematisch-Naturwissenschaftlichen Fakultät
der Universität Potsdam

von

Batuhan Kav

geb. 12.01.1991, Ankara/Türkei

MAX PLANCK INSTITUTE OF COLLOIDS AND INTERFACES
THEORY & BIO-SYSTEMS

Potsdam, 31.12.2018

Referees

Dr. Thomas Weikl

Dr. Emanuel Schneck

Prof. Dr. Andreas Janshoff

Oral Disputation: 03.05.2019

This work is licensed under a Creative Commons License:
Attribution 4.0 International.
This does not apply to quoted content from other authors.
To view a copy of this license visit
<https://creativecommons.org/licenses/by/4.0/>

Published online at the
Institutional Repository of the University of Potsdam:
<https://doi.org/10.25932/publishup-42879>
<https://nbn-resolving.org/urn:nbn:de:kobv:517-opus4-428790>

Abstract

Membrane adhesion is a fundamental biological process in which membranes are attached to neighboring membranes or surfaces. Membrane adhesion emerges from a complex interplay between the binding of membrane-anchored receptors/ligands and the membrane properties. In this work, we study membrane adhesion mediated by lipid-anchored saccharides using microsecond-long full-atomistic molecular dynamics simulations. Motivated by neutron scattering experiments on membrane adhesion *via* lipid-anchored saccharides, we investigate the role of LeX, Lac1, and Lac2 saccharides and membrane fluctuations in membrane adhesion.

We study the binding of saccharides in three different systems: for saccharides in water, for saccharides anchored to essentially planar membranes at fixed separations, and for saccharides anchored to apposing fluctuating membranes. Our simulations of two saccharides in water indicate that the saccharides engage in weak interactions to form dimers. We find that the binding occurs in a continuum of bound states instead of a certain number of well-defined bound structures, which we term as "diffuse binding".

The binding of saccharides anchored to essentially planar membranes strongly depends on separation of the membranes, which is fixed in our simulation system. We show that the binding constants for *trans*-interactions of two lipid-anchored saccharides monotonically decrease with increasing separation. Saccharides anchored to the same membrane leaflet engage in *cis*-interactions with binding constants comparable to the *trans*-binding constants at the smallest membrane separations. The interplay of *cis*- and *trans*-binding can be investigated in simulation systems with many lipid-anchored saccharides. For Lac2, our simulation results indicate a positive cooperativity of *trans*- and *cis*-binding. In this cooperative binding the *trans*-binding constant is enhanced by the *cis*-interactions. For LeX, in contrast, we observe no cooperativity between *trans*- and *cis*-binding. In addition, we determine the forces generated by *trans*-binding of lipid-anchored saccharides in planar membranes from the binding-induced deviations of the lipid-anchors. We find that the forces acting on *trans*-bound saccharides increase with increasing membrane separation to values of the order of 10 pN.

The binding of saccharides anchored to the fluctuating membranes results from an interplay between the binding properties of the lipid-anchored saccharides and membrane fluctuations. Our simulations, which have the same average separation of the membranes as obtained from the neutron scattering experiments, yield a binding constant larger than in planar membranes with the same separation. This result demonstrates that membrane fluctuations play an important role at average membrane separations which are seemingly too large for effective binding. We further show that the probability distribution of the local separation can be well approximated by a Gaussian distribution. We calculate the relative membrane roughness and show that our results are in good agreement with the roughness values reported from the neutron scattering experiments.

Zusammenfassung

Membranadhäsion ist ein fundamentaler biologischer Prozess, bei dem Membranen sich an benachbarte Membranen oder Oberfläche anheften. Membranadhäsion entstammt einem komplexen Zusammenspiel aus Bindungen zwischen Membranverankerten Rezeptor/Ligand-Bindungen und den Membraneigenschaften selbst. In dieser Arbeit untersuchen wir Membranadhäsion vermittelt durch Lipid-verankerte Saccharide mittels Mikrosekunden-langer voll-atomistischer molekular-dynamischer Simulationen. Motiviert durch Neutronen Scattering Experimente von Lipid-verankerten Sacchariden und deren Einfluss auf Membranadhäsion, untersuchen wir die Rolle der Saccharide LeX, Lac1 und Lac2 sowie der Membranfluktuationen in Membranadhäsion.

Wir untersuchen die Bindungen der Saccharide in drei verschiedenen Systemen: In Wasser, verankert in quasi-ebenflächigen Membranen bei fixierten Abständen, und verankert in aneinanderaliegenden, fluktuierenden Membranen. Unsere Simulationen von zwei Sacchariden in Wasser deuten darauf hin, dass diese Saccharide durch schwache Interaktionen Dimere formen. Anstelle einiger klar definierter Bindungsstrukturen, finden wir ein Kontinuum von gebundenen Zuständen vor, das wir als "diffuse Bindung" bezeichnen.

Die Bindungen von Sacchariden in quasi-ebenflächigen Membranen hängt stark vom Abstand zwischen diesen Membranen ab, der in unserem System fest gewählt ist. Wir zeigen, dass die Bindungskonstanten für *trans*-Interaktionen zweier Lipid-verankerter Saccharide monoton abnimmt mit zunehmendem Abstand. Saccharide verankert auf der selben Membran wechselwirken in *cis*-Interaktionen, deren Bindungskonstanten denen der *trans*-Interaktionen bei dem kleinsten gewählten Membranabstand ähneln. Das Zusammenspiel der *cis*- und *trans*-Interaktionen kann in Simulationssystemen mit vielen Lipid-verankerten Sacchariden untersucht werden. Für Lac2 deuten unsere Simulationen auf eine Kooperativität zwischen *cis*- und *trans*-Interaktionen hin: In diesem kooperativen Bindungsprozess verstärkt die *cis*-Interaktion die *trans*-Bindungskonstante. Für LeX hingegen stellen wir keine Kooperativität zwischen *trans*- und *cis*-Bindung fest. Zusätzlich bestimmen wir die generierten Kräfte, die durch *trans*-gebundene Lipid-verankerte Saccharide in ebenflächigen Membranen und die resultierende Ablenkung der Lipid-Anker hervorgerufen werden. Wir stellen fest, dass mit gesteigertem Abstand zwischen den Membranen, die auf *trans*-gebundene Saccharide wirkenden Kräfte auf bis zu 10 pN ansteigen.

Die Bindungen von Sacchariden, die in fluktuierenden Membranen verankert sind, resultieren aus einem Zusammenspiel zwischen den Eigenschaften dieser Lipid-verankerten Saccharide und den Membranfluktuationen. Unsere Simulationen, die den Membranabstand aufweisen, der auch in den Neutron Scattering Experimenten ermittelt wurde, resultieren in einer Bindungskonstante, die größer ist als jene in quasi-ebenflächigen Membranen bei dem gleichen Abstand. Dieses Ergebnis demonstriert, dass Membranfluktuationen eine wichtige Rolle spielen bei mittleren Membranabständen, die sonst scheinbar zu groß sind für effektive Bindungsprozesse. Weiterhin zeigen wir, dass die Wahrscheinlichkeitsverteilung der lokalen Abstände gut durch eine Gauss-Verteilung approximiert werden kann. Wir berechnen die relative Membranrauigkeit und zeigen, dass unsere Ergebnisse gut mit denen der Neutron Scattering Experimente vereinbar sind.

Acknowledgements

Within the scope of this thesis, I first would like to thank my supervisor Dr. Thomas Weikl for his supervision of this work and his contributions to my thesis. I thank my second supervisor Dr. Emanuel Schneck for the insightful discussions, the extension he provided, and the experimental data. I thank Dr. Mark Santer for his help in developing the RESP charge fitting protocol, Dr. Andrea Grafmüller for sparking the initial idea for the reparametrization of the AMBER Lipid14 force field, Dr. Jörg Sauter for allowing me to use modified Glycam06 parameters ahead of publication. I further thank Dr. Joao Robalo for providing me the scripts for the RESP charge fitting and enlightening discussions. I appreciate long and insightful discussions with Dr. Markus Miettinen on the membranes and simulations. I would like to acknowledge the help from Melis Göktaş and Katarzyna Ziolkowska for their help with the figures. I am grateful to Tara Schmitz for her critical reading of this thesis. I further acknowledge the funding from International Max Planck Research School on Multiscale Biosystems. I also thank Susann Weber, Angelina Schneider, and all the other MPIKG staff for helping me with the bureaucracy.

Beyond the scope of this thesis, I would like to thank all my friends (luckily too many to fully name here) for their constant help and support. In particular, I would like to thank Eleanor Ewins, Nadin Haase, Melis Göktaş, Prithvi Raj Pandey, Mehmet Can Uçar, Oliver Späker, Agnese Codutti, Markus Miettinen, Tania Cardoso and Joao Robalo for making my three years here almost home. My lifetime friends Ersun Sözen, Tolga Cerrah, Imre Özbay, Erdem Dur-sunkaya and Yalin Gürçan, I am grateful to you all for creating unforgettable memories. I also would like to thank Tara Schmitz with my whole heart for bearing with me throughout this writing process.

Last but not least, I present my sincere gratitude and love to my family, who have always supported me from my first day to this day. Needless to say, I wouldn't be here if it wasn't for them.

I can hardly contain myself.

Rajin Thunderkeg

Contents

1	Introduction	1
1.1	Interactions of membranes <i>via</i> saccharides	1
1.2	Molecular dynamics simulations of membranes and saccharides	4
1.3	Binding constants of membrane-anchored molecules	7
1.4	Overview of this thesis	9
2	Simulation Methods	11
2.1	Simulations of saccharides in water	11
2.2	Parametrization of MD Force Fields for saccharides and membranes . . .	13
2.2.1	Parametrization of AMBER Lipid14 Force Field for TIP5P Water Model	13
2.2.2	RESP charge fitting for the glycolipid linker	17
2.3	Simulations of lipid-anchored saccharides	19
3	Binding of saccharides in water	26
3.1	Conformations of soluble saccharides	26
3.2	Binding of soluble saccharides	29
3.3	Summary	37
4	Binding of saccharides anchored in planar membranes	38
4.1	<i>Trans</i> -binding	40
4.2	<i>Cis</i> -binding	46
4.3	Coupling of <i>trans</i> - and <i>cis</i> -binding	53
4.4	Summary	61
5	Binding of saccharides anchored in apposing fluctuating membranes	63
5.1	Membrane fluctuations and the relative membrane roughness	67
5.2	Binding of lipid-anchored saccharides	71

5.3	Saccharide concentrations at different local separations	75
5.4	Summary	76
6	Forces on <i>trans</i>-bound saccharides in membrane adhesion	78
6.1	Harmonic modeling of forces and energies in <i>trans</i> -binding	79
6.2	Forces and energies in <i>trans</i> -binding of lipid-anchored saccharides in planar membranes	83
6.3	Summary	90
Appendix A Parametrization of MD Force Fields for Saccharides and Membranes		93
A.1	Parametrization of Amber Lipid14 Force Field for TIP5P Water Model .	93
A.2	Assigning Point Charges for the Glycolipid Linker	98
Appendix B Simulations of saccharides and membranes		104
B.1	Simulations of saccharides in water	104
B.2	Simulations of lipid-anchored saccharides	105
B.2.1	Simulations of lipid-anchored saccharides in planar membranes . .	105
B.2.2	Simulations of lipid-anchored saccharides in apposing fluctuating membranes	107
Appendix C The correlation length and time of the apposing fluctuating bilayer simulations		108
Bibliography		111
List of Figures		121
List of Tables		125

Chapter 1

Introduction

1.1 Interactions of membranes *via* saccharides

Every living cell is separated from their environment by a complex membrane that is known as the cell membrane. Cell membranes are primarily composed of a lipid bilayer with amphiphilic phospholipids that have both hydrophilic head groups (for instance phosphate head groups) and hydrophobic tails. Cell membranes typically contain more than one type of phospholipids, as well as other lipids such as cholesterol that strengthens the bilayers.^{1,2} Besides lipid molecules, cell membranes also contain embedded molecules such as proteins and saccharides. Cell membranes are included in variety of cellular processes, ranging from signal transduction and ion conductivity to transportation of molecules from outside of the cell to the interiors.³ Different compositions of the cell membranes with different embedded molecules allow such versatile functions to be performed by the cell membranes.

Saccharides are a major class of biomolecules. In living systems, they are involved in a wide range of functions such as cell-cell recognition, growth, post-translational modifications of proteins, and blood anti-coagulation.⁴ From a structural point of view, saccharides form major structural element of the cell wall. The glycocalyx, which is also known as the pericellular matrix, is composed of glycoproteins and glycolipids and covers the cell membranes of some bacteria and epithelium cells. The saccharide portion of the glycocalyx contributes to cell-cell recognition and cell adhesion.^{5,6} In cell adhesion where the cells attach and interact with surfaces or other cells, saccharides most often serve as ligands for lectins.⁷

Membrane-anchored saccharides are involved in cellular recognition processes and immune responses.⁸ In terms of membrane adhesion, the most prevalent function of the membrane-anchored saccharides is to act as a ligand for the cell-adhesion molecules, in particular for lectins.⁹ On the other hand, there is accumulating experimental evidence in

the literature that shows the saccharide-saccharide interactions also can mediate membrane adhesion. For instance, blood antigen Lewis-X,¹⁰ glycosphingolipid GM3¹¹ and other saccharides¹² have shown to be involved in saccharide mediated membrane adhesion. Due to their importance in overall adhesion process, it is important to have a molecular understanding of the binding of saccharides.

Lewis-X (LeX)^{13,14} is a trisaccharide ($\text{Gal}\beta(1\rightarrow 4)[\text{Fuc}\alpha(1\rightarrow 3)]\text{GlcNAc}\beta$) that is most commonly found on cell membrane glycolipids and glycoproteins. Membrane-anchored LeX mediates cell-cell interactions, adhesion,¹⁵ and cellular recognition processes¹⁶ *via* homophilic interactions. Promoting cell adhesion in early embryonic stages¹⁷ and mediating metastasis of cancer cells¹⁰ are two examples of its wide biological function.

Because of its biological importance, LeX has been studied widely. X-ray crystallography and computational studies have shown that LeX has a rigid structure and predominantly exists in a single conformation.¹⁸ This is mainly due to the close packing of the galactose and fucose residues. As LeX is a small molecule, its binding properties in solution are not entirely clear. Several computational studies suggested that binding of two LeX molecules in solution has at least four bound states and the presence of calcium ions affect the binding constant.^{19,20} The binding constant of soluble LeX has been estimated to be at very low affinity²¹ although these results did not get published. The role of LeX in membrane adhesion has been studied by atomic force microscopy and binding essays with immobilized LeX on gold nanoparticles²² and lipid vesicles.^{23,24} Such studies have shown that LeX can mediate membrane adhesion *via* homophilic interactions, albeit the forces and the binding energies are generally in the order of piconewtons and a few $k_B T$.

The primary experimental study that motivates this thesis comes from the neutron scattering experiments on the solid-supported membrane stacks doped with the lipid-anchored LeX.²⁵ In this particular setup, the membranes are fluctuating due to the thermal excitations and free to adjust their periodicity (distance between apposing membranes) by the uptake of water. In these experiments, the authors have studied the membrane adhesion mediated by the lipid-anchored LeX using specular and off-specular neutron scattering. In the experimental setup, they have varied both the molar fraction of the lipid-anchored LeX measured the lamellar periodicity (the average separation between the apposing membranes). They have used DPPC lipids for the membranes, and performed their experiments at 333 K to ensure that the membranes are in liquid-disordered state. Their results have shown that the lamellar periodicity strongly depends on the molar fraction of the lipid-anchored LeX: increasing molar concentration of the lipid-anchored LeX results in the lamellar periodicity to converge to ≈ 7.7 nm (the resolution of the experiments were a few Ångstrom). For instance, without the presence of lipid-anchored LeX and ions, DPPC bilayers have an average separation 6.5 nm which increases to 7.7 nm at 10% mol concentration lipid-anchored LeX. Increasing the concen-

tration of the lipid-anchored LeX beyond this concentration does not change the average separation from 7.7 nm. This result is important because it shows that the apposing membranes are cross-linked by the *trans*-homophilic interactions between the lipid-anchored LeX. Furthermore, these results suggest that at 7.7 nm average separation, the repulsive interactions like undulation and hydration repulsion, repulsions between the lipid-anchored saccharides and the membranes, and attractive interactions due to the binding of lipid-anchored saccharides are equal to each other. In the same work, the authors used a continuum mechanical model to describe the fluctuations of the interacting membranes and experimentally determined the membranes' bending rigidity and interaction parameters. Furthermore, the authors provided a framework from which the relative membrane roughness can be calculated. Overall, the neutron scattering experiments suggests that lipid-anchored LeX can mediate membrane adhesion.

The ability to mediate membrane adhesion *via* homophilic interactions is not limited to LeX only. In a subsequent set of experiments, E. Schneck *et.al.* studied the the average separation of DPPC membrane stacks doped with lipid-anchored Lac1 (also known as lactose/milk sugar $\text{Gal}\beta(1\rightarrow 4)\text{Glc}\beta$)²⁶ and Lac2²⁷($\text{Gal}\beta(1\rightarrow 4)\text{Glc}\beta(1\rightarrow 3)\text{Gal}\beta(1\rightarrow 4)\text{Glc}\beta$) using neutron scattering*. They have observed that, similar to the lipid-anchored LeX, both Lac1 and Lac2 can alter the average separation of pure DPPC bilayers. For the lipid-anchored Lac2 and Lac1 at 10% mol concentration, the observed average separations are 7.0 nm and 6.5 nm, respectively. At larger lipid-anchored Lac2 and Lac1 concentration, the average separations converged to 7.0 nm and 6.5 nm, respectively. Different responses of the lipid-anchored LeX, Lac1, and Lac2 to changing ion concentrations observed in the experiments are beyond the scope of this thesis.

Overall, neutron scattering experiments on membrane stacks doped with lipid-anchored saccharides show that lipid-anchored saccharides can cross-link the membranes. The average separation of the membrane stacks and its response to different experimental conditions (changing salt concentration, for instance) depend on the structure of the lipid-anchored saccharides.

This thesis is motivated by the neutron scattering experiments on lipid-anchored saccharides. Our aim is to provide a molecular description for the membrane adhesion mediated *via* lipid-anchored saccharides and understand how the binding properties of the lipid-anchored saccharides and the membrane fluctuations mediate the membrane adhesion. In particular, we are studying the binding properties of soluble LeX, Lac1, and Lac2. When anchored to the membranes, we are analyzing the binding of lipid-anchored LeX and Lac2. Our main tool to study these system is full-atomistic molecular dynamics simulations.

*Unpublished results obtained through personal communication. Experiments have been performed at Institut Laue-Langevin, France with ID TEST-1655

1.2 Molecular dynamics simulations of membranes and saccharides

Biological processes, from the electron transfer chain to cell division, span a wide range of time and length scales. Rapid processes occurring at short length scales are where molecular level interactions take place. For instance, the binding of lipid-anchored saccharides studied in this work occurs at the length scale of a few nanometers and has a lifetime is in the order of a few hundreds of picoseconds. These very short time and length scales, unfortunately, are not easy to study experimentally. At this point, computer simulations can provide invaluable information on the dynamics of the system under study.

Molecular dynamics (MD) is a computational method to study the physical movements of atoms and molecules. The most common version of MD is the classical molecular dynamics, in which the movements (or trajectories) of atoms and molecules are studied by numerically solving the Newton's equations of motion. The main assumption of classical MD is that the system under study can be well approximated by a classical treatment: atoms are hard spheres with localized point (i.e. partial) charges and the dynamics follow the classical (Newton's) equations of motion. Quantum mechanical effects, such a delocalized charges because of the atomic or molecular orbitals are *implicitly* taken into account in the simulation parameters, but no quantum mechanical description of the time-evolution of the system is considered.

In order to use Newton's equations of motion, one needs to know the forces acting between the atoms in the system. The forces are derived from a potential function that contains the considered types and the strengths of the interactions. These interactions are typically divided into two categories: the bonded interactions stem from the existence of chemical bonds and include the vibrations alongside the bond, fluctuations within the bond angle, and the torsions generated by the dihedral angles. The non-bonded interactions form the second category where the physical interactions come from the charges on or sizes of the atoms.

The set of parameters that define the potential energy function is known as the force field. As all the interactions are derived from the force field, it is of utmost importance in the accuracy of the molecular dynamics simulations. In the literature, there are many force fields for the MD simulations, ranging from coarse grained (where atoms and molecules are combined to form larger beads) to full-atomistic (in which all of the atoms are explicitly presented). Moreover, there are different force fields optimized for different biomolecules: for instance, some force fields only define the lipids whereas some focus only on saccharides. To date, unfortunately, there is no single force field that includes all of the biomolecules with very high accuracy.

In this work, we have combined two full-atomistic force fields, namely the AMBER Lipid14²⁸ force field for the lipids and the Glycam06²⁹ force field for the saccharides and the TIP5P³⁰ water model for the solvent. In the following, we will shortly discuss the general properties of these force fields.

AMBER (Assisted Model Building with Energy Refinement) is a family of force fields that have been developed to study the biomolecules (proteins, lipids, and carbohydrates) at molecular level using MD simulations. It has been under constant refinement and development since the late 1970's and is one of the most popular force field family that is being used in full-atomistic MD simulations of biomolecules.

The AMBER force field assumes the following functional form when calculating the potential energy within the system

$$\begin{aligned}
 V(r^N) = & \sum_{bonds} k_b(l - l_0)^2 + \sum_{angles} k_a(\theta - \theta_0)^2 \\
 & + \sum_{torsion} \sum_n \frac{1}{2} V_n [1 + \cos(n\omega - \gamma)] \\
 & + \sum_{j=1}^{N-1} \sum_{i=j+1}^N f_{ij} \left\{ \epsilon_{ij} \left[\left(\frac{r_{0ij}}{r_{ij}} \right)^{12} - 2 \left(\frac{r_{0ij}}{r_{ij}} \right)^6 \right] + \frac{q_i q_j}{4\pi\epsilon_0 r_{ij}} \right\}
 \end{aligned} \tag{1.1}$$

The first term in the Eq. 1.1 corresponds to the energy between covalently bonded atoms. The second term is the summation over angles and represents the energy involved due to the geometry of the covalent bond. The third term (summing over torsions) is the energy contribution from the torsion angles. The fourth term corresponds to the non-bonded energy in the system and is calculated between all atom pairs. The double sum over i, j in the fourth term can further be decomposed into the van der Waals interactions (with ϵ_{ij}) and the electrostatic energies.

The AMBER force field contains all the parameters (namely $k_b, k_a, \epsilon_{ij}, q_i$ and r_{0ij}) for all possible atoms required to calculate the potential energy in Eq. 1.1 for a given time-step. All of these parameters are calculated using different quantum mechanical models and then further refined to reproduce experimental data.

AMBER Lipid14 force field is initially developed for the accurate description of the lipids. It has been designed to be consistent and compatible with the other AMBER force fields, so that different AMBER force fields can be used simultaneously to describe more complicated systems than of simple lipids or proteins. AMBER Lipid14 forcefield (with its next iteration AMBER Lipid17) allows the full-atomistic MD simulations of lipids with phosphocholine (PC), phosphatidylserine (PS), phosphatidylethanolamine (PE), and phosphatidylglycerol (PG) head groups and cholesterol.

AMBER Lipid14 force field is a common force field used in the MD simulations of

lipid bilayers. For the lipids with mentioned head groups, it correctly reproduces the liquid ordered/disordered phase transition of the lipid membranes. Furthermore, it reproduces the experimental area per lipid, isothermal compressibility modulus, tail order parameters, and X-ray scattering factors accurately. On the other hand, it fails to reproduce head group order parameters, especially the structure of the glycerol backbone that connects lipid head groups to the tails. Furthermore, it predicts the response of the lipid head groups to the binding of ions inaccurately. The limitations of the structural predictions of AMBER Lipid14 force field has been discussed elsewhere.^{31–33} Despite its limitations, AMBER Lipid 14 force field is widely used in MD simulations of lipid bilayers.

The Glycam06 force field has been designed as a full-atomistic force field for the saccharides (although same parameters can be used to design small molecules as well). It is developed to be a complete force field for the saccharides, that is all available saccharides, regardless of simple monosaccharides or complex oligosaccharides, can be modeled within the parameter set provided by the Glycam06 force field. As a continuation of its predecessors, Glycam06 force field improves on the gas-phase properties of small saccharides, diffusion coefficients and the rotamer populations of the soluble saccharides. Furthermore, Glycam06 force field has been developed to be compatible with AMBER family of force fields.

Both AMBER and Glycam06 force fields have originally been developed with the TIP3P water model,³⁴ which is a rigid (fixed bond lengths between O and H atoms) water model with three interaction sites. As TIP3P is one of the simplest water model and have exact analytical equations to calculate its interactions,³⁵ usage of TIP3P within the simulations decrease the computational costs greatly. It is important to note that, all force fields depend very sensitively on the water model used. Therefore, one should always avoid using a different water model than the original one used in the parametrization of the force field.

In 2015, Sauter and Grafmüller showed that many of the available force fields for saccharides underestimate the osmotic pressure of soluble saccharides in TIP3P water model.³⁶ The reason behind such a behavior is that all of the studied force fields are overestimating the interactions between the saccharides in water. Sauter and Grafmüller further showed that Glycam06 using TIP5P water model (another rigid water model with five interaction sites) is the best available model (albeit the osmotic pressure is still underestimated) for the full-atomistic MD simulations of saccharides. In their following work, Sauter and Grafmüller proposed a new force field, developed by carefully adjusting the Lennard-Jones parameters of the saccharide atoms (the double sum over i, j in Eq. 1.1) that reproduces the osmotic pressure of small saccharides in water accurately.³⁷

The most important interactions in the MD simulations presented in this thesis are the saccharide-saccharide interactions. Therefore, in order to capture such interactions

as accurately as possible, we use the Glycam06 force field with Sauter and Grafmüller parameters with the TIP5P water model.

1.3 Binding constants of membrane-anchored molecules

Biological processes, from signal transduction to adhesion, involve the binding of soluble or membrane-anchored molecules. An important question in membrane adhesion is to quantify the binding affinity of the membrane-anchored molecules as many biological responses depends on the differences in the binding affinities of the different membrane-anchored molecules.³⁸

In solution the binding affinity of the receptors and ligands are given by the three-dimensional binding constant K_{3D}

$$K_{3D} = \frac{[RL]_V}{[R]_V[L]_V} \quad (1.2)$$

where $[RL]_V$, $[R]_V$, and $[L]_V$ correspond to the volume concentrations of the bound receptor-ligand complexes, and the unbound receptors and ligands, respectively. Eq. 1.2 holds valid for large concentrations of the receptors and ligands and can be measured using experimental methods like surface plasmon resonance³⁹ and nuclear magnetic resonance.⁴⁰ When the concentrations of the receptors and ligands are small (a few receptors and ligands), Eq. 1.2 no longer holds but an equivalent description for the K_{3D} can be written as³⁸

$$K_{3D} = V \frac{P_b}{P_u} \quad (1.3)$$

where V , P_b , and P_u are the volume of the system, probability of being bound and unbound, respectively. P_b and P_u are further related to the kinetic *on*- and *off*-rates (k_{on}, k_{off}) via $P_b = V k_{on}$ and $P_u = 1 - P_b = k_{off}$. The kinetic *on*- and *off*-rates determine the transition rates from unbound to bound, and bound to unbound receptors and ligands, respectively.

When the receptors and ligands are anchored to the membranes, the binding affinity is given by the two-dimensional binding constant K_{2D} . In line with Eq. 1.2, K_{2D} is often assumed to be

$$K_{2D} = \frac{[RL]_A}{[R]_A[L]_A} \quad (1.4)$$

where $[RL]_A$, $[R]_A$, and $[L]_A$ are the surface (area) concentrations of the receptor-ligand complexes, receptors, and ligands, respectively.⁴¹ Eq. 1.4 implies a linear relationship between the concentrations of the bound and unbound receptors and ligands. The binding of membrane-anchored receptors and ligands can be experimentally investigated by fluorescence methods,⁴² hydrodynamic flow,⁴³ and micropipette setups.⁴⁴ However, different experimental methods on similar systems have reported binding constants differing by

orders of magnitude.⁴⁵ These differences in the experimental results suggest that the binding constant K_{2D} does not only depend on the nature of the receptors and ligands, but also on the membrane properties.⁴⁶

The relation between the properties of the membranes and the binding of the membrane-anchored receptors and ligands have been studied in the literature.^{47, 48, 48, 49} Using a discretized elastic surface model for the membranes, for instance, it has been shown that the two-dimensional binding constant depends on the local separation l between the apposing membranes and the relative membrane roughness ξ_{\perp} .^{46, 50} The dependency of two-dimensional binding constant K_{2D} on local separation and relative membrane roughness can be understood as follows: due to the membrane fluctuations, the distance between apposing membranes both temporarily and spatially change. If the local separation is too large compared to the lengths of the receptors and ligands, the binding will not occur as the receptors and ligands will not "see" each other. On the other hand, if the local separation is too small, the steric repulsions between membranes and the receptors/ligands will disfavor the binding. The relative membrane roughness, which is defined as the standard deviation of the probability distribution of the local separation, specifies the magnitude of the membrane fluctuations. When the membrane-anchored receptors and ligands bind, they have to hold the membranes against the thermal fluctuations. In the membrane adhesion zones, the binding of receptors and ligands result in a decrease of the membrane roughness as the receptor-ligand bonds confine the membrane fluctuations and therefore reduces the entropy of the membrane. Moreover, the reduction in the membrane roughness at binding zones due to the binding of receptors and ligands "smoothens" out the membranes and favors the binding of additional receptors and ligands.⁵¹ The overall outcome of this behavior is the positive cooperativity between the binding of receptors and ligands. Theoretical and computational studies have shown that, when the membrane fluctuations are present, the relation between the surface concentrations of the bound and unbound receptors and ligands follow a quadratic relation $[RL]_A \propto [R]_A^2 [L]_A^2$. This quadratic relation implies that the two-dimensional binding constant is in fact not a constant but depends on the concentrations of the receptors and ligands.

In the presence of membrane fluctuations, we can decompose the K_{2D} into individual $K_{2D}(l)$ values which are measured at different local separations l . We can describe the local separation l with a probability distribution $P(l)$. Then, K_{2D} and $P(l)$ can be combined into a single equation to calculate K_{2D} as

$$K_{2D} = \int K_{2D}(l)P(l)dl \quad (1.5)$$

where the integral is calculated over all possible local separations l .⁴⁶ We can understand Eq. 1.5 as follows: at each local separation l , the binding constant will have a value of $K_{2D}(l)$ with a probability of observing that local separation $P(l)$. Therefore, the bind-

ing properties of the receptors and ligands at a given local separation l is included in $K_{2D}(l)$. On the other hand, the membrane properties like average separation \bar{l} between the apposing membranes ($\bar{l} = \langle P(l) \rangle$) and relative membrane roughness ξ_{\perp} , which is the standard deviation of $P(l)$, are included in $P(l)$. As the experiments on membrane adhesion generally result in time and space averaged quantities, in equilibrium, Eq. 1.5 corresponds to the experimentally observed binding constant.

1.4 Overview of this thesis

In this thesis, motivated by the neutron scattering experiments on membrane adhesion *via* lipid-anchored LeX and Lac2, we are trying to provide a molecular description of the binding of the lipid-anchored saccharides in membranes. Our primary aim is to understand the binding properties of soluble and lipid-anchored saccharides and analyze the relation between the membrane fluctuations and the binding of lipid-anchored saccharides using full-atomistic molecular dynamics simulations.

This thesis is organized as follows: in **Chapter 2** and **Appendix**, we present the details of the molecular dynamics simulations, reparametrization of the AMBER Lipid14 force field for the TIP5P water model, and RESP charge fitting for the glycolipid linker. The obtained parameters for the glycolipid linker and reparametrized POPC force field for TIP5P water model are then used in the simulations of the membrane-anchored saccharides.

In **Chapter 3**, we study the binding of soluble saccharides. We discuss their equilibrium conformations and their changes due to binding. We further study the structures of the bound states and report the binding constants for the soluble saccharides. The main results on the structures of the bound states are primarily important for the understanding of the binding of the lipid-anchored saccharides.

In **Chapter 4**, we study the binding of lipid-anchored saccharides at fixed membrane separations. We first determine the *trans*- and *cis*- binding constants of isolated pairs of lipid-anchored saccharides. We next investigate the coupling between *cis*- and *trans*-interaction in membrane systems with many lipid-anchored saccharides. For each system, we report the binding constants.

In **Chapter 5**, we consider the binding of the lipid-anchored LeX in apposing fluctuating membranes. We first discuss the membrane fluctuations and the relative membrane roughness. We then determine the binding constant for the lipid-anchored LeX in apposing fluctuating membranes. Finally, we analyze the correlations between the lateral positions of the lipid-anchored saccharides and the local separation between the apposing fluctuating membranes.

In **Chapter 6**, we determine the forces generated by *trans*-binding of lipid-anchored

saccharides in planar membranes from the binding-induced deviations of the lipid-anchors. We discuss the validity and range of the model, and report the forces for the planar membrane systems presented in Chapter 4.

Chapter 2

Simulation Methods

Molecular dynamics (MD) is a computational method to study the physical movements of atoms and molecules. The most common version of MD is the classical molecular dynamics, in which the movements (or trajectories) of atoms and molecules are studied by numerically solving the Newton's equations of motion. MD is a powerful tool for studying the motions of the atoms and molecules as one can obtain Ångstrom resolution "video" of the system at femtosecond timescale which is not readily accessible through the experiments. In this thesis, we are using full-atomistic classical molecular dynamics simulations as our primary tool to study the binding of lipid-anchored saccharides.

In this chapter, we provide the details of our MD simulations. This chapter is organized as follows: we first provide the details of the simulations of saccharides in water. Then, we present our reparametrization scheme for AMBER Lipid14 force field, and discuss the RESP charge fitting protocol for obtaining the point charges on the glycolipid linker. Finally, we present the details of our simulations with lipid-anchored saccharides in planar and fluctuating membranes.

2.1 Simulations of saccharides in water

We simulate LeX, Lac1, and Lac2 saccharides (Fig. 2.1) in water to study their binding properties without any confinement due to a membrane.

The Glycam06h force field²⁹ has been developed as a self-consistent full set of parameters for the simulations of biomolecules with a special focus on saccharides. It is one of the most widely used force field for saccharides as it is designed to be applicable to simple monosaccharides as well as complex oligosaccharides, be usable for all saccharide sizes and ring conformations, and be self contained such that it can be used with other MD force fields. It contains the full-set of parameters that can be used for modeling any saccharide. Glycam06h force field provides one set of parameters each for the TIP3P and

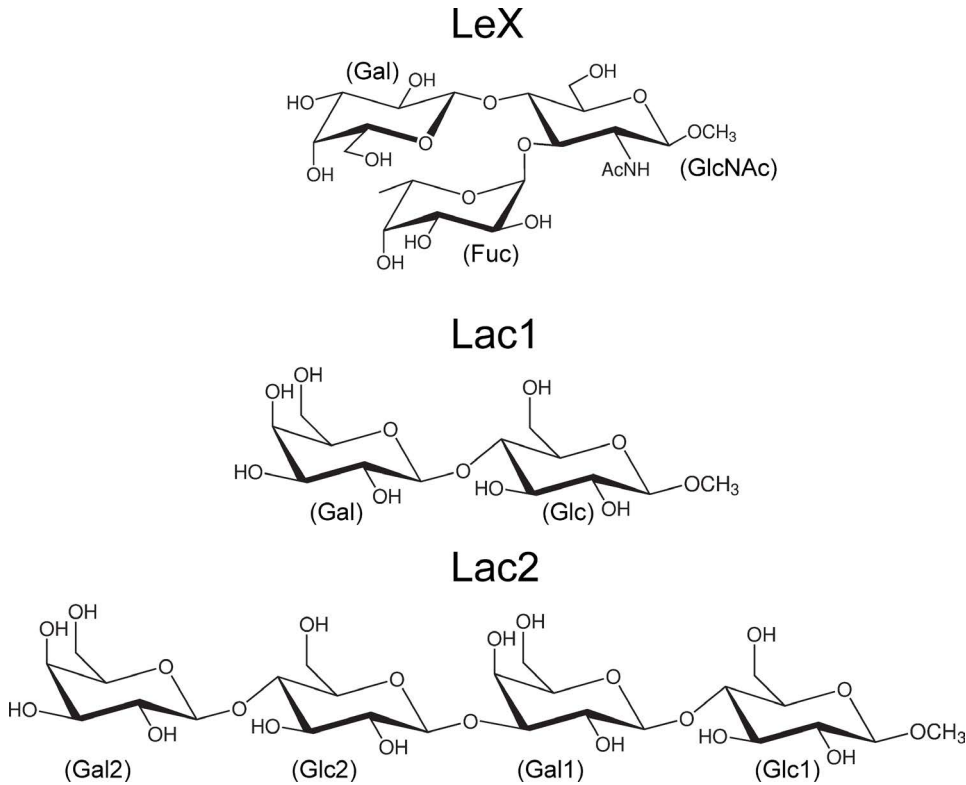


Figure 2.1: Structures of the simulated saccharides. LeX (top), Lac1 (middle), and Lac2 (bottom). Residue names are also labeled.

TIP5P water models.

In 2015 Sauter and Grafmüller have compared³⁶ the available force fields for carbohydrates with respect to their solution properties such as aggregation, density, and diffusion coefficients. They have shown that Glycam06h force field with the TIP5P water model reproduces solution properties of the hemicelluloses which are a class of branched saccharides. In their following work,³⁷ they also have shown that, even though Glycam06h with the TIP5P water model is the best available force field for the full atomistic MD simulations of the saccharides, it estimates low osmotic pressure for the saccharides indicating that the saccharide-saccharide interactions are underestimated. In order to rectify this drawback, Sauter and Grafmüller introduce a scaling to the Lennard-Jones well-depth ϵ_{ij} to the nonbonded saccharide-saccharide interactions which improves on the non-modified Glycam06h force field.

In this work, as we are interested in the binding of saccharides in water and lipid-anchored systems, we would like to capture saccharide-saccharide interactions as accurate as possible. Therefore, throughout this work, we are using the Glycam06 TIP5P force field with the further modifications from Sauter and Grafmüller (Glycam06^{TIP5P}_{OSMOr14}) for the saccharides, and the TIP5P water model as the solvent.

We obtain the initial saccharide structures from Glycam Carbohydrate Builder.⁵² As

we do not want to apply any bias to the bound configurations, we choose an initial structure of two saccharides that are not interacting. After that, we perform the minimization, heating, and production steps for each saccharide to obtain μ s long trajectories (Ch. B.1).

2.2 Parametrization of MD Force Fields for saccharides and membranes

Molecular dynamics (MD) force fields are the key parameters in every MD simulation and crucial for the accuracy of the MD simulations. In this section, we describe two parametrization procedures that we have employed in this thesis: 1) parametrization of AMBER Lipid14 force field for the TIP5P water model, and 2) assigning point charges to the glycolipid linker.

2.2.1 Parametrization of AMBER Lipid14 Force Field for TIP5P Water Model

The AMBER Lipid14 force field²⁸ is one of the most popular and accurate full-atomistic force field for lipids. It has been developed using the TIP3P water model³⁴ to capture the physical and structural properties of PC lipids in the liquid-disordered phase. In order to capture saccharide-saccharide interactions the best and be compatible with Sauter-Grafmüller force field Glycam06^{TIP5P}_{OSMOr14}, we employ the TIP5P water model³⁰ throughout this work. As the force fields sensitively depend on the chosen water model, we first need to check the compatibility of Lipid14 with TIP5P water, and reparametrize the Lipid14 force field in case of incompatibilities.

Our aim in the parametrization of the Lipid14 force field is to reproduce the original Lipid14 in the TIP3P water model results for the phase, area per lipid (APL), electron density profiles, diffusion constant and order parameters of the POPC lipid (Fig. 2.2) at 303 K by adjusting the interactions between phosphatidylcholine (PC) head group atoms and the TIP5P water. As the area per lipid is the most important physical parameter that defines the phase of the membranes, we pay special attention to get the area per lipid values correctly from our reparametrization scheme. The AMBER Lipid14 force field has been shown not to reproduce glycerol order parameters in solution, as well as it predicts the wrong response against the ions in the solution.^{31,33} However, as we are simply trying to reproduce the original Lipid14 values, these limitations are expected to translate to our modified force field as well.

In order to test the compatibility of Lipid14 with the TIP5P water model, we run a set of simulations with identical initial structures, both in TIP3P and TIP5P, using the

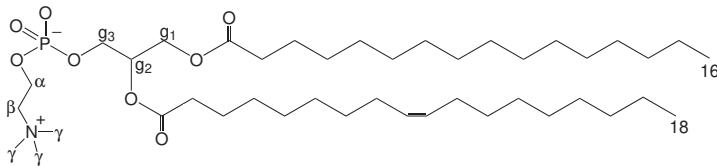


Figure 2.2: Structure of the the POPC lipid. α , β carbons and γ nitrogen and g_1 , g_2 , and g_3 are the nuclear magnetic resonance (NMR) labelings that are used to calculate head and glycerol order parameters, respectively. 16' chain is oleoyl, 18 is the palmitoyl chain of the POPC lipid.

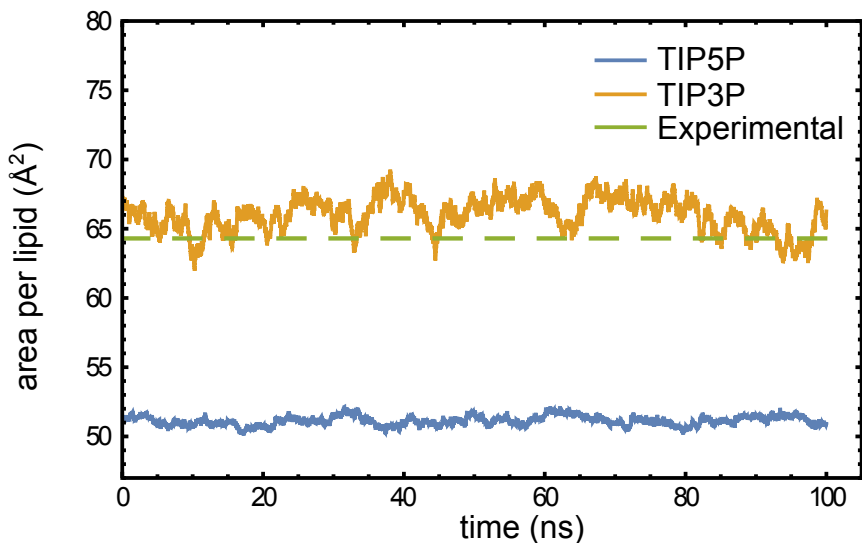


Figure 2.3: Area per lipid calculated from 100 ns simulations after 100 ns equilibration of the pure POPC in the TIP3P and TIP5P waters at 303 K. The results from the TIP3P⁵³ are in good agreement with the experiments, while the TIP5P yields very low and incorrect area per lipid values.

methods described in Ch. A.1. We calculate the APL from the simulations, and observe a large decrease in area per lipid for POPC in TIP5P at 303 K (Fig. 2.3) which is much lower than the experimental area per lipid $A_L = 64.3$.⁵³ The underlying mechanism of this behaviour is that the TIP5P water molecules tend to stay further from the PC head group (Fig. 2.4). Moreover, the overlap between the TIP5P water and the lipid tails, as well as the lipid head groups is lower than in the TIP3P water, further suggesting that the interactions between the TIP5P water and the lipid bilayer are weaker than of the TIP3P water. As a result, the TIP5P water model is not solvating the lipid bilayer fully. The reduced interactions between the TIP5P water and PC head groups result in less hydrophilic interactions and POPC lipids tend to stay closer. Very low area per lipid values in the TIP5P water shows that the AMBER Lipid14 force field is not compatible with the TIP5P water model. Therefore we reparametrize the Lipid14 force field in order to achieve compatibility with the TIP5P water model.

For the reparametrization of the Lipid14 force field, we choose to tune the well-depth

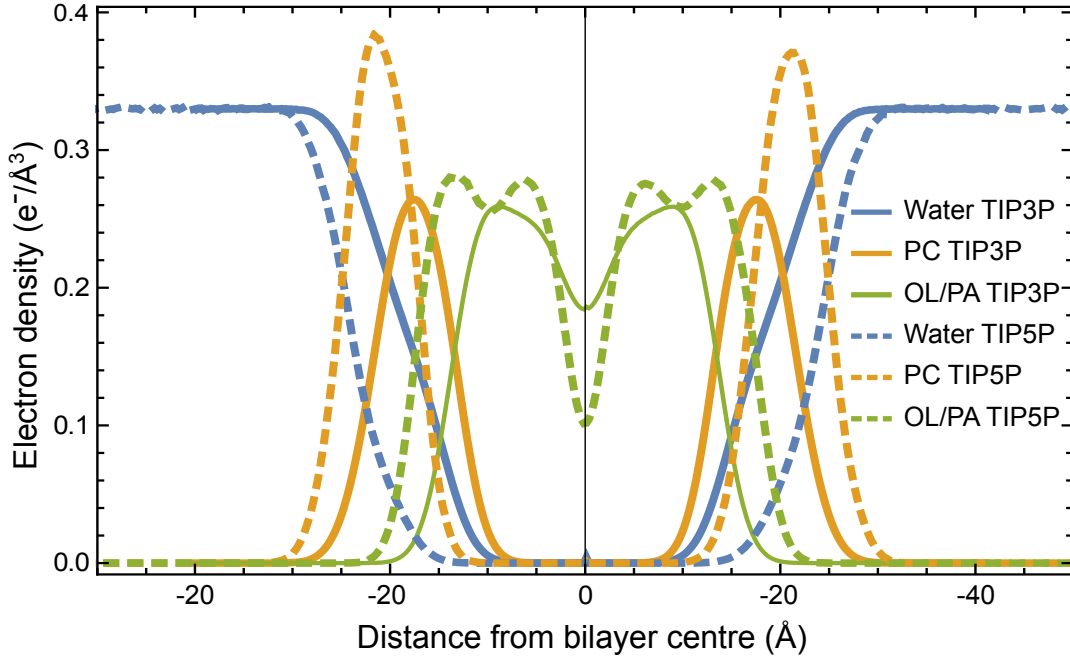


Figure 2.4: Electron density profiles along the z -axis for water, lipid head groups (PC), and lipid tail groups (PA/OL). Dashed lines represent the electron densities in the TIP5P water model. Both systems are aligned such that the center of mass of the PC head groups lie on the xy plane. Note that for the TIP5P water, the overlap between water and lipid head groups, as well as lipid tails, is much lower than of the TIP3P water.

ϵ_{ij} of the non-bonded Lennard-Jones interactions between the TIP5P water molecule and the PC head group atoms. The reason behind this choice is as follows: the electron density profiles of TIP5P water and PC head group (Fig. 2.4) shows that the TIP5P molecule is located further away from the PC head group atoms than the TIP3P. As the TIP5P oxygen atom has a smaller Lennard-Jones radius ($R_{ij} = 3.502 \text{ \AA}$) compared to TIP3P oxygen atom ($R_{ij} = 3.53 \text{ \AA}$), we do not think that the steric factors due to the atom size is the reason of this observed behaviour. We suggest that the reason why the TIP5P molecules tend to stay away from the PC head group is due to the underestimation of TIP5P-PC interactions. Therefore, we decide to alter only the Lennard-Jones well-depth ϵ_{ij} in our reparametrization. Altering the absolute value of the ϵ_i for TIP5P atoms and/or PC head group atoms would be a poor decision as such alterations will affect *all* the non-bonded interactions of the TIP5P water and PC head group atoms with saccharides, and other lipid molecules present in the system and can lead to incorrect physical values. As a result, we choose to alter only Lennard-Jones well-depth ϵ_{ij} between TIP5P water molecule and the PC head group atoms.

We apply a homogeneous scaling factor α_ϵ to the Lennard-Jones well-depth ϵ_{ij} , starting from $\alpha_\epsilon = 1.2$ to $\alpha_\epsilon = 1.55$, keeping the equilibrium distances σ_{ij} constant (Table A.1) as our initial tests with $\alpha_\epsilon = 2.0$ yielded too high area per lipid values. Remember that with this method, we are only altering lipid-water interactions to account for the

changes introduced by varying the water model from the TIP5P water to the TIP3P water model and keeping all the other interactions intact.

In order to determine which scaling factor reproduces the Lipid14 results, we first calculate the area per lipid for a given scaling factor by simply dividing the area of the box in xy -dimensions to the number of lipids per bilayer ($n_l = 64$). We observe a monotonic increase on area per lipid as a function of increasing scaling factor (Fig. 2.5). This result is expected, as with the increasing scaling factor, water-head group interactions become stronger and the lipid bilayer transitions to the liquid disordered state. Around $\alpha_\epsilon = 1.4$, we reach the original TIP3P value, which itself approximates the experimentally observed area per lipid.

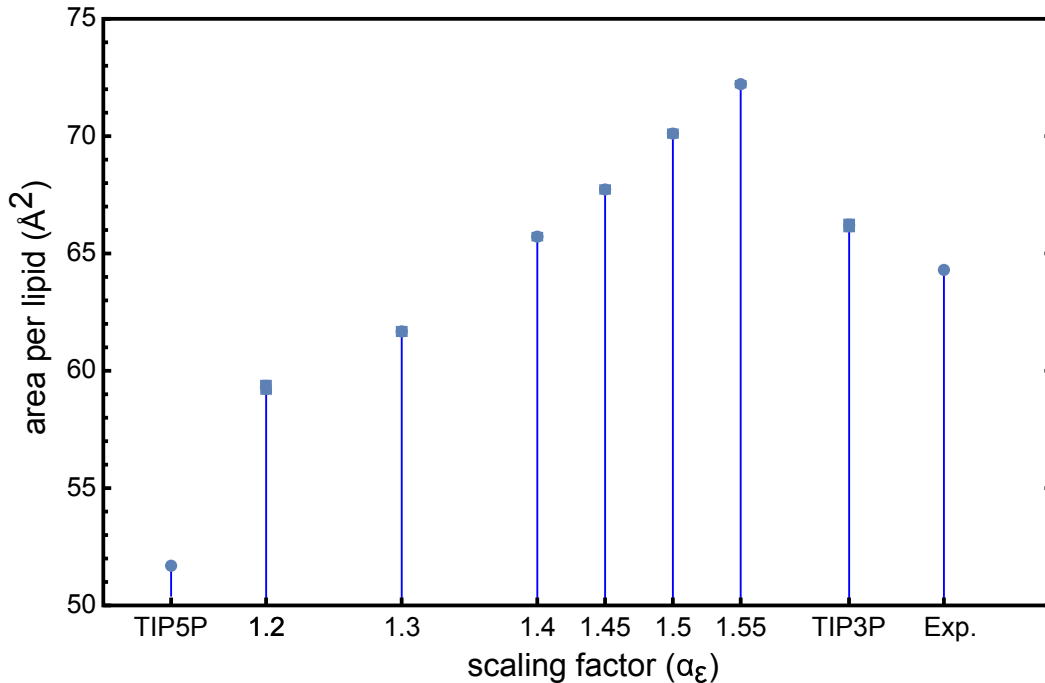


Figure 2.5: Area per lipid as a function of the scaling factor. Area per lipid values are averaged over ten independent runs. Errors in area per lipid are smaller than the bullet size.

We next consider the electron density profiles of the PC head groups and lipid tails from the simulations with different scaling factor. Although electron density profiles are not accessible through experiments, their Fourier transform knowns as the X-ray scattering factors are readily accessible by the experiments.^{54–56} We calculate the electron density profiles of the lipid head and tail groups in the direction of the membrane normal. First, we align and center the trajectories such that the center of mass of the PC head groups lie at the $z = 0$ plane, and we calculate the electron densities of PC head group and lipid tails along the membrane normal. Results are shown in Fig. 2.6. In TIP5P model, head and tail group peaks are located further away from each other than in TIP3P, indicating that the bilayer is more structured in TIP5P with lipid tails assuming

a nearly linear conformation. As the scaling factor increases, bilayer thickness (distance between PC head group peaks) decreases, and again around $\alpha_\epsilon = 1.4$, TIP3P results are reproduced.

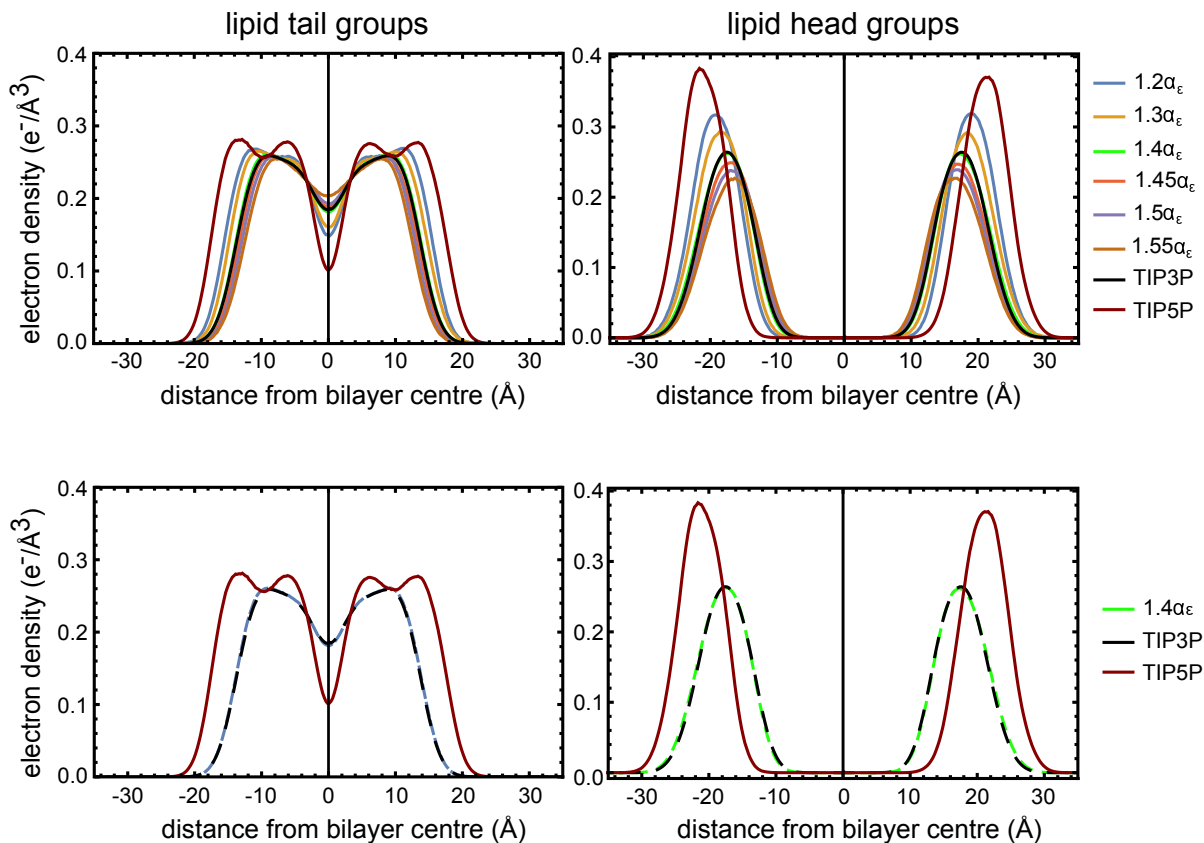


Figure 2.6: (top) Calculated electron density profiles for lipid tail and head groups. (bottom) Results for $\alpha_\epsilon = 1.4$ exhibit very good alignment with TIP3P values.

We present the results for additional parameters like volume per lipid, bilayer thickness, tail and head order parameters, and lateral diffusion constant in Ch. A.1 and show that we obtain excellent agreement between the original Lipid14 TIP3P results by using the scaling factor $\alpha_\epsilon = 1.4$ in the TIP5P water. In this work, we use the scaling factor $\alpha_\epsilon = 1.4$ with the TIP5P water model whenever we are simulating a lipid bilayer.

2.2.2 RESP charge fitting for the glycolipid linker

In MD simulations, partial atomic charges are used to calculate the electrostatic potential. For a classical non-polarizable force field, such as Lipid14, these charges are fixed and do not change throughout the simulation. In the lipid-anchored saccharides investigated in this work, there is a glycerol moiety that connects the saccharide head group to the lipid tails (Fig. 2.7). This moiety has already been parametrized in the Lipid14, as

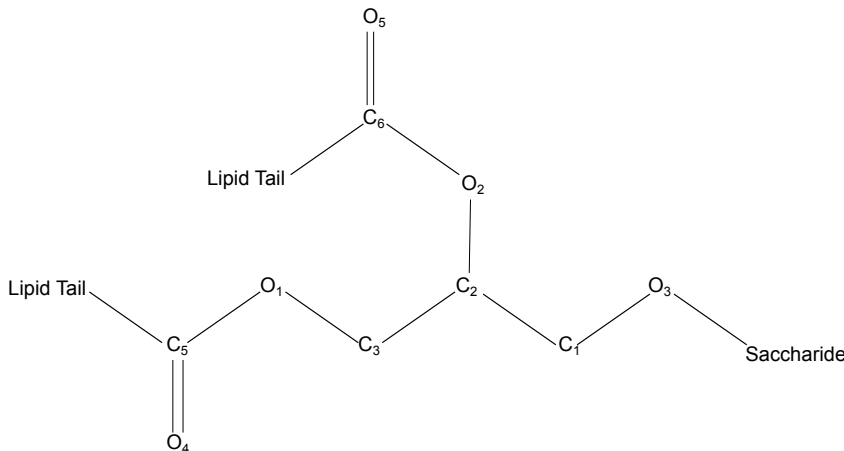


Figure 2.7: Structure of the glycolipid anchor. Non-hydrogen atoms are also labeled.

a part of the head group residue. The only difference is that in the Lipid14 the glycerol moiety is connected to the highly charged phosphate atom of the zwitterionic PC head group, whereas this moiety is connected to the neutral saccharide in the lipid-anchored saccharides. Therefore, we would expect different point charges for the same glycerol moiety in PC lipids and lipid anchored saccharides.

In order to recalculate the point charges, we apply the restrained electrostatic potential (RESP) method, along with the established AMBER protocol⁵⁷ for assigning the point charges. The RESP method inputs the molecule’s full-electronic structure that has been calculated by quantum mechanical methods, and tries to generate point-charges that creates the same quantum mechanical charge distribution. Simply, the RESP method is a way of converting a quantum mechanical continuous charge distribution into a classical discrete charge distribution.

For the RESP method, we first construct the glycolipid linker with methyl capping groups (Fig. 2.7). We minimize the structure, calculate the quantum mechanical electron distribution over the entire molecule, and feed the output structure into the RESP protocol. We use the obtained point charges to simulate glycolipid linker in TIP5P water for 100 ns. Then, we randomly select 100 conformations from the trajectory, recalculate the quantum mechanical charge distributions (without structure minimization), and refit the point charges for this ensemble of distributions (see Appendix for further details).

Our results (Table A.3) show no drastic changes to the original Lipid14 charges: our optimized partial charges do not differ drastically from the Lipid14 partial charges, which we would have used if we did not perform the partial charge optimization. The most significant differences between the observed and the original partial charges are at the $C1$, $C2$, $C3$, $O2$ and $O3$ atoms, that are closest to the carbohydrate end. As we move away from the saccharide end, we observe almost no change in the original and optimized partial charges. This behaviour is expected as the most important change to

the initial structure was to replace zwitterionic PC head group at *O1* with the neutral saccharide, and this is the part where we observe the most significant changes to the partial charges. Overall, the small differences between the optimized partial charges and the original Lipid14 charges indicate that our optimization of the partial charges has a minor effect on the overall parameter set for the linker.

For the bonded parameters, we adopt a hybrid approach. We naturally expect that the *C1*, *C2* and *O3* atoms would have bonded parameters similar to the saccharides as they are closer to the saccharide end, and other atoms in the linker would have bonded parameters close to the lipids. Therefore, for the lipid-end of the glycolipid linker we choose bonded parameters from the Lipid14 force field, and for the saccharide end we use Glycam06h bonded parameters (see Appendix for the full list of parameters). The other reason for us not to commit into the parametrization of the bonded parameters is that the parameterization of the bonded parameters is a computationally heavy task and due to the time-constraints on this project, we choose to adopt the bonded parameters from the existing ones instead of reparametrizing them. We use these optimized charges and bonded parameters for all the lipid-anchored saccharides in this work.

2.3 Simulations of lipid-anchored saccharides

We are performing full-atomistic MD simulations of lipid-anchored LeX and Lac2 saccharides (Fig. 2.9) in order to understand how the membrane adhesion depends on the binding properties of the saccharides and physical properties of the membranes. This section contains an overview of our lipid-anchored systems.

Membrane adhesion is mediated through the interactions of the lipid-anchored saccharides at the interface of two opposing membranes. The strength of adhesion depends on i) the binding strength of the lipid-anchored saccharides, ii) the local separation between opposing membranes, and iii) membrane fluctuations. The accuracy of the simulations of membrane adhesion relies on how accurately these interactions are modeled. In this work, we first consider simple systems without any membrane fluctuations at fixed local separations, and then move to more complicated systems where membrane fluctuations are also included.

In our simulations, we choose POPC lipids and 303 K temperature to construct and simulate our systems. However, in the neutron scattering experiments, the membranes contain DPPC lipids and the temperature is 333 K.²⁵ Our choice of POPC lipids and 303 K temperature can be explained as follows: the molecular dynamics force fields are very sensitive to the simulated temperature. DPPC lipids can be simulated at 333 K within the AMBER Lipid14 force field. However, the Glycam06 force field for the saccharides, and the improved force field parameters from Sauter&Grafmüller³⁷ use 303 K in their simulations. The temperature dependency of these force fields has not been

studied. Therefore, by increasing the temperature to 333 K, we cannot be sure of the accuracy of the saccharide force fields and consequently the interactions between the saccharides. As capturing the saccharide-saccharide interactions as best as possible has the utmost importance in this work, we set the simulation temperature to 303 K. From the lipid perspective, DPPC lipids are in liquid-ordered state at 303 K which means that the membrane properties differ greatly from the experimental conditions. Furthermore, the diffusion of lipid-anchored saccharides along the membrane in liquid-ordered state is completely different than in liquid-disordered state. On the other hand, the POPC lipids are in liquid-disordered state at 303 K, which allows the diffusion of the lipid-anchored saccharides and ensures that the general dynamics of the membranes are similar to the DPPC membranes at 333 K. Moreover, the bilayer thicknesses and area per lipid values for POPC lipids at 303 K and DPPC lipids at 333 K differ by a few Ångstrom. These several-Ångstrom differences are well within the experimental resolution. As a result, we are using POPC lipids at 303 K to construct our systems.

To study the binding of the lipid-anchored saccharides in planar membranes using full-atomistic molecular dynamics simulations, we are using self-interacting single bilayers. Fig. 2.8 illustrates the setup of the self-interacting single bilayer. The black dashed line shows the simulation box. The box height is given as the z -extension of the simulation box and is equal to the sum of the bilayer and water layer thicknesses. The periodic images of the system can be obtained by translating the simulation box by its extensions in x -, y -, and z -dimensions. The lipids (black spheres) and the lipid-anchored saccharides (red spheres) compose the bilayer with leaflets numbered 1/1' and 2/2'. The prime numbered leaflets (1' and 2') are the periodic images of the leaflets 1 and 2 and therefore have the same dynamics with their corresponding leaflets: for instance, if any atom in the leaflet 1 moves in z -dimension by a certain amount, the same atom in leaflet 1' will move in the same direction by the same amount. The lipid-anchored saccharide in leaflet 1 interacts with the one in leaflet 2', which is the periodic image of the lipid-anchored saccharide in leaflet 2. As a result, the interactions between the lipid-anchored saccharides occur essentially in the same membrane but in different periodic images. Therefore, we name this system as the self-interacting single bilayer system.

We define the membrane mid-plane as the z -coordinate of the center of mass of the lipid tail groups (gray lines in Fig. 2.8) for a given membrane. The distance between the membrane mid-planes is the average separation and corresponds to the height of the simulation box. For the opposing membranes, we can define the local separation as the distance between the membrane mid-planes at different x, y -coordinates. The average separation, then, will correspond to the average of the local separations for a given trajectory frame. Since we have only one membrane in the simulations and start from a planar configuration, regardless of the choice of x, y -coordinates on the membrane, we always get the same and constant local separation. Therefore, in the context of a self-interacting bilayer, the local and average separations correspond to the same distance

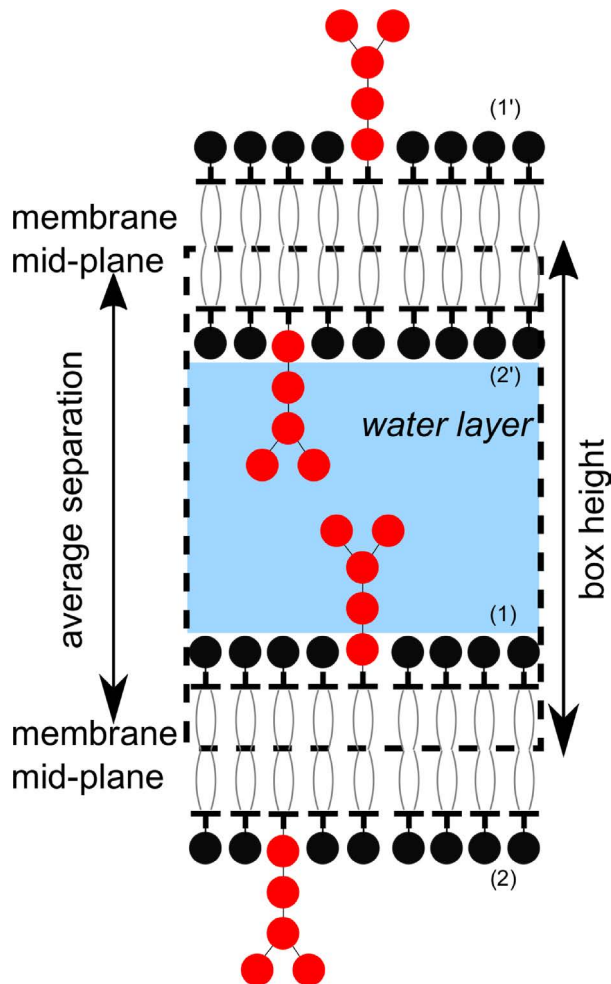


Figure 2.8: The illustration of the self-interacting single bilayer system. The dashed line shows the simulation box. The z -extension of the simulation box is labeled as the box height. The lipids (black spheres) and the lipid-anchored saccharides (red spheres) compose the bilayer with leaflets numbered 1/1' and 2/2'. The prime numbered leaflets (1' and 2') are the periodic images of the leaflets 1 and 2 in z -dimension. The periodic images 1' and 2' have the same dynamics as the leaflets 1 and 2, respectively. The z -coordinate of the center of mass of the lipid tails (gray) is defined as the membrane mid-plane. The distance between the membrane mid-planes corresponds to the average separation. In this setup, the average separation has the same distance as the box height. The local separation is defined as the separation between the membrane mid-planes at different x, y -positions and has a constant value for a given trajectory frame. Therefore, the average separation, which is obtained by averaging the local separations, is the same as the local separation. The binding of the lipid-anchored saccharides occurs between leaflets and their periodic images. Hence, we name this system as the self-interacting single bilayer system.

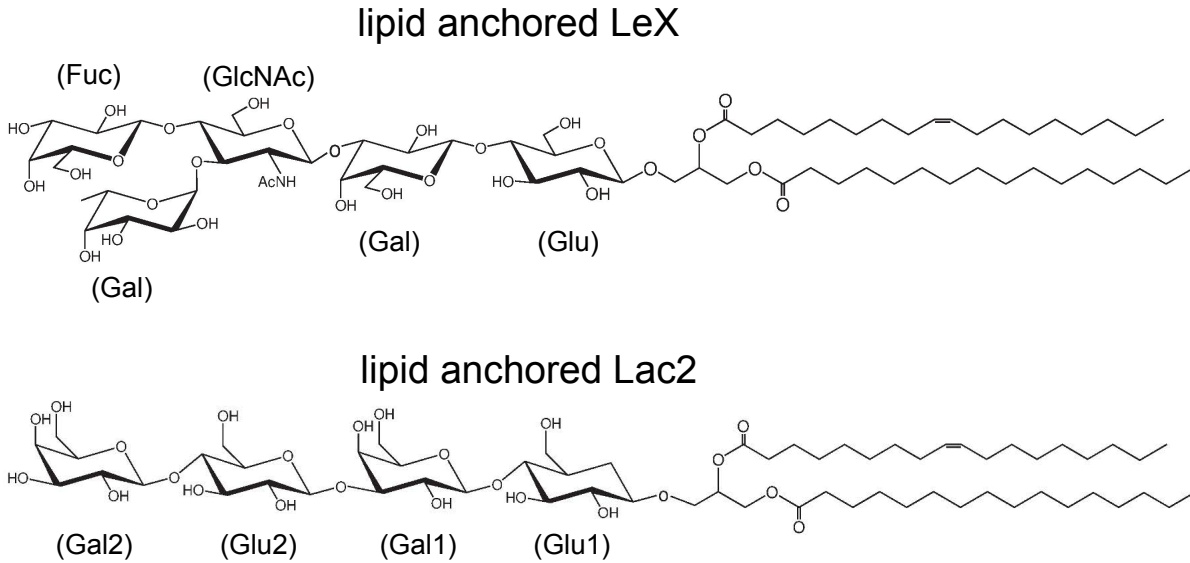


Figure 2.9: The structures of the lipid-anchored LeX (top) and Lac2 (bottom). Lipid-anchored LeX is connected to the lipid tails by a lactose residue (Galactose-Glucose) therefore has two additional saccharide units compared to the soluble LeX (Fig. 2.1). Structures of the soluble and lipid-anchored Lac2 are the same. The tails of the lipid-anchored saccharides are the same as the POPC tails. The residue names are given in parenthesis.

and can be used interchangeably.

For a given trajectory frame, the self-interacting single bilayer system ensures that the local separation between the opposing membranes will be constant and equal to the box height. The only way to change the local separation is to change the height of the simulation box in z -direction. For small membrane sizes as we use in this chapter, the fluctuations in the box height are negligible that ensures that the average separation stays almost constant.

In the binding of the lipid-anchored saccharides in planar membranes we are interested in how binding depends on the local separation. Therefore, we would like to construct membrane anchored saccharide systems at various fixed local separations. As the local separation (in the framework of self-interacting single bilayer system) is equal to the box height and box height is equal to the sum of membrane and water layer thicknesses, the local separation can be adjusted by adjusting the water layer thickness *via*

$$n_w = \frac{Ah_w}{V_w} \quad (2.1)$$

where n_w is the number of water molecules required form a water layer with a given thickness h_w for a certain area A , with each water molecule having the molecular volume V_w as the membranes are almost incompressible along z -direction (membrane normal).

The first system we construct with planar membranes is a single bilayer with two lipid-anchored saccharides in one leaflet, and none in the other. This so called *cis*-system

contains (Fig. 2.10) only in-plane interactions of the anchored saccharides because the saccharides are anchored to the same leaflet. For the *cis*-system, we choose the box height large enough to prevent any interaction of the lipid-anchored saccharides with the opposing leaflet.

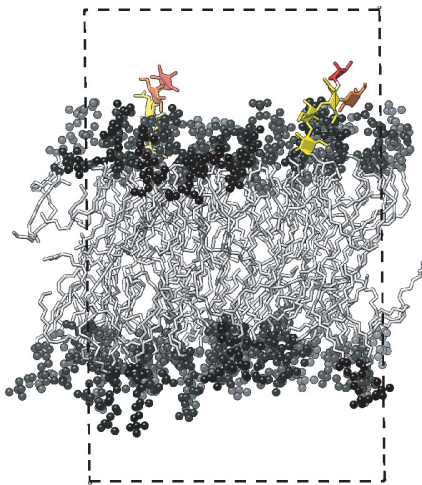


Figure 2.10: A snapshot from the simulation of LeX in single-*cis* configuration. Periodic box is drawn in dashed lines. Gal is shown in orange, Fuc in red, and the remaining saccharide units are in yellow. Lipid head groups and tails are colorized in black and gray, respectively.

The second system we construct with planar membranes is a single POPC bilayer with one lipid-anchored saccharide in each leaflet. The purpose of this single-*trans* -system (Fig. 2.11) is to study the binding of lipid-anchored saccharides as a function of local separation between planar membranes without any *cis*-interactions or membrane fluctuations. In this system there are no *cis*-interactions because there is only one lipid-anchored saccharide per leaflet. The *trans*-interactions occur through the periodic images in the z -direction. In order to change the local separation, we use Eq. 2.1 for adjusting the thickness of the water layer. We vary the local separation from 5.5 nm to 8.0 nm and 5.5 nm to 7.5 nm, for lipid-anchored LeX and Lac2, respectively.

The third system we construct with planar membranes involves ten lipid-anchored saccharides in both leaflets (Fig. 2.12). Our purpose in this system (will be denoted as ten-percent system from now on) is to study the interplay between *cis*- and *trans*-binding of lipid-anchored saccharides at a fixed local separation by excluding the membrane fluctuations. Similar to single-*trans* system, we adjust the height of the simulation box to allow interactions between opposing leaflets through periodic images in z -dimension, which in turn again creates one interface for us to study the binding. Using Eq. 2.1, we adjust the local separation between periodic images. To be consistent, we choose the same local separations as the single-*trans* simulations.

Membrane fluctuations play an important role in mediating membrane adhesion via lipid-anchored saccharides. In our planar membrane simulations, due to the self-interacting

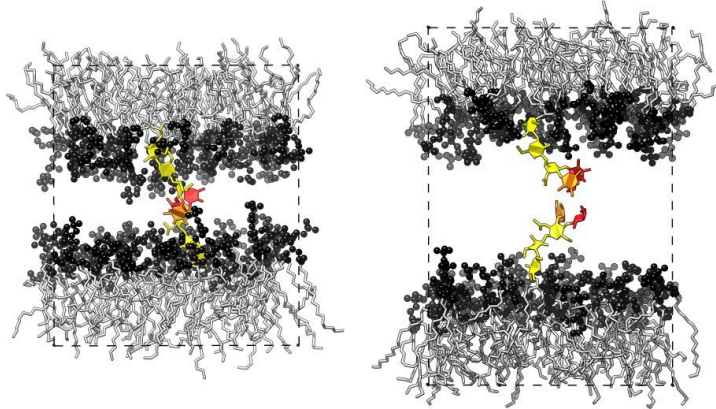


Figure 2.11: Two snapshots from the simulation of LeX in single-*trans* configuration at 5.5 nm (left) and 7.5 nm (right) local separations. Periodic box is drawn in dashed lines. Lower leaflet in each simulation has been translated in z -direction by the box height to better depict the interface between opposing leaflets. Gal is shown in orange, Fuc in red, and the remaining saccharide units are in yellow. PC head groups and lipid tails are colorized in black and gray, respectively.

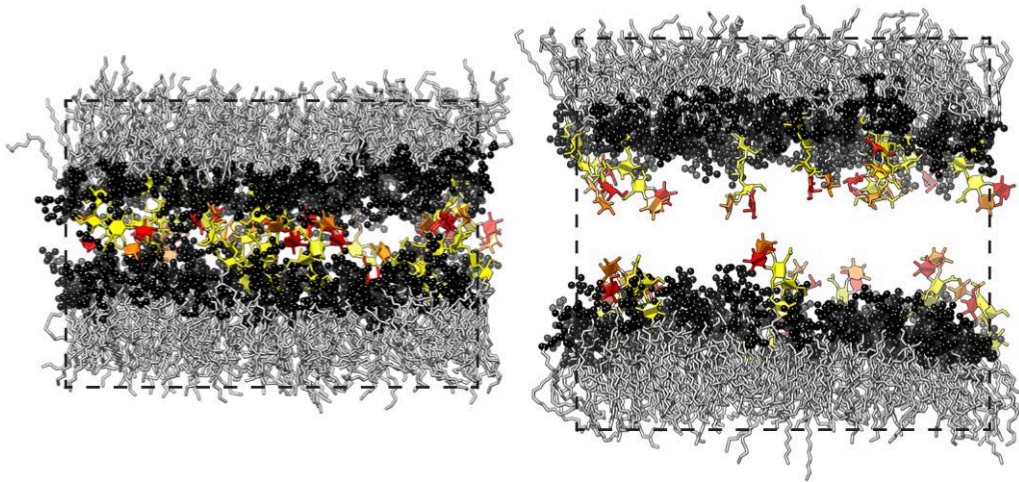


Figure 2.12: Two snapshots from the ten-percent system of LeX at 5.5 nm (left) and 7.5 nm (right) separations. Periodic box is drawn in dashed lines. Lower leaflet in each simulation has been translated in z -direction by the box height to better depict the interface between opposing leaflets. Gal is shown in orange, Fuc in red, and the remaining saccharide units are in yellow. PC head groups and lipid tails are colorized in black and gray, respectively.

bilayer, membrane fluctuations do not change the separation between the membranes. In fluctuating membranes with lipid-anchored saccharides, on the other hand, the local separation between opposing membrane patches varies with respect to time as a result of complex interplay between the binding of lipid-anchored molecules and the thermal fluctuations. In order to study how membrane fluctuations affect the membrane adhesion, we construct systems with two POPC bilayers with lipid-anchored saccharides.

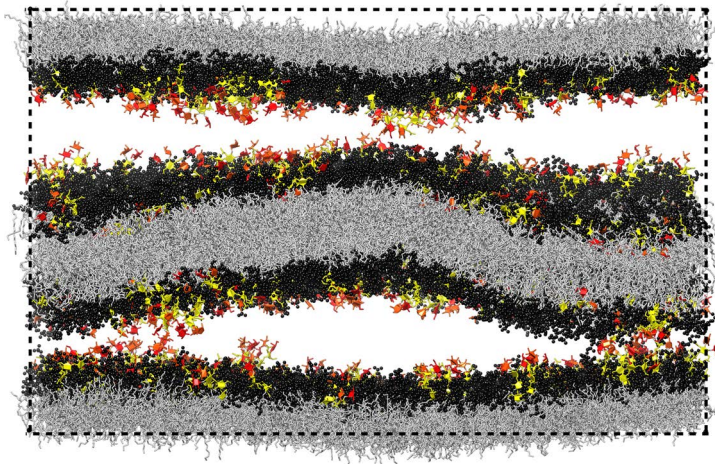


Figure 2.13: A snapshot from the double bilayer simulation. Simulation box is drawn in dashed line. One of the leaflets (lowest) is translated by the box height in z -direction to better show the interfaces. Gal is shown in orange, Fuc in red, and the remaining saccharide units are in yellow. PC head groups and lipid tails are colorized in black and gray.

The setup includes two POPC bilayers with one in every ten lipid is replaced by lipid-anchored saccharides (Fig. 2.13). We set the simulation box height such that each of the bilayer interacts with the other one both in the simulation box and through the periodic boundary conditions in z -dimension. With this setup, we create two interfaces between the apposing membranes. As we have two bilayers in the simulation box, the local separation between opposing leaflets changes due to the thermal fluctuations, giving us the opportunity to study the effects of the membrane fluctuations on membrane adhesion. For LeX saccharide, we have experimental data on the average separation and membrane roughness (i.e. the standard deviation of the local separation) for a similar setup.²⁵ Following this work, we set the average separation to be 7.7 nm, and choose only lipid-anchored LeX saccharide in the simulations.

Chapter 3

Binding of saccharides in water

Understanding the binding of saccharides in water is one of the key steps towards understanding the membrane adhesion mediated by the lipid-anchored saccharides. In water, or generally in solution, there are no constraints on the saccharides' movements. Therefore, they are free to diffuse and choose conformations that lead to lower energies. These conformations may or may not be available in the lipid-anchored systems due to the confined dynamics on the membrane surface, yet it is reasonable to expect some dynamical properties and bound conformations in solution will translate to the lipid anchored systems. The differences in the binding of saccharides in water and in the membranes will also shine light on the effects of the confinement due to a membrane. Consequently, we need to understand how saccharides bind in solution to better understand their binding in the lipid anchored systems. In the simulations of saccharides in water, we are interested in the structures of the bound and unbound states, the structural changes introduced by binding, and the binding strength.

In the MD simulations of the soluble saccharides, we have two monomers of the same kind in explicit water. The size of the simulation box is chosen large enough to prevent any self-interactions. The distance between two monomers in the initial structure is larger than the cutoff for the non-bonded interactions which ensures that the two monomers are in an unbound conformation. With this setup, we simulate LeX, Lac1, and Lac2 (all of the saccharides in this work are neutral and therefore do not carry a net charge) saccharides (Fig. 3.1) in explicit water to generate 50, 20, and 40 independent trajectories, respectively. In total, we obtain 100 μ s, 40 μ s and 40 μ s trajectories for LeX, Lac1, and Lac2, respectively.

3.1 Conformations of soluble saccharides

Dihedral angles (torsion) around the glycosidic bonds define the overall conformation of the saccharides. We calculate the dihedral angles around the glycosidic bonds in order

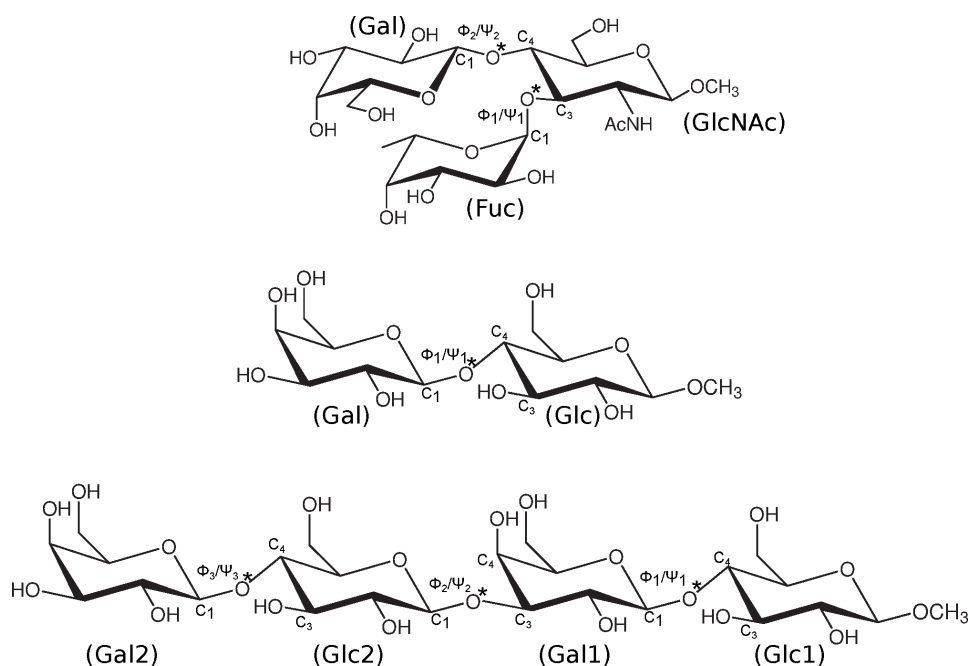


Figure 3.1: The structures of the soluble saccharides. Dihedral angles are defined as (1→3): $\phi = O - C1 - O^* - C3$, $\psi = C1 - O^* - C3 - C4$; (1→4): $\phi = O - C1 - O^* - C4$, $\psi = C1 - O^* - C4 - C3$.⁴ The residue names for each saccharide are given in parenthesis.

to reveal the available saccharide conformations in solution. Fig. 3.2 (solid lines) shows the probability distribution of the dihedrals around the glycosidic bonds for LeX, Lac1, and Lac2. For LeX, all dihedral angles have single peaks at their corresponding maxima. For the ψ angles around Fuc-GlcNAc and Gal-GlcNAc residues, there are sparsely populated regions around 95° and 75° , respectively. These regions have relative populations of $\rho_{rel} = 0.02$ and $\rho_{rel} = 0.03$ and therefore contribute very little to the overall conformation of LeX. For Lac1, we observe a single peak distribution for the ϕ angle with a small kink around 210° , a single peak distribution for the ψ angle with an extended tail towards 0° and again a small kink at 300° . The relative populations of these off-peak regions are very low ($\rho_{rel} = 0.04, 0.08, 0.04$) and similar to LeX, their overall contribution to the unbound structure of Lac1 is low. Lac2, on the other hand, shows a variety of conformations. ϕ/ψ angles around Gal2-Glc2 have the same distribution as the same angle in Lac1. ϕ/ψ angles around Gal1-Glc1 bond, although it is the same connection between the same residues, show a bimodal distribution for the ψ angle with similar relative populations. The ψ angle between Gal2-Glc1 also has two peaks with relative populations of $\rho_{rel} = 0.65$ (75°) and $\rho_{rel} = 0.35$ (140°). The small kink regions around 225° and 300° have very low populations with $\rho_{rel} = 0.03$ and $\rho_{rel} = 0.03$, respectively. As a result, we observe that there is one dominant conformation for soluble LeX and Lac1, whereas there are multiple conformations for soluble Lac2.

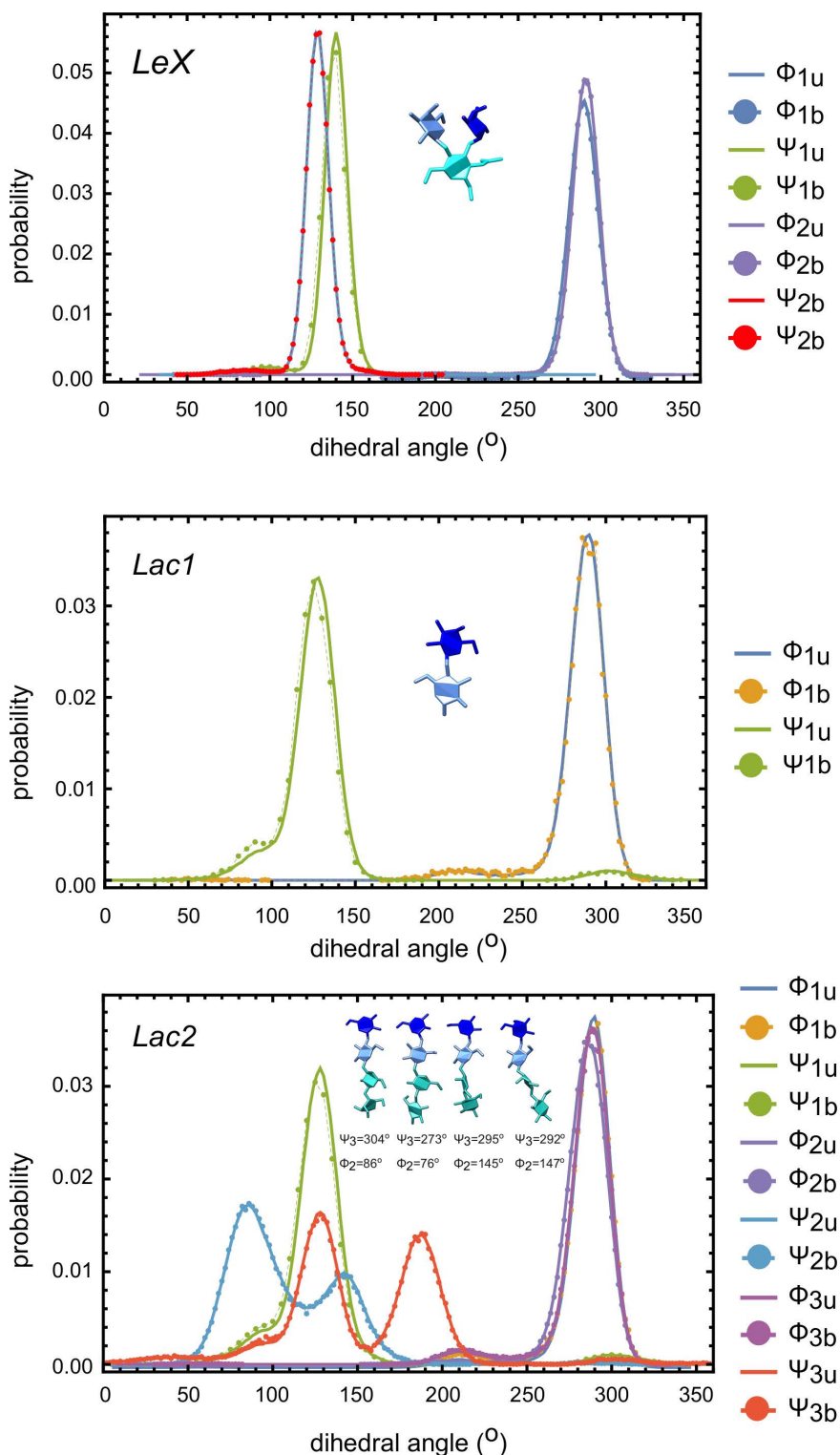


Figure 3.2: The probability distributions of the dihedral angles along the glycosidic bonds for the soluble saccharides in unbound (full lines) and bound (lines with full bullet). Inlet in each distribution contains the conformations of the soluble saccharides corresponding to the highly populated dihedral angles.

3.2 Binding of soluble saccharides

In order to study the binding of saccharides in water, we first need to adopt a measure that will distinguish between bound and unbound structures. As binding of them requires both molecules to be in the vicinity of each other, we choose to use the contacts formed between atoms as this measure. We choose a distance cutoff of 0.45 nm, i.e. whenever the distance between non-hydrogen atoms from different monomers is less than 0.45 nm we define this interaction as a contact. At the cutoff distance 0.45 nm, the Lennard-Jones potential that describes non-bonded non-electrostatic interactions almost flattens for the atoms in our systems therefore with 0.45 nm cutoff we are including most of the Lennard-Jones interactions. Fig. 3.3 shows the time series of the contacts formed between two LeX monomers. For clarity, we only show data from 5 trajectories corresponding 10 μs portion of the total 100 μs ($50 \times 2 \mu\text{s}$) data. We observe that there are many binding events, i.e. many regions with non-zero contacts. The large number of binding and unbinding events is the basis for the accurate calculation of the binding constant K_{3D} . Furthermore, we observe that there are stable intervals that last for tens of nanoseconds indicating that soluble saccharides also form relatively long-lived bound states.

The total number of contacts between the soluble saccharides can be decomposed into the contacts between the individual saccharide residues. Such a decomposition gives an idea about which saccharide residues interact with each other and provides a measure to check the convergence of our simulations. We calculate the number of contacts formed between saccharide residues after combining all independent trajectories and obtain the average number of contacts between the saccharide residues. Fig. 3.4 shows the average contact map we obtain for the soluble saccharides. In order to make the comparison easier, we also normalize each average contact map to have a maximum value of 1.0. For the soluble LeX, most frequent contact are formed between the GlcNAc. residues suggesting a parallel alignment of two soluble LeX is generally achieved when two soluble LeX interact. Similar observation is valid also for the soluble Lac1. For the soluble Lac2, both Glc1-Glc2 and Glc2-Glc2 contacts have the largest frequency. This observation indicates that soluble Lac2 can have parallel and anti-parallel alignments in the bound states with similar probabilities. Average contact maps also give us an opportunity to understand the convergence of our simulations. For a converged set of trajectories, we would expect the contacts formed between the same residue pairs from with different labels for the soluble saccharides to be equal. For instance, in a converged set of trajectories, the average number of contacts between Fuc. of the first soluble LeX and Gal. of the second soluble LeX must be the same as the average number of contacts between Gal. of the first soluble LeX and Fuc. of the second soluble LeX. This implies a symmetric average contact map. From Fig. 3.4 we observe that the average contact maps are almost symmetrical for the soluble LeX and Lac1, and to a lesser extent for the soluble Lac2. This observation suggests that our microsecond trajectories for the soluble saccharides

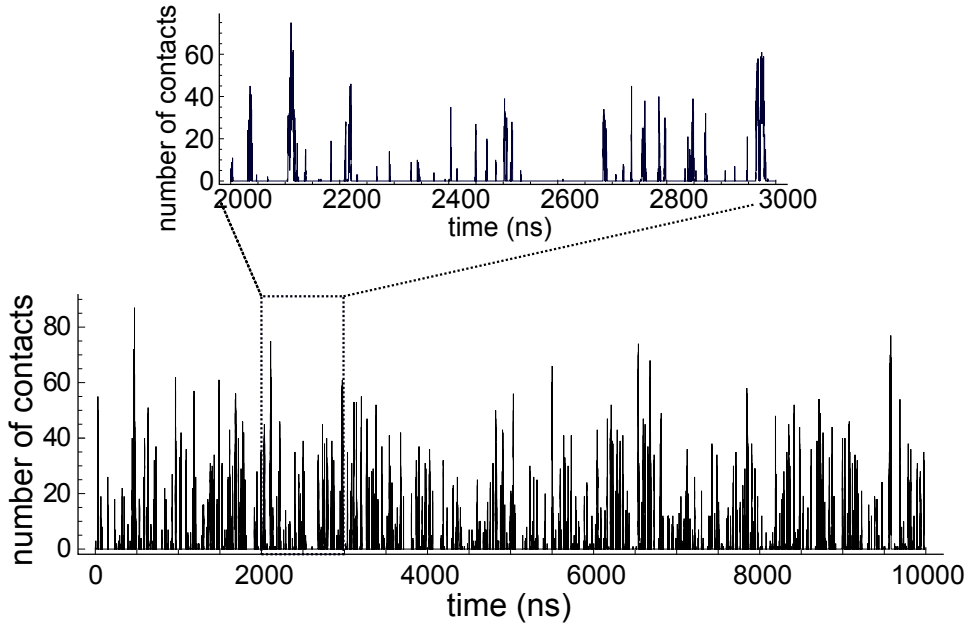


Figure 3.3: Number of contacts as a function of time for two LeX saccharides in water. Only $1 \mu\text{s}$ (top) and $10 \mu\text{s}$ (bottom) of the total $100 \mu\text{s}$ trajectory are shown for clarity. We observe similar curves for Lac1 and Lac2 (data not shown).

are converged.

Fig. 3.5 (left column) shows the probability distribution of the number of contacts. For all saccharides, we observe a monotonically decreasing function for the probability of the number of contacts N_C with the maximum number of contacts depending on the size of the saccharide. This observation does not provide a clear distinction between bound and unbound states: a dimerization process with one well-defined bound and unbound states, for example, would show a bimodal distribution of contacts with two maxima that correspond to the unbound and bound states, respectively.

The right column in Fig. 3.5 shows how the lifetimes of the contiguous intervals, i.e. intervals with non-zero contacts, are related to the maximum observed number of contacts in that interval. We observe a strong correlation between the duration of the contiguous interval and the maximum observed number of contacts (Spearman's rank-correlation coefficient $\rho = 0.82, 0.78, 0.83$ for LeX, Lac1, and Lac2, respectively). Our data shows that long living contiguous intervals are more likely to have higher N_c , which can be explained with the rationale that contacts formed between saccharide monomers stabilize the structure. For LeX and Lac2, we observe contiguous intervals up to 60 ns with more than 100 total number of contacts. However, giving the length of the total trajectories ($100 \mu\text{s}$ for LeX and $40 \mu\text{s}$ for Lac2), these states actually have rather short lifetimes. The lifetimes of Lac1 dimers are significantly shorter than other saccharides, and likely to stem from small possible number of contacts allowed as Lac1 is smaller than LeX and Lac2. Our results show that all saccharides can form dimers with the lifetimes

LeX				Lac1	
	GlcNAc	Gal	Fuc		
GlcNAc	1.00	0.50	0.26	Glc	1.00
Gal	0.49	0.20	0.18	Glu	0.66
Fuc	0.28	0.20	0.06	Glc	0.68
				Glu	0.58
 Lac2					
	Glc1	Glu1	Glc2	Glu2	
Glc1	0.98	1.00	0.90	0.49	
Glu1	0.84	0.86	0.82	0.48	
Glc2	1.00	0.77	0.99	0.58	
Glu2	0.59	0.53	0.59	0.44	

Figure 3.4: The average number of contacts between the saccharide residues calculated by combining the independent trajectories of the soluble LeX, Lac1, and Lac2. Each average contact map is normalized such that their maximum is 1. All of the contact maps are almost symmetrical suggesting that our trajectories are converged.

of tens of ns. Overall, neither the lifetimes nor the maximum number of contacts in a contiguous interval yield a clear distinction between the bound and unbound states, and suggest that the binding of soluble saccharides is weak.

To quantify the binding strength, we calculate the binding constant K_{3D} for the soluble saccharides. The binding constant K_{3D} can be calculated *via*³⁸

$$K_{3D} = V \frac{P_b}{P_u}$$

where V is the volume of the simulation box, P_b and P_u are the bound and unbound probabilities of the saccharides, respectively. We define the bound states as the contiguous intervals with the maximum observed contact number is greater than a certain cutoff value for the number of contacts. Then, we can estimate the bound probabilities simply by counting the frames in the bound states. Fig. 3.6 shows how K_{3D} depends on the contact cutoff N_{cut} for defining the bound states for the soluble saccharides. For all saccharides, we first observe that K_{3D} decreases smoothly with increasing N_{cut} . This is a direct consequence of monotonically decreasing probability distribution of the number of contacts (Fig. 3.5), as increasing the contact cutoff decreases the number of bound states. Our second observation is that the binding constant K_{3D} does not sensitively depend on the contact cutoff for the range of 1 to 20 contacts: increasing the cutoff value four times (from 5 to 20) results in only a 20% decrease in K_{3D} in the case of soluble LeX.

Fig. 3.6 further shows that Lac2 has the largest binding constant K_{3D} among all saccharides considered for all contact cutoffs, where Lac1 has the lowest. The ordering of the binding constant K_{3D} for different saccharides correlates with the sizes of the soluble saccharides. Lac2, with four saccharide residues is the largest and Lac1 with two saccharide residues is the smallest saccharide used in this work. When the saccharides

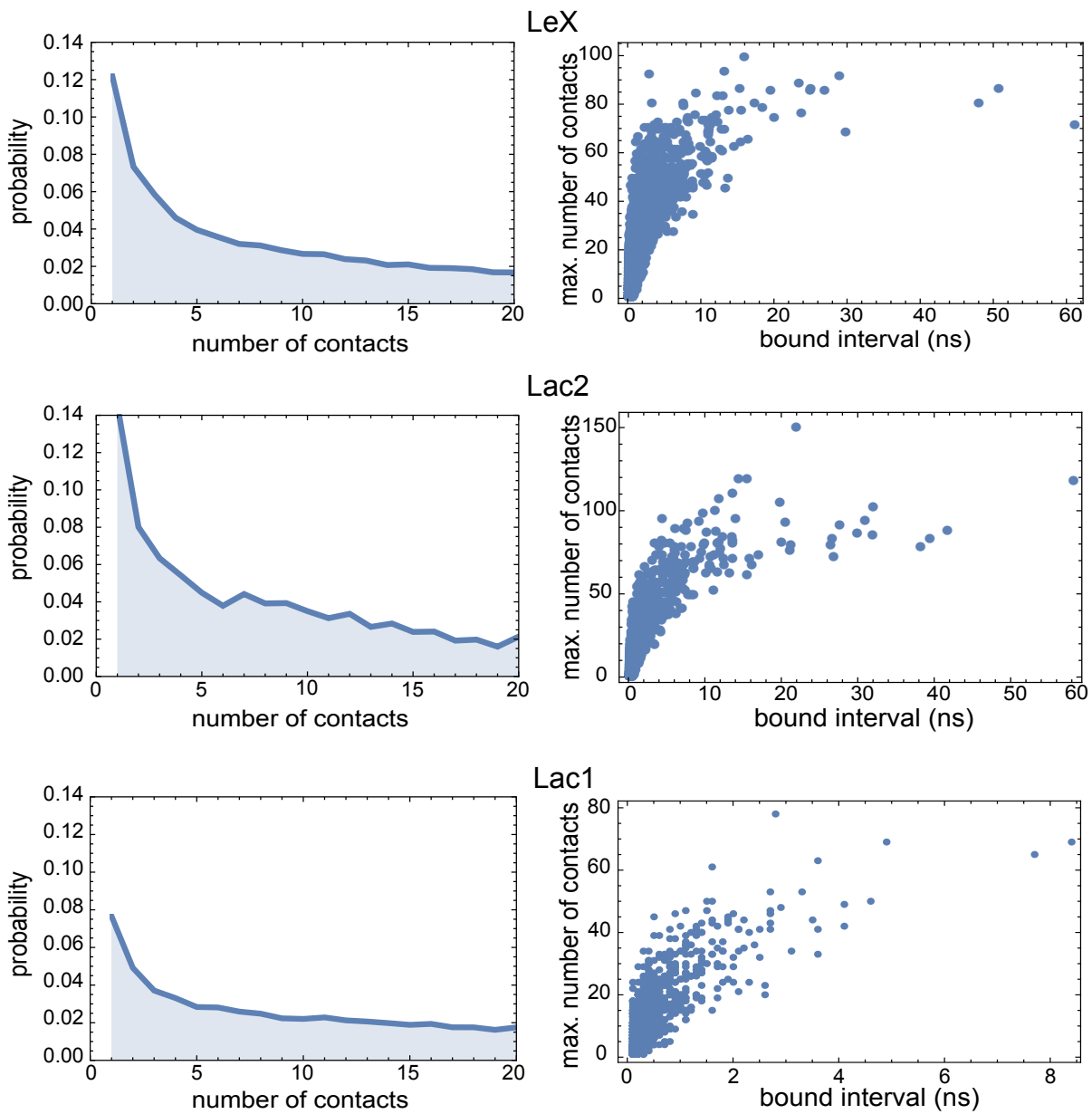


Figure 3.5: Probability distribution of the number of contacts (left column) and the maximum number of contacts in a given bound interval as a function of the lifetime of the bound interval (right column).

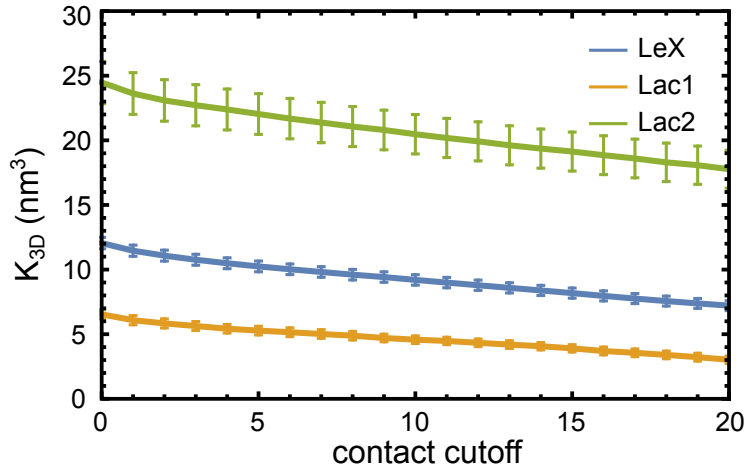


Figure 3.6: The calculated binding constant K_{3D} for soluble saccharides as a function of contact cutoff. Errors are calculated as the standard error of the mean from 50, 40, and 20 independent runs for LeX, Lac2, and Lac1, respectively.

get larger, they can form more contacts among them. Larger number of contacts, in turn, stabilizes the bound states. As a result, we obtain larger binding constants for the soluble saccharides as we increase their size.

Table 3.1 summarizes the calculated binding constants K_{3D} for LeX, Lac2, and Lac1 with contact cutoffs 5, 10, and 15. For all saccharides, the dissociation constant ($1/K_{3D}$) is in the order of molar range, suggesting that the binding of saccharides in solution is very weak.⁵⁸ As it is very difficult to experimentally measure the binding constant of small saccharides in solution due to their small size and high flexibility, there are not many experimental works available for us to compare our results. One study²¹ has approximated the binding constant of LeX in solution as $K_{3D} \approx 10 M^{-1}$. Our estimate for the binding constant has a comparable magnitude with the experimental data. However, we need to stress that the details of the experimental estimate has never been published, therefore it is impossible for us to discuss the relevance of our results to the experimental values. To the best of our knowledge, no experimental data for the binding constants have been published for Lac1 and Lac2 saccharides.

Neither the monotonically decreasing probabilities for the number of contacts nor the lifetimes of the contiguous states suggest a contact cutoff for defining the bound states. However, by considering the structures of the soluble saccharides we can argue that any contact cutoff between 5 and 15 is reasonable. In the cases of bound conformations with only one pyranose ring from each saccharide are in contact, we will have number of contacts around 4-6. As more rings interact, the total number of contacts will increase. 10 contacts will require 3 atoms from each ring to interact, and 15 contacts will contain at least 4-5 atoms per ring. We choose contact cutoff as 5 and define the bound states as the contiguous intervals with the maximum number of contacts in that interval is larger or equal to 5: any contiguous interval in the trajectory will be considered bound

	contact cutoff		
	5	10	15
LeX	$10.2 \pm 0.4 \text{ nm}^3$	$9.2 \pm 0.4 \text{ nm}^3$	$8.2 \pm 0.4 \text{ nm}^3$
	$16.4 \pm 0.9 \text{ M}^{-1}$	$14.4 \pm 0.8 \text{ M}^{-1}$	$12.5 \pm 0.7 \text{ M}^{-1}$
Lac2	$22.0 \pm 1.6 \text{ nm}^3$	$20.5 \pm 1.5 \text{ nm}^3$	$19.1 \pm 1.5 \text{ nm}^3$
	$34.3 \pm 3.2 \text{ M}^{-1}$	$31.4 \pm 3.00 \text{ M}^{-1}$	$28.9 \pm 2.8 \text{ M}^{-1}$
Lac1	$5.3 \pm 0.3 \text{ nm}^3$	$4.6 \pm 0.3 \text{ nm}^3$	$3.9 \pm 0.3 \text{ nm}^3$
	$5.8 \pm 0.7 \text{ M}^{-1}$	$5.0 \pm 0.6 \text{ M}^{-1}$	$4.3 \pm 0.6 \text{ M}^{-1}$

Table 3.1: The binding constant K_{3D} for soluble saccharides. Errors are calculated as the standard error of the mean from 50, 40, and 20 independent runs for LeX, Lac2, and Lac1, respectively.

if the maximum number of contacts in that region is larger than the contact cutoff 5. Throughout this work, we will use this definition for the bound states.

Naturally, the quantities calculated over the bound states depend on the contact cutoff we use. In these cases, we analyze the sensitivity of our results to the cutoff. For instance, the binding constant K_{3D} depends on the contact cutoff. However, within the range of contact cutoff values 1 to 20, we see that the K_{3D} does not change significantly. Consequently, we can propose that, although our definition of bound states is necessarily arbitrary, it is not unreasonable.

After defining the bound states and calculating the binding constant, we move to analyze the conformations of the bound states. To this end, we first recalculate the average contact maps for the soluble saccharides in the bound states. Fig. 3.7 shows that, for the soluble LeX the most frequent interactions are between the GlcNAc. residues and the least frequent contacts are formed between Fuc. residues. For the soluble Lac2, we see that the most frequent interactions are between Glc2-Glc1 and Glu1-Glu1 residues suggesting that both parallel and anti-parallel alignments of the two saccharides are possible. By comparing Fig. 3.4 and Fig. 3.7, we see that applying a contact cutoff 5 for the bound states almost do not change the average contacts between the saccharide residues.

Average contact maps do not readily reveal the structure of the bound states. In order to understand the structure of the bound states, we visualize the bound conformations that we obtain from the trajectories. In these visualizations we align one of the saccharide monomers to have a fixed conformation. We achieve this alignment as follows: we choose one of the saccharides as the reference monomer. Then, we calculate the root-mean-squared-displacement (RMSD) for the reference monomer in each frame with respect to the first frame of the combined total trajectory and minimize the RMSD. This procedure yields a fixed conformation of the reference saccharide (up to small fluctuations) throughout the trajectory. From the RMSD minimized trajectories, we randomly choose

<i>LeX</i>				<i>Lac1</i>		
	GlcNAc	Gal	Fuc			
GlcNAc	1.00	0.50	0.26	Glc	1.00	0.78
Gal	0.49	0.19	0.18	Glu	0.68	0.96
Fuc	0.28	0.20	0.06			

<i>Lac2</i>				
	Glc1	Glu1	Glc2	Glu2
Glc1	0.97	0.99	0.90	0.48
Glu1	0.84	0.86	0.82	0.47
Glc2	0.99	0.77	1.00	0.58
Glu2	0.58	0.53	0.59	0.43

Figure 3.7: Average number of number of contacts between the saccharides residues in bound states. We normalize each average contact map to have their maximum value to be 1.

50 configurations of the other saccharide in bound states with minimum 20, 30, and 50 contacts. Fig. 3.8 shows how the second saccharide is distributed around the first one. For all saccharides, we do not observe any well-defined structural configurations although all of these configurations belong to the bound states. Instead, we obtain a cloud-like distribution of the second saccharide around the first one. The bound structures are diverse and assume many different conformations. The observed continuum of diverse bound states without structural clusters, combined with the probability distributions of the number of contacts in the simulations (Fig. 3.5) suggests that the binding of saccharides in water is diffuse; binding of soluble saccharides occurs in numerous ways in a continuum of bound states, instead of a finite number of well-defined bound states as in induced fit and lock-and-key models of protein-ligand binding.^{59–61} Diffuse binding of LeX, Lac2, and Lac1 is one of the key findings in this thesis, and to the best of our knowledge has not been proposed before.

Last but not least, we look at the structural changes in the soluble saccharides induced by the binding by comparing the dihedral distributions around the glycosidic bonds in bound and unbound states. As shown in Fig. 3.2, the structural changes induced by the diffuse binding of soluble saccharides are negligible.

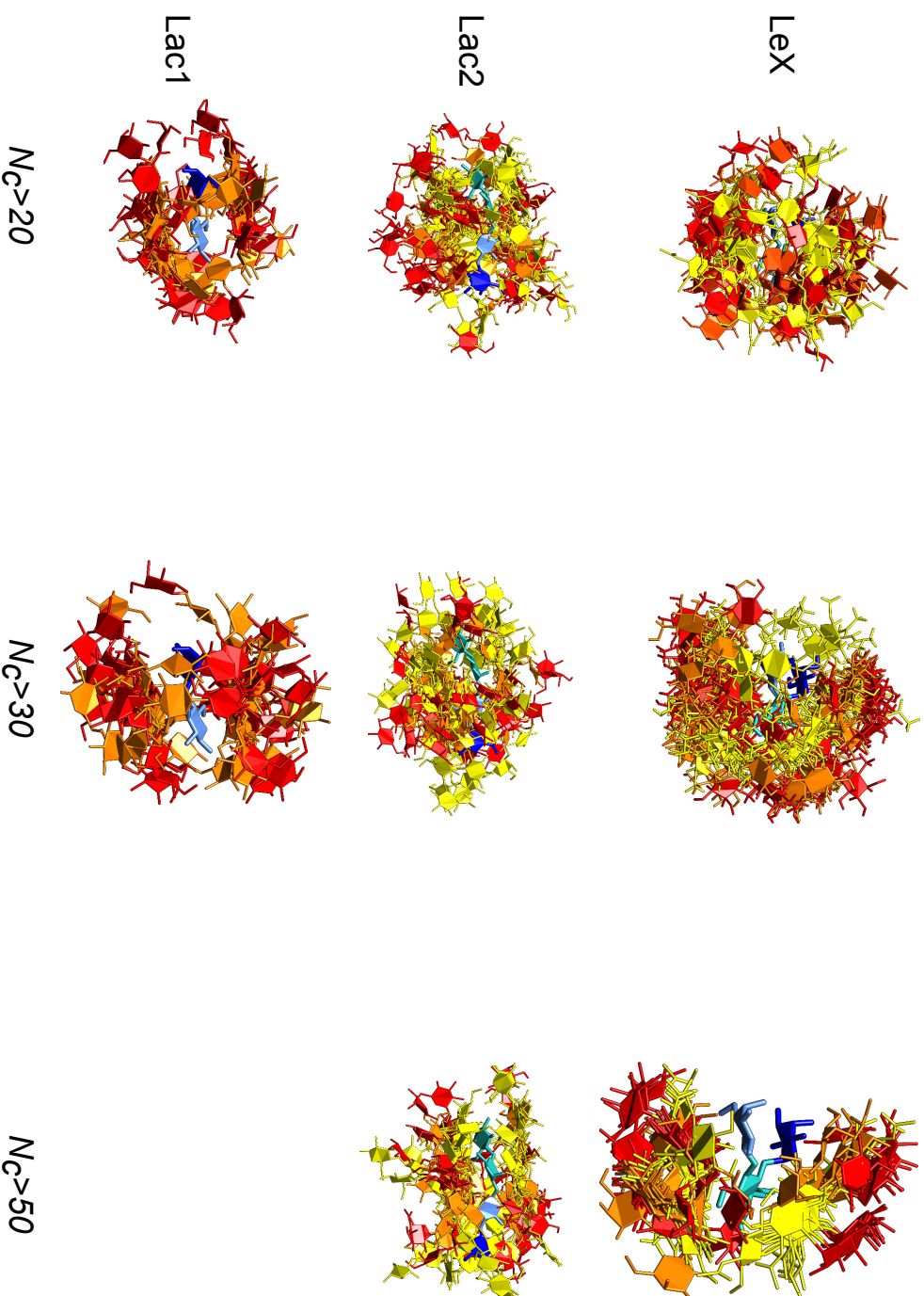


Figure 3.8: Spatial distributions of saccharides with at least 20, 30, and 50 contacts. Cold-colored saccharide (reference) has the same and fixed conformations for the entire trajectory. This fixed conformation is obtained by calculating the RMSD between the reference saccharide in the first frame of the total trajectory and the reference saccharide in the other frames of the total trajectory. Then, we minimize the RMSD between the structures of the reference saccharide in all trajectory frames. For each saccharide, we randomly select 50 conformations. For Lac1, conformations with 50 contacts are not shown as there are only a few of them. The color-code is as follows: for the soluble Lex, fucose, galactose, and GlcNAc. residues in the reference structure are shown in blue, light blue, and cyan, respectively. For the second saccharide, they are shown in red, orange, and yellow with the same ordering. For the soluble Lac2, galactose1 and glucose1 residues are in cyan/yellow, glucose2 and galactose2 are in light blue/orange and blue/red in the reference/second saccharide. For Lac1, glucose is in light blue/orange and galactose is in blue/red in the reference/second saccharide.

3.3 Summary

In this chapter, we study the binding of soluble saccharides using full-atomistic molecular dynamics simulations. To this end, we simulate two LeX, Lac1, and Lac2 monomers in explicit water for trajectory lengths up to 100 μs .

We first calculate the distributions of the dihedral angles around the glycosidic bonds to understand the conformations of the saccharides in solution. We observe that soluble Lac1 and LeX stay in one single conformation whereas Lac2 has at least four highly populated conformations. Upon the binding of the soluble saccharides, we do not observe any significant changes to the conformations.

In order to study the binding of the soluble saccharides, we calculate the number of contacts between the saccharides as a function of simulation time. We observe many binding and unbinding events for all of the soluble saccharides. We find that the maximum number of contacts between the saccharides has a positive correlation with the size of the saccharide. The probability distribution for the number of contacts decreases monotonically and does not suggest a clear contact cutoff for the definition of the bound states.

We calculate the solution binding constant K_{3D} as a function of different contact cutoff N_{cut} . We see that the binding constant decreases with increasing N_{cut} , but for small N_{cut} values (1 to 20) stays relatively constant. We define the bound states as the contiguous intervals with the maximum number of contacts in that interval is larger or equal to 5: any contiguous interval in the trajectory will be considered bound if the maximum number of contacts in that region is larger than the cutoff 5. With this definition of the bound states, we calculate the binding constant K_{3D} for the soluble saccharides. We find that soluble Lac2 has the largest binding constant whereas Lac1 has the smallest. We explain this behavior by recalling that the number of contacts formed between the saccharides correlate with the size of the saccharide. As larger number of contacts stabilize the bound states, Lac2 being the largest saccharide used in this work has the largest binding constant. In terms of the magnitude, we show that the dissociation constant for all of the saccharides is in the molar range and therefore the binding of the soluble saccharides is weak.

We visualize the bound states by fixing the orientation of one of the saccharides in the trajectory. This method depicts how the second saccharide is distributed around the first one in the bound states. We observe a cloud-like distribution of the second saccharide in the bound states. From this observation, we show that the binding of the soluble saccharides is diffuse: the binding occurs in a continuum of bound states instead of a certain number of structurally well-defined bound states.

Chapter 4

Binding of saccharides anchored in planar membranes

Membrane adhesion *via* binding of lipid-anchored saccharides emerges from a complex interplay between the properties of the lipid-anchored saccharides and the membranes. For instance, in case of two opposing membranes with lipid-anchored saccharides, the adhesion of the membranes will be dictated by the binding properties of the lipid-anchored saccharides, the separation between the membranes, and the magnitude of the membrane fluctuations. In this chapter, our aim is to study the binding of the lipid-anchored saccharides in planar membranes separated by fixed separations.

In order to study the binding of lipid-anchored saccharides in planar membranes, we are using a self-interacting single bilayer system (Fig. 2.8). The self-interacting single bilayer system consists of a single lipid bilayer with lipid-anchored saccharides. In our simulations with the periodic boundary conditions, the distance between any atom and its periodic image is given by the size of the simulation box. Therefore, the height of the simulation box defines the distance between the bilayer and its periodic image in z -dimension. For the self-interacting single bilayer system, we set the height of the simulation box such that the lipid-anchored saccharides in the upper membrane leaflet can interact with the periodic images of the lipid-anchored saccharides in the lower membrane leaflet. In other words, we are allowing lipid-anchored saccharides to interact with the periodic images of other lipid-anchored saccharides. In this work, we define the membrane mid-plane as the z -coordinate of the center of mass of the lipid tail groups for a given membrane. The average distance between the membrane mid-planes is defined as the average separation and within the self-interacting single bilayer system corresponds to the height of the simulation box. For the opposing membranes, we can define the local separation as the distance between the membrane mid-planes at different x, y -coordinates. The average separation, then, will correspond to the average of the local separations for a given trajectory frame. Since we have only one membrane in the simu-

lation box, regardless of the choice of x, y -coordinates on the membrane, we always get the same and constant local separation. Therefore, in the context of a self-interacting single bilayer, the local and average separations correspond to the same distance and can be used interchangeably. The main result of the self-interacting single bilayer system is that membrane shape fluctuations due to the thermal excitations do not change the local separation: the local and average separations between the membrane and its periodic image are equal and determined by the height of the simulation box. Consequently, the interactions between the lipid-anchored saccharides from different membrane leaflets through the periodic boundaries always occur at the same separation, up to the small fluctuations in the box height.

Using the self-interacting single bilayer system, we are studying the binding of the lipid-anchored LeX and Lac2 (Fig. 2.9). Both of the lipid-anchored saccharides have the same lipid tails as the POPC lipid and contain no net charge (neutral). For the lipid-anchored LeX, the LeX trisaccharide is connected to the glycolipid linker *via* a lactose (Galactose-Glucose) disaccharide and therefore has five saccharide residues. The lipid-anchored Lac2 has the same saccharide structure as the soluble Lac2. As lipid-anchored LeX contains five saccharide residues but branched at the tip, both of the lipid-anchored saccharides have almost the same maximum extensions (0.41 nm and 0.40 nm for the lipid-anchored LeX and Lac2, respectively).

The binding of lipid-anchored saccharides in planar membranes can occur in three ways: i) two lipid-anchored saccharides from different membrane leaflets can undergo *trans*- (*off*-plane) interactions, ii) two lipid-anchored saccharides from the same leaflet can undergo *cis*- (*on*-plane) interactions, iii) multiple lipid-anchored saccharides can undergo binding in the simultaneous presence of the *cis*- and *trans*- interactions. Consequently, we construct three different self-interacting bilayer systems to study the each of these different bindings separately. In the first two systems, we only have two lipid-anchored saccharides either in *cis*- or *trans*-configuration which aim to study the *cis*- and *trans*-binding in isolation (no simultaneous *cis*- and *trans*-interactions are present). In the last system, we allow simultaneous *cis*- and *trans*-interactions by incorporating 10% concentration of lipid-anchored saccharides in each leaflet to study the interplay of *cis*- and *trans*-binding. 10% concentration of the lipid-anchored saccharides also corresponds to the experimentally relevant concentrations.⁶²

In this chapter, our aim is to study the binding of lipid-anchored saccharides at fixed local separation between the membranes. Due to the self-interacting bilayer system, the membrane fluctuations do not change the local separation. We are particularly interested in the *on*-plane (*cis*) and *off*-plane (*trans*) binding of two lipid-anchored saccharides at different local separations and the possible coupling between *cis*- and *trans*-binding by including multiple lipid-anchored saccharides to the membrane leaflets.

This chapter is organized as follows: in Chapter 4.1 we study the *trans*-binding of

two lipid-anchored saccharides to understand how lipid-anchored saccharides in different membrane leaflet interact with each other at different local separations. Our main aim in the *trans*-binding simulations is to understand the dependency of the binding to the local separation between the membranes. Then, in Chapter. 4.2 we study the *cis*-binding of two lipid-anchored saccharides, i.e. the binding between lipid-anchored saccharides in the same leaflet. In Ch. 4.3 we combine the *cis*- and *trans*- binding of the lipid-anchored saccharides by using planar membrane patches with a 10% mol concentration of the lipid-anchored saccharides at different local separations to study the possible correlations between the *cis*- and *trans*-binding. In all sections, we calculate the corresponding binding constant for the particular interaction.

4.1 *Trans*-binding

Membrane adhesion is mediated by the binding of the lipid-anchored receptors and ligands from opposing membranes. In this section we present the results from our simulations of two lipid-anchored saccharides in self-interacting single bilayer system. This system, which we will refer to as the single-*trans* system hereafter, is an isolated case in which only the interactions of the lipid-anchored saccharides between different membrane leaflets are allowed. Our main aim is to calculate the two-dimensional *trans*-binding constant $K_{2D}^{trans}(l)$ as a function of the local separation.

The self-interacting single-*trans* system is composed of a single bilayer with 35 POPC lipids and one lipid-anchored saccharide (LeX and Lac2) in each leaflet. The box extensions are 4.8×4.8 nm in the *xy*-plane and are large enough to prevent any self-interaction of the lipid-anchored molecules. The box height can be adjusted by adjusting the number of water molecules in the simulation box *via*

$$d = \frac{N_w V_w}{A} \quad (4.1)$$

where d is the desired height of the water layer, A is the area of the simulation box, N_w is the required number of water molecules to obtain a height of d , and V_w is the volume per water molecule ($V_w \approx 30.48 \text{ \AA}^3$). By using Eq. 4.1 we vary the height of the simulation box from 5.5 nm to 7.5 nm with 0.5 nm increments both for self-interacting membranes with lipid-anchored LeX and Lac2. Table 4.1 shows the average simulated box heights (local separations) for all trajectories. With these setups, we obtain ten independent trajectories for each local separation. The lengths per trajectory are 3 μs and 1 μs for the lipid-anchored LeX and Lac2, with the total simulation times of 30 μs and 10 μs , respectively.

Fig. 4.1 shows the number of contacts between lipid-anchored saccharides as a function of time for two different local separations. For the local separation 5.5 nm, both of the lipid-anchored saccharides have many binding and unbinding events. As we increase the

	box height (nm)				
LeX	5.49 ± 0.01	6.00 ± 0.02	6.51 ± 0.01	7.01 ± 0.01	7.50 ± 0.01
Lac2	5.59 ± 0.01	6.04 ± 0.02	6.55 ± 0.01	7.05 ± 0.01	7.55 ± 0.01

Table 4.1: Average box height for the simulations. Note that, average box height is equal to the average separation between the membrane and its periodic image. Errors are calculated as the standard error of the mean over ten independent trajectories.

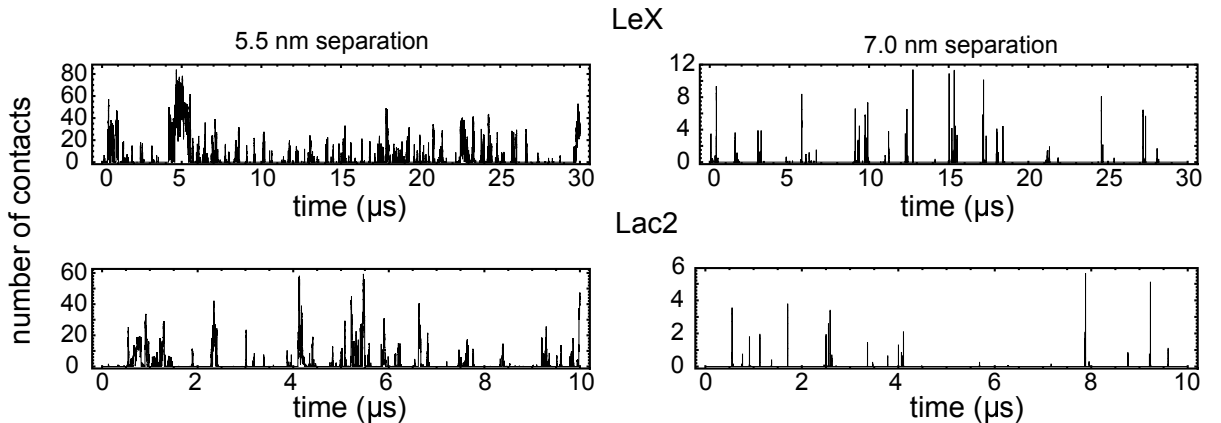


Figure 4.1: The number of contacts as function of time for the lipid-anchored LeX (top) and Lac2 (bottom) for 5.5 nm (left) and 7.0 nm (right) local separations.

local separation to 7.0 nm, we observe significantly fewer binding events: the increasing local separation decreases the maximum number of possible contacts, resulting in weaker binding events. The maximum number of contacts for the lipid-anchored LeX is reduced from 80 to 10 as we increase the local separation from 5.5 nm to 7.0 nm.

The probability distributions of the number of contacts in Fig. 4.2 shows a decreasing probability for increasing number of contacts, similar to the binding of soluble saccharides. The monotonically decreasing probability distributions indicate that the binding of lipid-anchored saccharides in single-*trans* configuration is diffuse.

As the binding of lipid-anchored saccharides in single-*trans* system is diffuse, there is no clear contacts cutoff to distinguish between the bound and unbound states. Therefore, in order to be consistent with our previous calculations of the binding constants for the binding of the soluble saccharides, we choose the contact cutoff as 5 contacts. The bound probabilities P_b for the lipid-anchored saccharides in single-*trans* configuration, then, can be obtained by counting the number of contiguous frames with at least 5 contacts. The two-dimensional binding constant at a given local separation l can be calculated *via*³⁸

$$K_{2D}^{trans}(l) = A \frac{P_b}{P_u} \quad (4.2)$$

where A is the average surface area of the membranes and P_u ($P_u=1-P_b$) is the probability of being unbound. $K_{2D}(l)^{trans}$ defines the *trans*-binding strength of the lipid-anchored

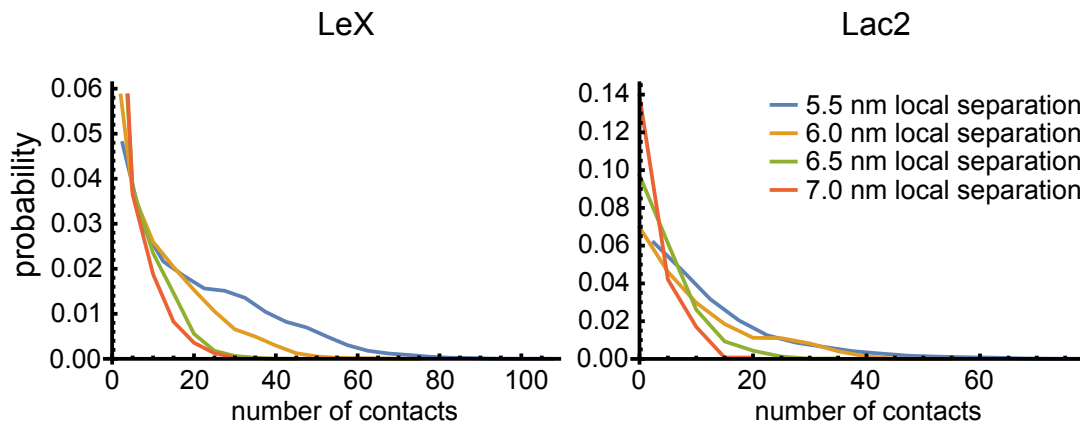


Figure 4.2: The probability distributions of the number of contacts observed in all trajectories as a function of number of contacts.

saccharides at different local separations l . The error for the binding constant can be obtained by propagating the error in the bound probabilities P_b as $err = (\partial K_{2D}^{trans} / \partial P_b) s_{P_b}$ where s_{P_b} is the standard error of the mean of the P_b calculated over ten independent trajectories.

Fig. 4.3 shows the binding constant $K_{2D}^{trans}(l)$ as a function of the local separation for the lipid-anchored LeX and Lac2. For both of the lipid-anchored saccharides, the binding constant K_{2D}^{trans} decreases with increasing local separation. The main reason behind this behavior is that at smaller local separations, the lipid-anchored saccharides can form many contacts. As the local separation increases, there are less available contact areas for the lipid-anchored saccharides to interact. Therefore, the binding constant decreases with the increasing local separation. This observation also correlates with the diffuse binding of the lipid-anchored saccharides: we know that the binding occurs in a continuum of bound states and there is no preferred binding sites on the lipid-anchored saccharides. In comparison, we can look at the binding of the rod-like lipid-anchored receptors and ligands with one single binding site at their tip.³⁸ For such molecules, the binding constant $K_{2D}(l)$ has a maximum at the local separation that corresponds to the length of the tip-to-tip bound structures. If the lipid-anchored LeX and Lac2 had single interaction sites, we would observe the maximum of the binding constant at local separations corresponding to the best alignment of the interaction sites. However, as the binding of the lipid-anchored LeX and Lac2 is diffuse, such single interaction site does not exist.

Table 4.2 summarizes our results for the binding constant $K_{2D}^{trans}(l)$ as a function of the local separation. In terms of the magnitude of the binding constants for the lipid-anchored LeX and Lac2, the K_{2D}^{trans} values agree within the error estimates except at 6.0 nm local separation, at which the lipid-anchored LeX has a larger binding constant than Lac2.

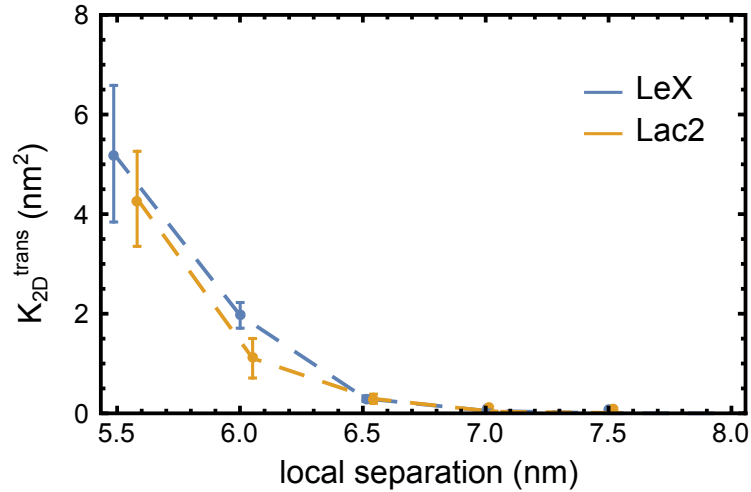


Figure 4.3: The *trans* binding constant $K_{2D}^{trans}(l)$ as a function of local separation for the *trans*-configured lipid-anchored LeX and Lac2. Errors are calculated by propagating the errors in the number of *trans* bonds (Eq. 4.4)

local separation (nm)	$K_{2D,LeX}^{trans}(nm^2)$	$K_{2D,Lac2}^{trans}(nm^2)$
5.5	5.21 ± 1.37	4.31 ± 0.95
6.0	1.97 ± 0.26	1.11 ± 0.40
6.5	$3.0 \times 10^{-1} \pm 0.6 \times 10^{-1}$	$2.9 \times 10^{-1} \pm 0.9 \times 10^{-1}$
7.0	$5.0 \times 10^{-2} \pm 1.5 \times 10^{-2}$	$3.4 \times 10^{-2} \pm 0.1 \times 10^{-2}$
7.5	$1.8 \times 10^{-3} \pm 1.8 \times 10^{-3}$	$8.8 \times 10^{-3} \pm 8.2 \times 10^{-3}$

Table 4.2: The *trans* binding constant $K_{2D}^{trans}(l)$ values for the *trans*-configured lipid-anchored LeX and Lac2. Values are adopted from Fig. 4.3

In order to visualize the diffuse binding, we observe how one of the lipid-anchored saccharides is distributed around the second one in the bound states. To this end, we first obtain the frames with the bound states. Then, we choose one of the lipid-anchored saccharides as the reference molecule. Our aim is to fix the orientation of this reference molecule throughout the trajectory so that we can understand how the second lipid-anchored saccharide is orientated around the reference molecule in the bound states. To achieve this, we calculate the root-mean-squared-displacement (RMSD) of the reference molecule in all frames with respect to the first frame of the trajectory. Then, we apply rotations to all frames of the trajectory to minimize the RMSD difference of the reference molecule with respect to the first frame of the trajectory. Note that our trajectories are rotationally invariant. This procedure essentially fixes the three-dimensional configuration of the reference lipid-anchored saccharide (up to small fluctuations) and gives us an opportunity to understand the distribution of the relative orientations of two lipid-anchored saccharides. Fig. 4.4 shows how one of the lipid-anchored saccharides is

distributed around the other one for the bound states with at least 10 number of contacts. For both of the lipid-anchored saccharides we do not observe well-defined regions for the binding. Instead, similar to the soluble saccharides and two lipid-anchored saccharides in *cis*-configuration, we observe a cloud-like distribution of the bound lipid-anchored saccharides around each other. This observation further demonstrates the diffuse binding characteristics of the lipid-anchored saccharides. We calculate the average number of contacts (contact maps) between the saccharide residues by averaging the number of contacts occurring between the saccharide residues in bound states. The calculated average number of the contacts between different lipid-anchored saccharide residues accompanies the corresponding bound states: at smaller local separations, almost all saccharide units can interact significantly but as the local separation increases only the saccharide head residues interact (Fig. 4.4 contact maps).

A visual inspection of the trajectories suggest that the unbound lipid-anchored saccharides are tilted towards the lipid head groups for most part of the trajectories. In order to quantify the observed tilting from our trajectories, we calculate the tilt angle θ_{tilt} for the bound and unbound states of the both lipid-anchored saccharides as the angle between the axial vectors and membrane normal. The axial vectors are defined as the vectors from the first to the last saccharide residues with respect to the glycolipid linker. Thus, for the lipid-anchored LeX the axial vector is between the glucose and the center of mass of the galactose and fucose residues. For the lipid-anchored Lac2, the axial vector is between galactose-2 and glucose-1. We calculate the average tilt angle by $\langle \theta_{tilt} \rangle = \int \theta_{tilt} P(\theta_{tilt}) d\theta_{tilt}$. Fig. 4.5 shows how the average tilt angle depends on the local separation. At 7.5 nm local separation the lipid-anchored Lac2 has few bound states yielding very high noise in the data. Therefore, we omit that data point from the plot. Both lipid-anchored LeX and Lac2 assume more parallel alignment with the membrane normal with increasing local separation. As the local separation increases, the lipid-anchored saccharides need to align themselves in more upright orientation for trans binding to occur. This observation is in line with the contact maps (Fig. 4.4) where only head-to-head saccharide-saccharide contacts are observed at larger local separations. At 8.0 nm local separation there are no bound states and both of the lipid-anchored saccharides assume average tilt angles $\approx 47^\circ$.

Fig. 4.5 further shows that for all local separations, except at 6.0 nm local separation, both lipid-anchored LeX and Lac2 have the the same average tilt angle. At 6.0 nm local separation, on the other hand, the lipid-anchored LeX has a smaller average tilt angle than the lipid-anchored Lac2 by $\approx 5^\circ$. When we compare these results on the average tilt angle with the binding constant K_{2D}^{trans} (Fig. 4.3) we observe a correlation between them: for all local separations except 6.0 nm, both of the lipid-anchored saccharides have similar binding constants within the error estimation. At 6.0 nm local separation, where the lipid-anchored LeX is less tilted than the lipid-anchored Lac2, the lipid-anchored LeX has a larger binding constant than the lipid-anchored Lac2. Our results suggest

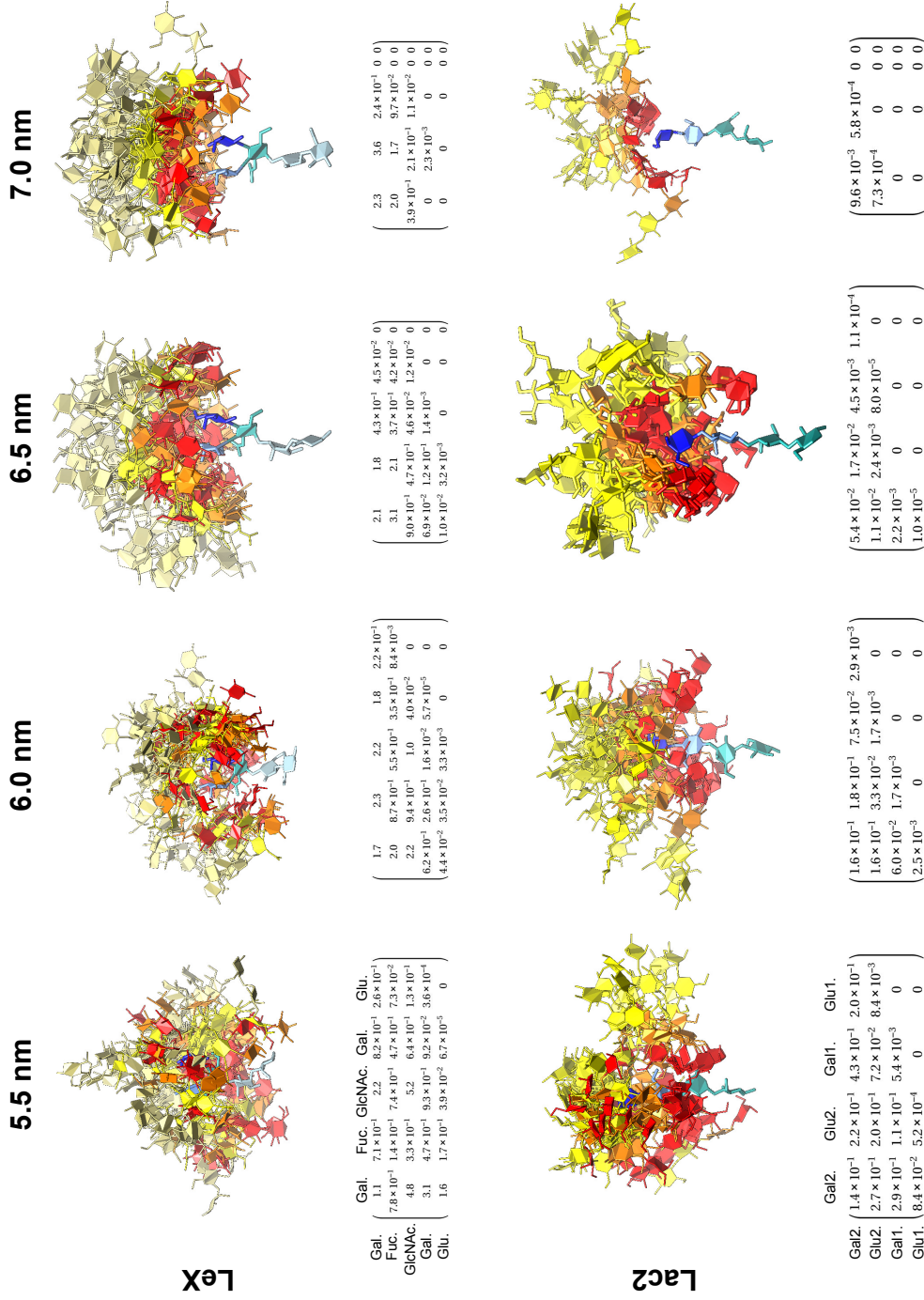


Figure 4.4: The structures of 50 bound states with at least 10 contacts superimposed around the first lipid-anchored LeX and Lac2 as a function of local separation. The cold-colored saccharide is referred to as the reference saccharide. We fix the orientation of the reference saccharide in all frames by first aligning the vector between the last and first saccharide residues parallel to the membrane normal (z -axis). Then, we minimize the root-mean-squared-displacement (RMSD) of the reference saccharide in all frames with respect to the first frame in the total trajectory. For the lipid-anchored LeX, the color code is: red, orange, yellow, and beige for the fucose, galactose, GlcNAc. and the rest of the second lipid-anchored LeX; blue, medium blue, cyan, and light blue for the fucose, galactose, GlcNAc. and the rest of the first lipid-anchored Lac2, respectively. For the lipid-anchored Lac2: red, orange, and yellow for galactose1, glucosel1, and the rest of the second lipid-anchored Lac2; blue, medium blue, and cyan for the galactose1, glucosel1 and the rest of the first lipid-anchored Lac2, respectively. The average number of contacts formed between lipid-anchored saccharide units in the bound states for the corresponding local separation are given below the snapshots.

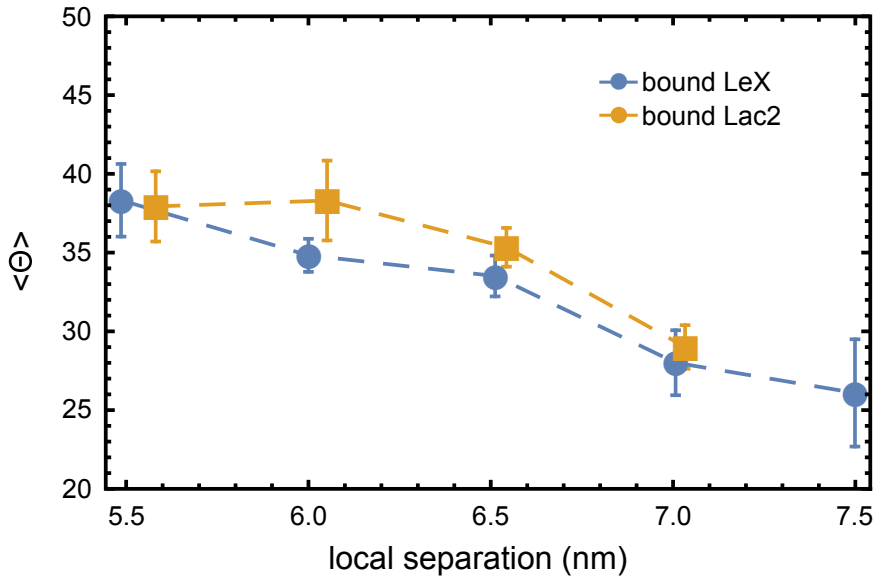


Figure 4.5: The average tilt angle for the bound lipid-anchored LeX (blue) and Lac2 (orange) as a function of local separation. We define the tilt angle θ_{tilt} same as we did in the *cis*-binding (Ch. 4.2). We calculate the average tilt angle $\langle \theta_{tilt} \rangle$ as $\langle \theta_{tilt} \rangle = \int \theta_{tilt} P(\theta_{tilt}) d\theta_{tilt}$ where $P(\theta_{tilt})$ is the probability distribution of the tilt angle. Green and red data points show the average tilt angle for the lipid-anchored LeX and Lac2 at 8.0 nm local separation, respectively. At 8.0 nm local separation there are no bound states. The average tilt angles in the unbound states at 8.0 nm local separation are similar to the average tilt angles we obtain for the *cis*-binding. For the lipid-anchored Lac2, at 7.5 nm local separation there are only a few bound states resulting in very noisy data. Therefore, we omit the data point for 7.5 nm local separation. For both of the lipid-anchored saccharides, θ_{tilt} decreases with increasing local separation meaning that the lipid-anchored saccharides tend to stay more upright in larger separations when they engage in trans interactions. The errors are calculated as the standard error of the mean over ten independent trajectories.

that, by having a smaller average tilt angle the lipid-anchored LeX can form more bound states than the lipid-anchored Lac2 at 6.0 nm local separation yielding a larger binding constant for the lipid-anchored LeX.

4.2 *Cis*-binding

In this section, we present our results on the binding of two lipid-anchored saccharides in *cis*-configuration, i.e. only the in-plane interactions between lipid-anchored saccharides are allowed. As the strength of the *cis*-binding is a key parameter in the in-plane clustering of lipid-anchored saccharides and can affect the binding of lipid-anchored saccharides from *different* membrane leaflets, it is important to study the *cis*-binding of the lipid-anchored saccharides.

Our system to study the *cis*-binding of lipid-anchored saccharides is composed of a

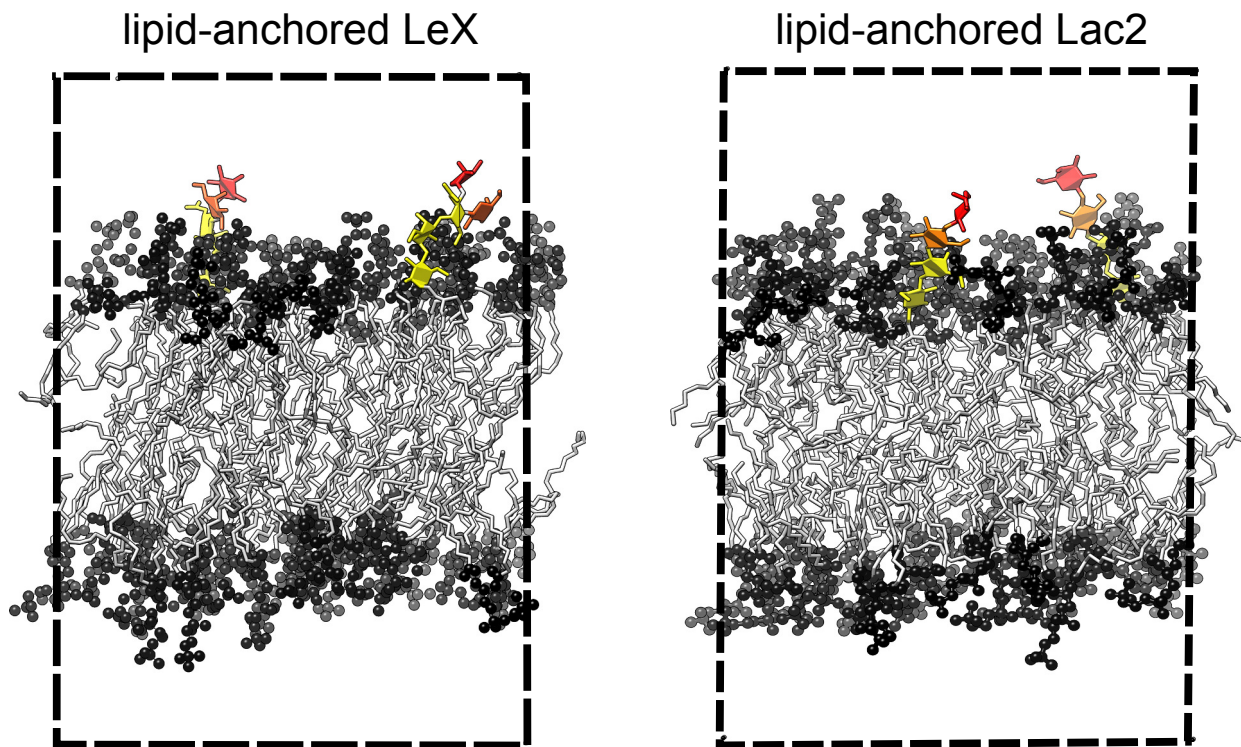


Figure 4.6: Snapshots from the simulations of two lipid-anchored saccharides in *cis*-configuration. For the lipid-anchored LeX (left), fucose, galactose and the remaining saccharide residues are shown in red, orange, and yellow respectively. The same coloring order is used for the lipid-anchored Lac2 (right) for the Gal2, Glu2, and the remaining saccharide residues. Lipid tails and head groups are colored in gray and black, respectively. Periodic box has been drawn in dashed lines.

single bilayer of 36 POPC lipids in one leaflet and 34 POPC lipids in the other. Two lipid-anchored saccharides are added to the leaflet with 34 POPC lipids to introduce in-plane interactions between the lipid-anchored saccharides. In order to prevent lipid-anchored saccharides to interact with the other leaflet through the periodic boundaries, we set the height of the simulation box as 8.0 nm. This choice of the box height is large enough to ensure that lipid-anchored saccharides only interact with each other and the leaflet that accommodates them. Our simulation box, then, has the approximate size of $2.5 \times 2.5 \times 8.0 \text{ nm}^3$. For the lipid-anchored saccharides, we study the *cis*-binding of the lipid-anchored LeX and Lac2 (Fig. 4.6). The total trajectory lengths for each lipid-anchored saccharide are $75 \mu\text{s}$ and $12.5 \mu\text{s}$ for LeX and Lac2, respectively, with 25 independent trajectories for each. For the future reference, we denote this system as the *single-cis* system.

To study *cis*-binding of lipid-anchored saccharides, we first calculate the number of contacts between lipid-anchored saccharides as a function of time using a distance cutoff of 0.45 nm. Fig. 4.7 shows the time series of the total number of contacts calculated for lipid-anchored LeX and Lac2. We observe many binding and unbinding events for

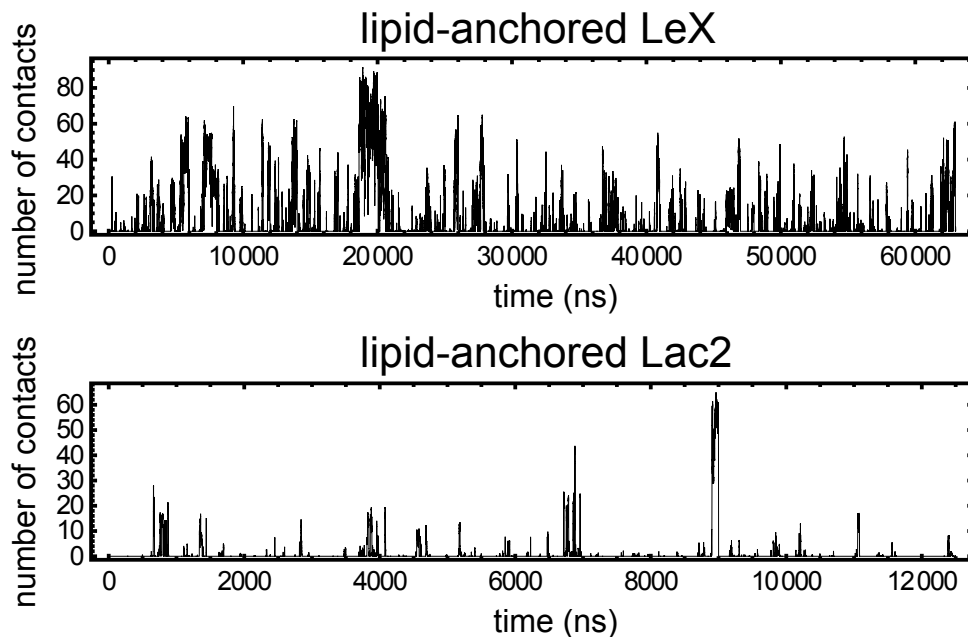


Figure 4.7: The number of contacts as a function of time for the lipid-anchored LeX (top) and Lac2 (bottom) for single-*cis* system. Full trajectories are shown. Smoothing over 20 frames has been applied.

the both lipid-anchored saccharides with Lac2 interacting less frequently than LeX. This observation is important in the accurate calculation of the two-dimensional *cis*-binding constant K_{2D}^{cis} and indicates that the K_{2D}^{cis} for Lac2 is smaller than of LeX. Furthermore, we observe that both lipid-anchored saccharides can form long-living bound states that can go up to tens of nanoseconds (even hundreds of nanoseconds in case of LeX).

Fig. 4.8 (left column) shows the probability distribution of the total number of contacts between lipid-anchored saccharides. The probability distributions for the both lipid-anchored saccharides assume a monotonically decreasing form. Similar to the case of the binding of the soluble saccharides, this is a result of the diffuse binding of the lipid-anchored saccharides and therefore there is not a well-defined cutoff value for the total number of contacts that can distinguish the bound and unbound states. The right column of Fig. 4.8 shows the maximum number of contacts observed in contiguous bounds states as a function of the lifetime of the bound states. For the lipid-anchored LeX, we observe bound states with lifetimes up to 500 ns, whereas Lac2 has a maximum lifetime of 100 ns in our trajectories. For both of the lipid-anchored saccharides, there is a positive correlation between the lifetime of a given bound state and the maximum number of contacts observed in it (Spearman's correlation coefficient is calculated as $\rho_{LeX} \approx 0.77$ and $\rho_{Lac2} \approx 0.66$) as the contacts between lipid-anchored saccharides stabilize the bound states.

The *cis*-binding constant K_{2D}^{cis} for two lipid-anchored saccharides can be calculated as

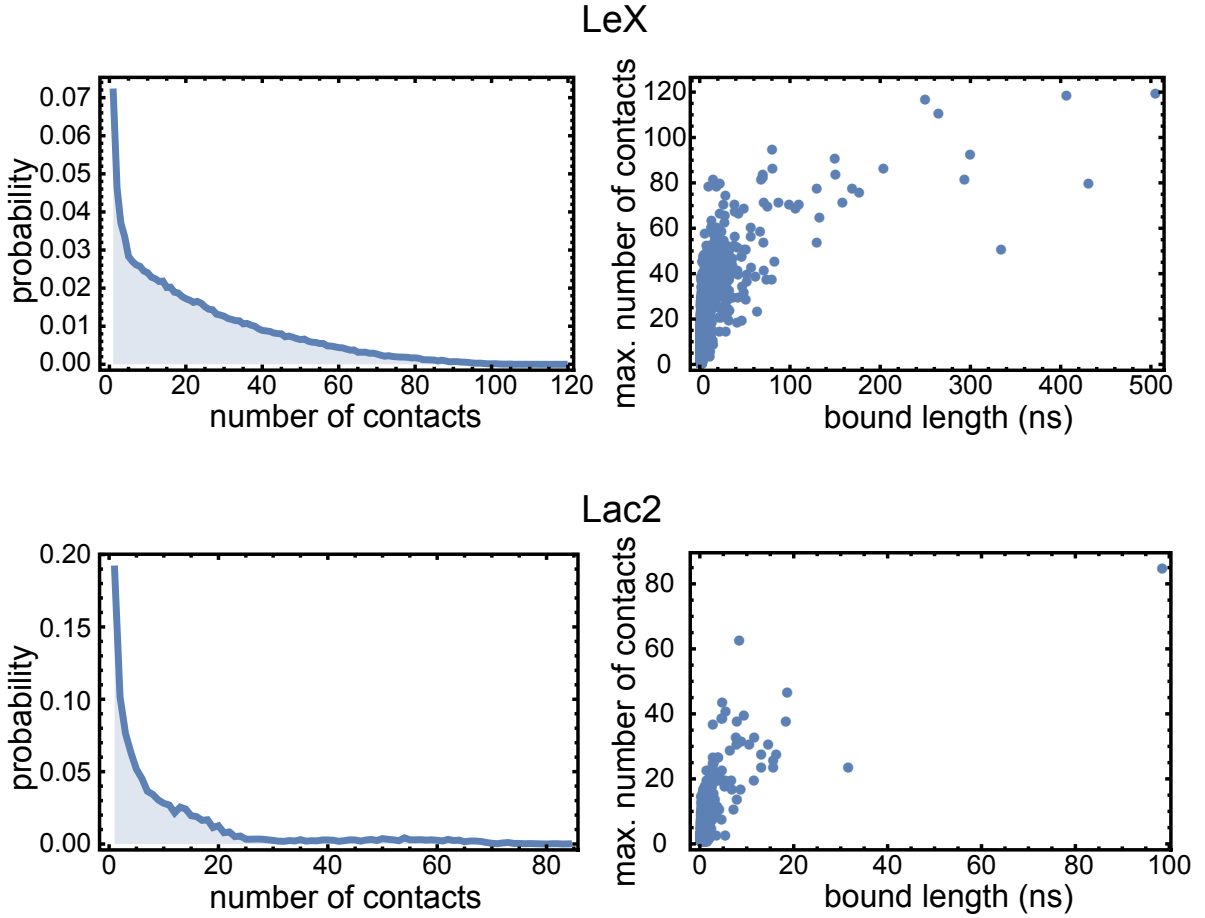


Figure 4.8: The probability distribution of the number of contacts (left column) and the maximum number of contacts in a given bound interval as a function of the lifetime of the bound interval (right column) for the single-*cis* system.

the ratio of the bound and unbound probabilities (P_b , $P_u = 1 - P_b$) via

$$K_{2D}^{cis} = A \frac{P_b}{1 - P_b} \quad (4.3)$$

where A is the surface area.³⁸ The bound probability P_b can be calculated directly from the trajectories with a chosen contact cutoff by counting the number of frames in the contiguous bound intervals and dividing this number to the total number of frames. Similar to the simulations of soluble saccharides, we first calculate the binding constant as a function of the contact cutoff. The errors are calculated by propagating the error in P_b using

$$err = \frac{\partial K_{2D}^{cis}}{\partial P_b} s_{P_b} \quad (4.4)$$

with s_{P_b} being the standard error of the mean of the bound probability P_b over 25 independent trajectories. As the area fluctuations ($A = 23.39 \pm 0.01$ nm² for LeX) are very low, we do not include them in the error analysis.

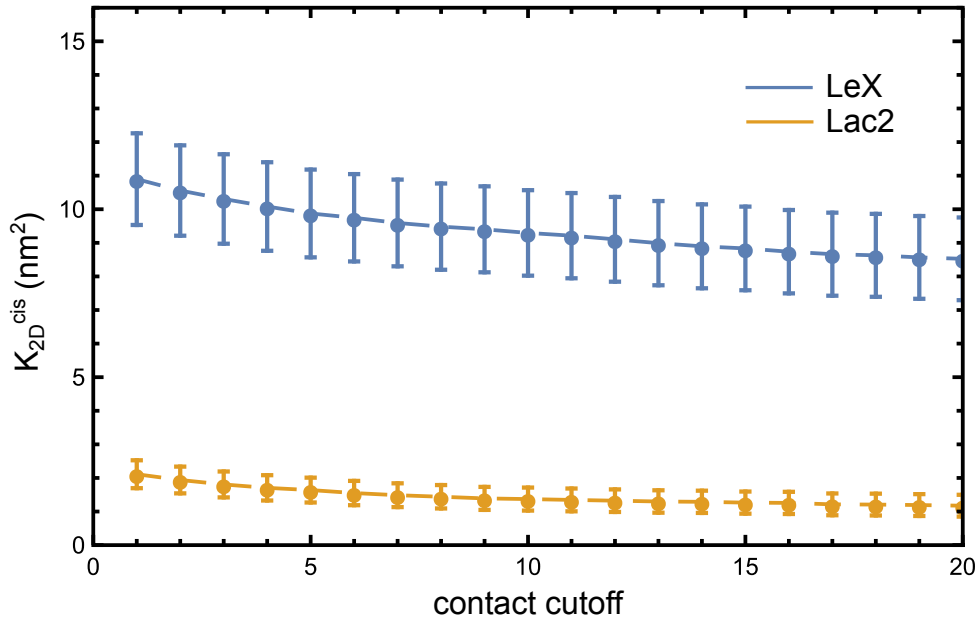


Figure 4.9: The binding constant K_{2D}^{cis} as a function of contact cutoff for two lipid-anchored saccharides in *cis*-configuration. The mean values are averaged over 25 independent trajectories ($3 \mu\text{s}$ each for LeX and 500 ns each for Lac2). We calculate the errors by propagating the error in the bound probabilities (See Eq. 4.4).

Fig. 4.9 shows how the *cis*-binding constant depends on the applied cutoff for the number of contacts N_{cut} between the lipid-anchored LeX and Lac2. Our first observation is that lipid-anchored LeX has almost five times larger *cis*-binding constant than lipid-anchored Lac2 for all N_{cut} . This is interesting, as this ordering is the opposite of the soluble saccharides in which we have found that the soluble Lac2 has roughly three times larger binding constant K_{3D} than the soluble LeX (Fig. 3.6). One of the reasons for this behavior is that in the case of soluble LeX, we have a trisaccharide whereas in the lipid-anchored LeX, we have two more saccharide units. Therefore, the lipid-anchored LeX can have form more contacts in the single-*cis*-configuration than the soluble LeX which yields a larger binding constant. Our second observation is that the *cis*-binding constants K_{2D}^{cis} behave similar to the K_{3D} curves we obtained from the soluble saccharides (Fig. 3.6), i.e. there is a decrease of 10 to 20% in K_{2D}^{cis} when changing the N_{cut} from 5 to 20. Table 4.3 tabulates the *cis*-binding constant as a function of contact cutoffs 5, 10, and 15. For the both saccharides the *cis*-binding constant for these cutoffs is within the error bars. Following this observation, to be consistent with our results from the binding of soluble saccharides, we choose the contact cutoff for the number of contacts as 5 and report the *cis*-binding constant for the lipid-anchored LeX and Lac2 as $9.87 \pm 1.31 \text{ nm}^2$ and $1.64 \pm 0.41 \text{ nm}^2$, respectively.

The monotonically decreasing probability distribution of the number of contacts, similar to the soluble saccharides, suggests that the binding of lipid-anchored saccharides in

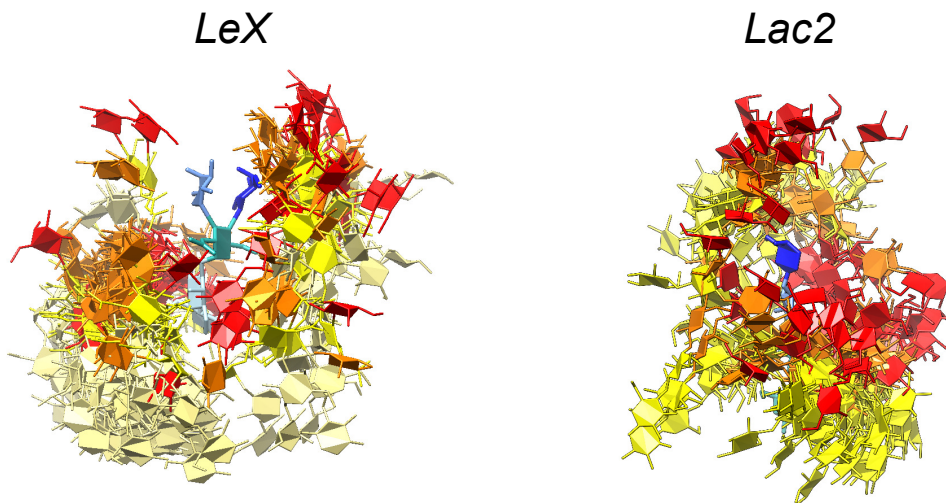


Figure 4.10: The structures of the second lipid-anchored saccharide around the first one for 50 random bound states with at least 20 contacts. These structures are obtained by minimizing the root-mean-squared-displacement (RMSD) for the first lipid-anchored saccharide in the bound states. Therefore, the first lipid-anchored saccharide has a fixed configuration in all of these bound states. For the lipid-anchored LeX, the color code is: red, orange, yellow, and beige for the fucose, galactose, GlcNAc. and the rest of the second lipid-anchored LeX; blue, medium blue, cyan, and light blue for the fucose, galactose, GlcNAc. and the rest of the first lipid-anchored LeX, respectively. For the lipid-anchored Lac2: red, orange, and yellow for galactose1, glucose1, and the rest of the second lipid-anchored Lac2; blue, medium blue, and cyan for the galactose1, glucose1 and the rest of the first lipid-anchored Lac2, respectively.

cis-configuration is also diffuse (Fig. 4.8). In order to visualize the diffuse binding, we look at the structures of the bound states and visualize how the second lipid-anchored saccharide is distributed around the first one in the bound states. We perform the alignment of the first lipid-anchored saccharide as described in Chapter 4.1. Fig. 4.10 (left column) shows the structures of 50 bound structures with at least 20 contacts. For both of the lipid-anchored saccharides, we observe a cloud-like distribution of the second lipid-anchored saccharide around the first (reference) one and therefore we do not obtain well-defined bound state structures. This observation is in line with our previous finding that the binding of saccharides is diffuse.

The tilting angle between the lipid-anchored saccharides and the membrane normal (z -axis) is the last point we would like to discuss in this section. In order to quantify the tilting from our trajectories, we calculate the tilt angle θ_{tilt} for the bound and unbound states of the both lipid-anchored saccharides as the angle between the axial vectors and membrane normal as described in Chapter 4.1. Both in bound and unbound states, we calculate the most probable tilt angles as $\theta_{tilt} = 50^\circ$ and $\theta_{tilt} = 55^\circ$ for the lipid-anchored LeX and Lac2, respectively. The tilting of the lipid-anchored saccharides confines the structure of the bound states: large tilting angles result in more contacts between the

	contact cutoff		
	5	10	15
LeX (nm ²)	9.87 ± 1.31	9.30 ± 1.27	8.83 ± 1.24
Lac2 (nm ²)	1.64 ± 0.41	1.37 ± 0.38	1.26 ± 0.37

Table 4.3: The binding constants K_{2D}^{cis} (in nm²) for the lipid-anchored LeX and Lac2 calculated at different contact cutoffs. Similar to the binding of soluble saccharides, we choose the binding constant at contact cutoff 5 when reporting the K_{2D}^{cis} .

	LeX					Lac2				
	Gal.	Fuc.	GlcNAc.	Gal.	Glc.		Gal.2	Glc.2	Gal.1	Glc.1
Gal.	0.15	0.18	0.38	0.18	0.042	Gal.2 Glc.2 Glc.1 Gal.1	0.49	0.63	0.59	0.23
Fuc.	0.092	0.026	0.081	0.022	0.017		1.0	0.82	0.77	0.24
GlcNAc.	0.26	0.080	1.0	0.46	0.18		0.33	0.82	0.66	0.52
Gal.	0.13	0.024	0.36	0.24	0.18		0.064	0.037	0.070	0.80
Glc.	0.13	0.039	0.14	0.076	0.34					

Figure 4.11: The average number of contacts between lipid-anchored saccharide units for the bound states. Each contact map has been normalized such that the maximum average contact number is 1.

lipid-anchored saccharides and the lipid-head groups within the same leaflet. As a result, there are less available interaction surfaces between the lipid-anchored saccharides. This is visible from Fig. 4.7 where the maximum number of contacts for the lipid-anchored Lac2 is almost half of the soluble Lac2. A similar effect is observed in the lipid-anchored LeX to a lesser extent. However, as the structures of the LeX in soluble and lipid-anchored simulations are different by two saccharide units, the direct comparison of the number of contacts between the LeX saccharides is not possible. The tilting of lipid-anchored saccharides have been also observed in the literature, especially for the GM1.⁶³

The average number of contacts between different saccharide units (contact map) can be used to demonstrate both the effect of tilting and the convergence of our simulations. In order to calculate the contact map, we calculate the average number of contacts between each residue of the lipid-anchored saccharides in bound states. From Fig. 4.11 we observe that for the lipid-anchored Lac2 there are many contacts between all of the saccharides units except the glucose1 residues. Given the anchoring saccharides into membranes limit the structure of the bound states, highly pronounced contacts between tip saccharide units (galactose2 and glucose2) and end saccharide units (galactose1 and glucose1) are only possible by the tilting of the lipid-anchored Lac2. We observe similar results in lipid-anchored LeX as well.

The contact map in Fig. 4.11 further demonstrates that in our simulations we are not sampling all of the possible bound states. For a fully-converged trajectory (which we generate by combining 25 independent trajectories) we would expect a symmetric contact

map: in a converged trajectory the average number of contacts between the saccharide units must be the same irrespective of our numbering the lipid-anchored saccharides. Still, as the calculated quantities such as the *cis*-binding constant have low errors, we can conclude that our results are significant.

4.3 Coupling of *trans*- and *cis*-binding

The systems described in the previous sections, namely the single-*cis* (Ch. 4.2) and single-*trans* (Ch. 4.1) are the isolated examples of the interaction between the lipid-anchored saccharides: previously we either allowed only *cis*- or *trans*-interactions in our simulations. In realistic systems, on the other hand, there are multiple lipid-anchored saccharides in each membrane leaflet. As a result, the *cis*- and *trans*-interactions are allowed simultaneously and the overall binding of lipid-anchored saccharides depend on the relative strength of these binding events.

In Ch. 4.2 we have calculated the *cis*-binding constant as $K_{2D}^{cis}=9.87\pm 1.31$ nm² and $K_{2D}^{cis}=1.61\pm 0.41$ nm² for the lipid-anchored LeX and Lac2, respectively. Comparing the *cis*-binding constants to the *trans*-binding constants $K_{2D}^{trans}(l)$ for LeX and Lac2 at different local separations (Ch. 4.3), we see that for small local separations (5.5-6.5 nm) the K_{2D}^{cis} and K_{2D}^{trans} have comparable values, and for larger separations, the *cis* binding constant becomes much larger than the *trans*-binding constant.

Our aim in this section is to understand the binding of lipid-anchored saccharides when there are both *cis*- and *trans*-interactions present. As the membrane adhesion is mediated via the *trans*-binding of lipid-anchored saccharides, we would like to quantify the strength of *trans*-binding by calculating the *effective* binding constant $K_{2D}^{eff}(l)$.

Our system to study the coupling of *trans*- and *cis*-binding is composed of a single self-interacting bilayer with 90 POPC lipids in each leaflet. We add 10 lipid-anchored saccharides to each leaflet to get a ten percent mol concentration of the lipid-anchored saccharides. With this setup, which we name the ten-percent system, the box size becomes $\approx 8.0 \times 8.0$ nm². We adjust the box height using the Eq. 4.1 and vary from 5.5 nm to 7.5 nm with 0.5 nm increments (Table 4.4). This range of box heights, similar to single-*trans* system, allows the lipid-anchored saccharides from different leaflets to interact through the periodic boundaries. The local separation, i.e. the distance between the membrane mid-planes in the opposing leaflets, is equal to the box height and stays relatively constant throughout the simulations due to the small fluctuations of the box height.

For the ten-percent system, the number of atoms varies from 45000 for 5.5 nm local separation to 66000 for 7.5 nm local separation. For each lipid-anchored saccharide, we run ten independent trajectories each of which is 1 μ s long. In total, we obtain 10 μ s trajectory for the lipid-anchored LeX and Lac2.

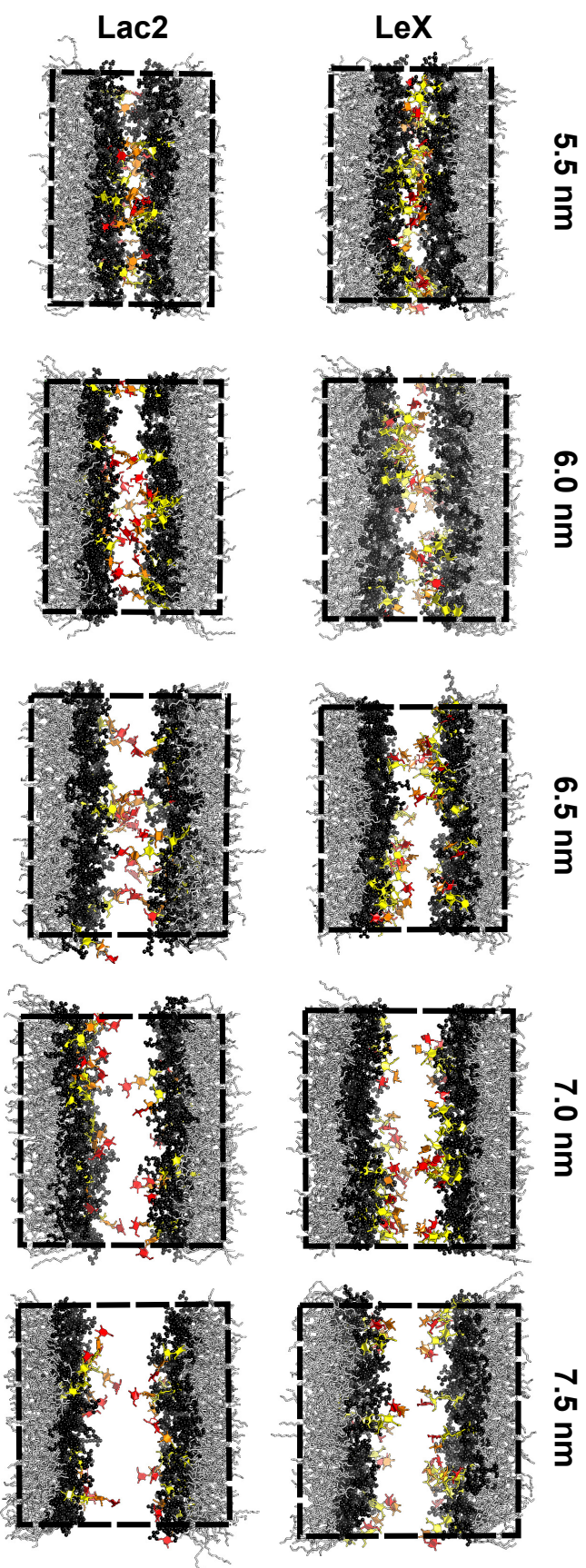


Figure 4.12: Snapshots from the simulations of ten-percent system of lipid-anchored LeX and Lac2 in planar membranes for the local separations 5.5 nm to 7.5 nm. The simulation boxes are drawn in dashed lines. The trajectories are aligned such that center of mass of each molecule is inside the simulation box. The color code is: red, orange, and yellow for fucose, galactose, and the rest of the lipid anchored LeX; red, orange, and yellow for galactose2, glucose2, and the rest of the lipid-anchored Lac2, respectively.

	box height (nm)				
LeX	5.61 ± 0.01	6.01 ± 0.01	6.56 ± 0.01	7.07 ± 0.01	7.55 ± 0.01
Lac2	5.57 ± 0.01	5.99 ± 0.01	6.52 ± 0.01	7.04 ± 0.01	7.53 ± 0.01

Table 4.4: The average box height for the ten-percent simulations. Errors are calculated as the standard error of the mean over ten independent trajectories.

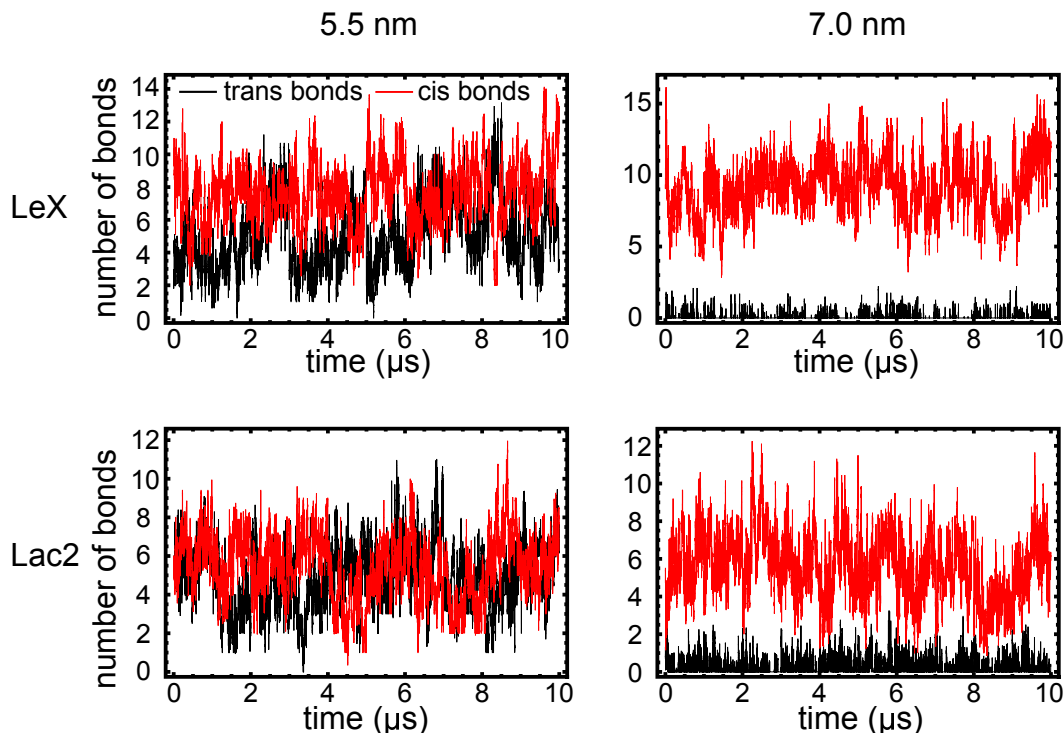


Figure 4.13: The number of *cis*- and *trans*-bonds as a function of time for the lipid-anchored LeX (top) and Lac2 (bottom). For clarity, we only show the number of bonds at 5.5 nm (left) and 7.0 nm (right) separations. The number of *trans*-bonds at 7.5 nm separation is very small for the both lipid-anchored LeX and Lac2.

In order to study the binding of lipid-anchored saccharides, we first calculate the number of contacts between the lipid-anchored saccharides per trajectory frame using a 0.45 nm distance cutoff. Then, similar to the previous chapters, we define the bound states as the contiguous intervals with the maximum number of observed contact is at least five. For each bound state, we assign a bond. If the bound states contain only *cis*-interactions, then we have a *cis*-bond and vice versa. Fig 4.13 shows the *cis*- and *trans*-bonds per frame for 5.5 nm and 7.0 nm local separations. At 5.5 nm local separation, both lipid-anchored LeX and Lac2 have at least one *trans*-bond per frame and an average of five *trans*-bonds. At this local separation, the number of *cis*-bonds and *trans*-bonds are similar. As the local separation increases, the number of *trans*-bonds per frame decreases and at ≥ 7.5 nm local separations, we observe almost no *trans*-bonds. The number of

cis-bonds, on the other hand, stays constant with increasing local separation. Since the *cis*-bonds occur only in the same leaflet, the strength of the *cis*-binding does not strongly depend on the local separation.

The binding constant for the *trans*-interactions can be obtained *via*³⁸

$$K_{2D}(l) = \frac{[L - L]}{[L][L]} \quad (4.5)$$

where $[L - L]$ and $[L]$ denotes the surface concentration of the *trans*-bound and unbound lipid-anchored saccharides, respectively. If we assume that each of the *trans*-engaged lipid-anchored saccharide contains one *trans*-bond, we can calculate the surface concentration of the *trans*-engaged lipid-anchored saccharides as $[L - L] = (n_{trans})/A$ where A is the surface area and n_{trans} is the total number of *trans*-bonds. Similarly, for the unbound lipid-anchored saccharides, we can calculate their surface concentration as $[L] = N_0 - n_{trans}/A$ with N_0 being the initial number of the unbound lipid-anchored saccharides. By substituting the expressions for $[L]$ and $[L-L]$ and remembering that there are 10 lipid-anchored saccharides in each leaflet, we can express Eq. 4.5 as

$$K_{2D}(l) = A \frac{n_{trans}}{(10 - n_{trans})^2} \quad (4.6)$$

to obtain the effective two-dimensional binding constant $K_{2D}^{eff}(l)$ for a given local separation l . The reason that we label this binding constant as the effective binding constant instead of simply *trans*-binding constant is that, although we are only considering *trans* interactions by counting the *trans*-bonds, the formation of *trans*-bonds is affected by the *cis*-interactions as well. Therefore, the binding constant we calculate via Eq. 4.6 reflects the overall *trans*-binding as an outcome of *trans*- and *cis*-interactions.

One crucial assumption we made when expressing the K_{2D}^{eff} is that every *trans*-engaged lipid-anchored saccharide forms one *trans*-bond in the *trans*-engaged complex. We can check the validity of this assumption by calculating the populations of the *trans*-multimers (dimers, trimers, ...). The simplest *trans*-engaged lipid-anchored saccharide complex with multiple *trans*-bonds per lipid-anchored saccharide is the *trans*-trimers with two *trans*-bonds. We calculate the overall frequency of these particular *trans*-trimers and find that they occur 0.30 and 0.17 times per frame at 5.5 nm separation for the lipid-anchored LeX and Lac2, respectively. Comparing these frequencies with the frequency of the *trans*-dimers (1.0 and 0.6 for LeX and Lac2, respectively) we see that *trans*-trimers with two *trans*-bonds occur less frequently than the *trans*-dimers. At larger separations, the difference between the frequency of the *trans*-dimers and *trans*-trimers is more drastic: at 7.0 nm local separation, for instance, the frequencies of *trans*-dimers for a given frame are 0.018 and 0.096 whereas the *trans*-trimer frequencies are 0.0005 and 0.0063 for the lipid-anchored LeX and Lac2, respectively. Consequently, we therefore neglect the contributions of the *trans*-trimers and higher multimers to the effective binding constant.

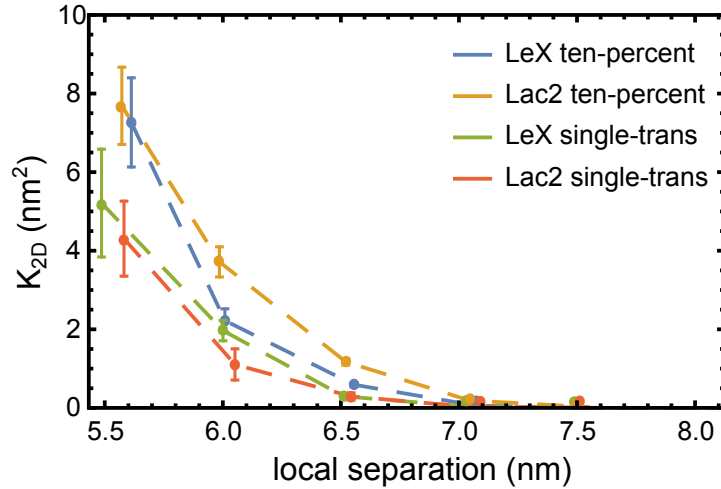


Figure 4.14: The effective $K_{2D}(l)$ calculated for the ten-percent simulations of the lipid-anchored LeX and Lac2. For comparison, the binding constants $K_{2D}(l)$ from single-*trans* simulations of the lipid-anchored LeX and Lac2 are also shown.

The effective binding constants for lipid-anchored LeX and Lac2 as a function of the local separation is given in Fig. 4.14. For comparison, we also show the *trans*-binding constants from Ch. 4.1. We observe that for the lipid-anchored LeX, the effective binding constant $K_{2D}^{eff}(l)$ and the *trans*-binding constant $K_{2D}^{trans}(l)$ have the same values within the error bars at 5.5 and 6.0 nm local separations, and for 6.5 nm local separation $K_{2D}^{eff}(l)$ is slightly larger than $K_{2D}^{trans}(l)$. For higher separations, both binding constants have similar values which suggests that there is no cooperativity between the *cis*- and *trans*-binding of the lipid-anchored LeX. For the lipid-anchored Lac2, we observe that the effective binding constant $K_{2D}^{eff}(l)$ is larger than the $K_{2D}^{trans}(l)$ at all local separations, which indicates that there is a positive cooperativity between the *cis*- and *trans*-binding of the lipid-anchored Lac2.

In order to further analyze the coupling between the *cis*- and *trans*-binding, we calculate the average tilt angle for the bound states of the lipid-anchored LeX and Lac2. Fig. 4.15 shows the average tilt angle for bound lipid-anchored LeX and Lac2 as a function of local separation at 10% mol concentration. For comparison, we include the results from the single *trans*-system (Fig. 4.5). For both of the lipid-anchored saccharides, we see that the average tilt angle decreases with increasing local separation where this decrease is more pronounced at 7.0 nm and 7.5 nm local separations. This observation is in line with our previous observations on the average tilt angle in single *trans*-system (Ch. 4.1). At 10% mol concentration, the lipid-anchored saccharide has a smaller average tilt angle than the lipid-anchored LeX at 6.0 nm and 6.5 nm local separations. This is important, as the ordering is reversed in the single-*trans* system. This results explains why the lipid-anchored Lac2 has a larger binding constant than the lipid-anchored LeX at 6.0 nm and 6.5 nm local separations: the smaller tilt angle results in more contacts between the

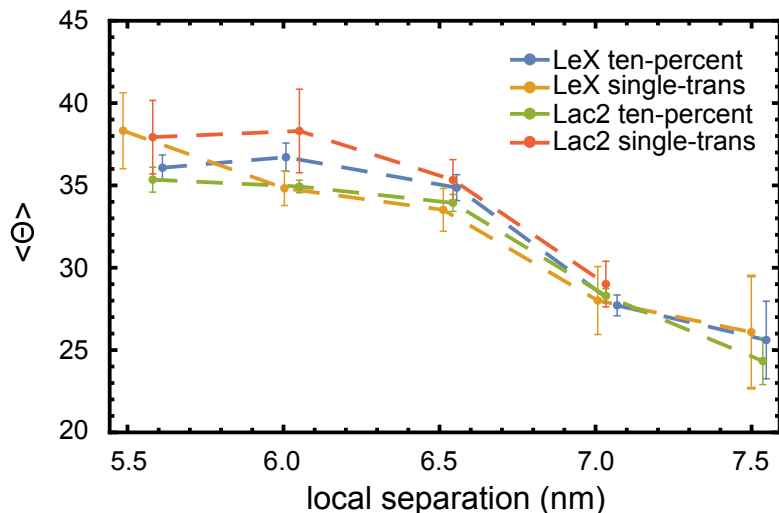


Figure 4.15: The average tilt angle for the lipid-anchored LeX and Lac2 as a function of the local separations. The tilt angle is defined as the angle between the membrane normal (z -axis) and the axial vectors of the lipid-anchored saccharides. For the lipid-anchored LeX the axial vector is between the glucose and the center of mass of the galactose and fucose residues. For the lipid-anchored Lac2, the axial vector is between galactose-2 and glucose-1 (Ch. 4.2). For comparison, we plot the results for ten-percent and single-*trans* systems. The average tilt angle is calculated as the mean of the tilt angle over the ten independent trajectories at each local separation. The errors are calculated as the standard error of the mean over ten independent trajectories.

lipid-anchored saccharides at a given local separation. Moreover, at all local separations, the lipid-anchored Lac2 in ten-percent system has smaller tilting than in single-*trans* system. This finding gives a molecular description of the observed coupling between the *cis*- and *trans*-binding for the lipid-anchored Lac2 (Fig. 4.14): in ten-percent system the lipid-anchored Lac2 extends towards the opposing leaflet more than in single-*trans* configuration which allows more contacts between the *trans*-engaged lipid-anchored saccharides to be formed. That is, the *cis*-interactions cause the lipid-anchored Lac2 to stay in more upright orientation. As a result, the lipid-anchored Lac2 has a larger binding constant in ten-percent system than in single-*trans* configuration. For the lipid-anchored LeX, the average tilt angles for the ten-percent system and the single-*trans* configuration are similar within the error estimates at all local separation. With the same line of thought, this result provides an explanation for the lack of coupling between *cis*- and *trans*-binding for the lipid-anchored LeX at ten-percent system.

We calculate the probability density function for the electron densities of the lipid-anchored saccharides along the z -axis in ten-percent system to further analyze the coupling between *cis*- and *trans*-interactions. For the electron density profiles, we first align the membranes such that the center of mass of the lipid head groups lies at the origin. With this alignment, the membrane normal is parallel to the z -axis. Then, we calculate

the electron density along the z -axis. For all systems we make sure that the lipid head groups have their maxima at the same z -position. Fig. 4.16 shows the electron density profiles for the lipid-anchored saccharides in single-*trans* and ten-percent systems for different local separations. We only show the results for $z > 0$ as the electron density profiles are symmetric with respect to z -axis. The full lines correspond to the single-*trans* system and dashed lines correspond to ten-percent system. We normalize the electron density profiles of the lipid head groups and the lipid-anchored saccharides such that the total electron density is 1. This normalization is required as ten-percent and single-*trans* system contain different number of lipid-anchored saccharides and lipid head groups. At all local separations, we observe that the lipid-anchored Lac in ten-percent system extends out of the membrane more than in single-*trans* system. These differences are most pronounced at 6.0 nm, 6.5 nm, and 7.0 nm local separations. Recalling from Fig. 4.14, at these local separations we observe the positive coupling between *cis*- and *trans*-binding for the lipid-anchored Lac2 the strongest. For the lipid-anchored LeX, on the other hand, the differences in the electron densities between single-*trans* and ten-percent systems are small compared to the lipid-anchored Lac2. Our main conclusion from Fig. 4.16 is that, for the lipid-anchored Lac2, the coupling between *cis*- and *trans*-interactions results in lipid-anchored Lac2 extending towards the opposing leaflet than in single-*trans* system where there are no *cis*-interactions. As a result, in ten-percent system, the lipid-anchored Lac2 from opposing leaflets can interact stronger compared to the single-*trans* system. However, we do not observe such effects in the lipid-anchored LeX, which is in line with our results pointing that there is no coupling between *cis*- and *trans*-binding in lipid-anchored LeX.

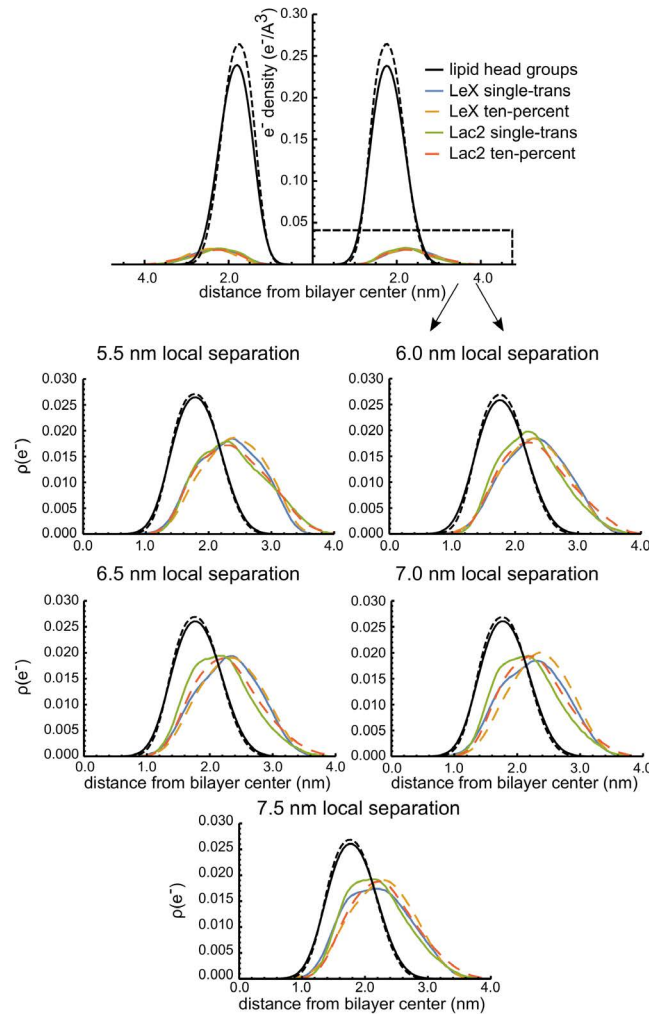


Figure 4.16: Electron density profiles and probability distribution for the electron densities along the z -axis of the lipid-anchored saccharides and lipid head groups in ten-percent and single-*trans* configurations for different local separations. Top figure shows the full electron density profile for the lipid-anchored saccharides at 6.0 nm local separation. Remaining figures are the probability distributions of the electron density profiles. The electron density profiles are calculated after aligning each membrane such that the center of mass of the lipid head groups is at the origin. Furthermore, we align the peaks of the lipid head groups for each system to be at the same z position. For the lipid-anchored saccharides, we only show the electron densities for the saccharide units without the glycolipid linker. The full lines correspond to single-*trans* system and dashed lines correspond to ten-percent system. All electron density profiles (except the top figure) are normalized such that total electron density is 1. The black curves are electron densities of the lipid head groups. We only show the results for $z > 0$.

4.4 Summary

In this chapter, we have studied the binding of lipid-anchored saccharides in planar membranes using a self-interacting bilayer setup. The binding of lipid-anchored saccharides in planar membranes can occur in three distinct categories: i) the lipid-anchored saccharides interact only in-plane, i.e. only the *cis*-interactions between lipid-anchored saccharides from the same membrane leaflet are present, ii) the lipid-anchored saccharides from opposing membrane leaflets can interact have only *trans* interactions in the absence of the *cis* interactions, iii) multiple lipid-anchored saccharides undergo binding in the simultaneous presence of the *cis*- and *trans* interactions.

In order to study the *cis*-interactions, we construct a self-interacting bilayer with two lipid-anchored saccharides in one leaflet and none in the other. As the local separation does not affect the binding, we keep the local separation constant. Our calculations yield the *cis*-binding constant for the lipid-anchored LeX and Lac2 as $K_{2D,LeX}^{cis}=9.87\pm 1.31$ nm² and $K_{2D,Lac2}^{cis}=1.64\pm 0.41$ nm². We further observe that the lipid-anchored LeX and Lac2 has a average tilt angles of 50° and 55° with the membrane normal, respectively. We also show that the *cis*-binding of the lipid-anchored saccharides is diffuse and do not contain any well-defined bound structures.

We study the *trans*-interactions of the lipid-anchored LeX and Lac2 by adding one lipid-anchored saccharide to each membrane leaflet. Again, we allow the lipid-anchored saccharides from different leaflets to interact through the periodic boundaries. In order to understand how the local separation affects the *trans*-binding constant $K_{2D}^{trans}(l)$ we vary the local separation from 5.5 nm to 7.5 nm with 0.5 nm increments. For each separation we calculate the *trans*-binding constant $K_{2D}^{trans}(l)$ and find that for both of the lipid-anchored saccharides the *trans*-binding constant decreases monotonically with increasing separation. We show that the reason behind this behavior is the diffuse binding of the lipid-anchored saccharides, which is omnipresent in all of the saccharide systems we have studied in this thesis. In terms of the magnitude, both lipid-anchored LeX and Lac2 have similar $K_{2D}^{trans}(l)$ values. We calculate the average tilt angle between the membrane normal and the axial vectors of the lipid-anchored saccharides as a function of the local separation. We show that the average tilt angle for the bound states decreases with increasing separation as the lipid-anchored saccharides need to extend more when engaged in *trans*-interactions as the local separation increases. We further observe the trends in the average tilt angle correlates well with the binding constant $K_{2D}^{trans}(l)$.

The ten-percent system we have is to study the possible coupling between the *cis*- and *trans*-binding of the lipid-anchored saccharides. We add ten lipid-anchored saccharides to each membrane leaflet to obtain 10% mol concentration of the lipid-anchored saccharides. We vary the local separation from 5.5 nm to 7.5 nm with 0.5 nm increments to study the affect of the local separation on the binding. We observe that the effective binding

constant $K_{2D}^{eff}(l)$ for the lipid-anchored saccharide is significantly larger than its *trans*-binding constant $K_{2D}^{trans}(l)$ at all local separations, suggesting that there is a positive coupling between the *cis*- and *trans*-binding of the lipid-anchored Lac2. For the lipid-anchored LeX, we do not observe such coupling between the *cis*- and *trans*-binding. By calculating the average tilt angle of the lipid-anchored saccharides in *trans*-engaged bound states, we show that the lipid-anchored Lac2 stays in more upright position in the ten-percent system than in single-*trans* system. On the other hand, we do not observe such a trend in lipid-anchored LeX. We further strengthen our results by calculating the probability distribution of the electron densities of the lipid-anchored saccharides along the membrane normal. We propose the differences in average tilt angle and the electron density profiles for the lipid-anchored Lac2 between ten-percent and single-*trans* systems as a possible explanation of the observed coupling between the *cis*- and *trans*-binding.

Chapter 5

Binding of saccharides anchored in apposing fluctuating membranes

Biological membranes are composed of phospholipid bilayers with embedded molecules. In the liquid-disordered phase, which is the biologically most relevant phase of the membranes, the phospholipid tails are disordered allowing the high flexibility of membranes. Therefore, the membranes can undergo shape fluctuations due to the thermal excitations. In case of parallel aligned sheets of membranes, membrane fluctuations change the local separation between the apposing membrane patches. The overall interactions between the membranes, membrane-anchored molecules, and solvent will influence the local separation. For instance, very low local separations will not be favored due to the hard-core repulsions between the phospholipids (or membrane anchored molecules) and the membranes will be pushed away due to the reordering of the water molecules, which is known as the hydration repulsion.^{64,65}

As the membrane fluctuations change the local separation, it is not possible to talk about one single separation between the apposing membranes but a distribution of them. The probability distribution of the local separations defines the statistical properties of the local separations. The mean value of such probability distribution is defined as the average separation and corresponds to the average distance between the apposing membranes. When the membranes are "free" to change their separation, the average separation will correspond to the separation in which the overall interaction energy between the apposing membranes is minimized. The standard deviation of the probability distribution of the local separations is known as the relative membrane roughness and defines the magnitude of the membrane fluctuations.

The membrane adhesion is mediated by the interactions of the membrane anchored receptors and ligands from the apposing membranes. Membrane fluctuations will change the local separation between the apposing membranes. As a result, a range of local

separations, which can be small or large compared to the length of the receptor-ligand bonds, will be observed. Consequently, the binding of the membrane anchored receptors and ligands will be effected by the presence of the membrane fluctuations: the binding of the membrane-anchored receptors and ligands only occurs in membrane regions with appropriate local separations, in contrast to essentially planar membranes with equal local separations throughout. For example, assume that the average separation between the apposing membranes is slightly larger than the length of the bonds formed between the receptors and ligands. In the case of planar membranes, membrane anchored receptors and ligands will not bind as they will not "see" each other. On the other hand, the membrane fluctuations can bring the apposing membrane patches closer to each other (keeping the average separation constant) allowing the membrane anchored receptors and ligands to interact. Furthermore, the membrane fluctuations requires the bonds formed between the membrane anchored receptors and ligands to withstand the membrane fluctuations. Therefore, when membrane anchored receptors and ligands bind in fluctuating membranes, the number of receptor-ligand complexes will not just depend on the binding strength of the receptor-ligand interactions but also on the relative membrane roughness. For instance, it has been shown that the membrane fluctuations can result in cooperative binding of the membrane anchored receptors and ligands.^{51,66} The reason behind that cooperative binding is that the increasing bond concentration at a certain location on the apposing membranes will smoothen out the membrane fluctuations and will consequently facilitate the binding of additional receptors and ligands. Such cooperative binding due to the constrained membrane fluctuations is not present in planar membranes.

The primary experimental study that motivates this chapter comes from the neutron scattering experiments on the solid-supported membrane stacks doped with the lipid-anchored LeX.²⁵ In this particular setup, the membranes are allowed to fluctuate as a results of the thermal excitations and free to adjust their periodicity. In these experiments, the authors have studied the membrane separation and roughness mediated by the lipid-anchored LeX using specular and off-specular neutron scattering. In the experimental setup, they have varied the molar fraction of the lipid-anchored LeX and measured the lamellar periodicity (the average separation between the apposing membranes). Their results have shown that the lamellar periodicity depends on the molar fraction of the lipid-anchored LeX: increasing the molar concentration of the lipid-anchored LeX results in the lamellar periodicity to converge to ≈ 7.7 nm (the resolution of the experiments were a few Ångstroms). In the same work, they used a continuum mechanical model to describe the fluctuations of the interacting membranes and experimentally determined the membranes' bending rigidity and interaction parameters. Within this continuum mechanical framework, the relative membrane roughness in the present definition, $g_1(0)$, is ≈ 0.7 nm (see Eq. 2 and Table 2 in reference ²⁵). In this chapter, we are aiming to shed light onto the molecular mechanics of the *trans*-binding of the lipid-anchored LeX and the importance of membrane fluctuations in membrane adhesion.

In this chapter, we are studying the binding of the lipid-anchored saccharides in apposing fluctuating membranes. Our first aim is to calculate the probability distribution of the local separation and consequently the average separation and the relative membrane roughness. Our second aim is to obtain the binding constant for the *trans*-engaged lipid-anchored saccharides at a fixed average separation and understand the effect of the membrane fluctuations on the binding constant. Our last aim is to understand the correlations between the positions of the lipid-anchored saccharides and the local separation to see whether binding is cooperative such that the lipid-anchored saccharides get enriched in membrane patches of suitable local separation.

In order to incorporate membrane fluctuations in our simulations, we construct two lipid bilayers with lipid-anchored LeX (Fig 5.1). Each of the monolayers contains 810 POPC lipids and 90 lipid-anchored LeX resulting in total numbers of 3240 POPC lipids and 360 lipid-anchored LeX molecules. This choice of the number of lipids and lipid-anchored LeX corresponds to a 10 mol percent concentration of the lipid-anchored LeX, which is in the range of lipid-anchored LeX concentrations used in the experiments. We adjust the box height such that the membrane leaflets from apposing membranes can interact through the periodic boundary conditions. This setup creates two interfaces between the apposing membranes. We set the box height to 15.5 nm by including 70000 TIP5P water molecules in both interfaces so both of the interfaces have the same average height. With this choice of the box height, the average separation between apposing membranes becomes approximately 7.75 nm, which is the experimentally observed average separation. The overall size of the simulation box is approximately 25 nm \times 25 nm in xy -plane and 15.5 nm in the z -direction with \approx 1200000 atoms. With this setup, we run ten independent trajectories, each starting from the same planar configuration, (Table 5.1) for 900 ns to 1100 ns. In total, we have simulation data corresponding to \approx 10 μ s. At this size of the membranes and the simulation times, the spatial and time correlation functions for the fluctuations in the local separation decay to zero (see Appendix C). The overall simulation time for each trajectory is roughly 300 days. The results presented in this chapter, therefore, come from ten independent simulations of in total 3000 days of simulation time.

One important aspect in our simulations that requires further elaboration is the presence of membrane fluctuations. We adjust the box height in our simulations of the apposing fluctuating membranes such that the lipid-anchored saccharides will also be able to interact with each other through the periodic boundaries. However, in contrast to our simulations of the planar membranes (Ch. 4.1, 4.2, 4.3), in this particular setup, the interactions between the lipid-anchored saccharides is not from the self-interactions of the same membrane. Instead, we have two membranes and the interactions are between the apposing leaflets that are adjacent through the periodic boundaries. In this setup, we have two interfaces in which the binding of the lipid-anchored saccharides can occur. The local separations at these interfaces are given as the local separations of the

membrane-mid planes. Due to the periodic boundary conditions, the sum of the local separations for the two interfaces must be equal to the height of the simulation box. Therefore, membranes can fluctuate at both of the interface subjected to the constraint imposed by the periodic boundaries.

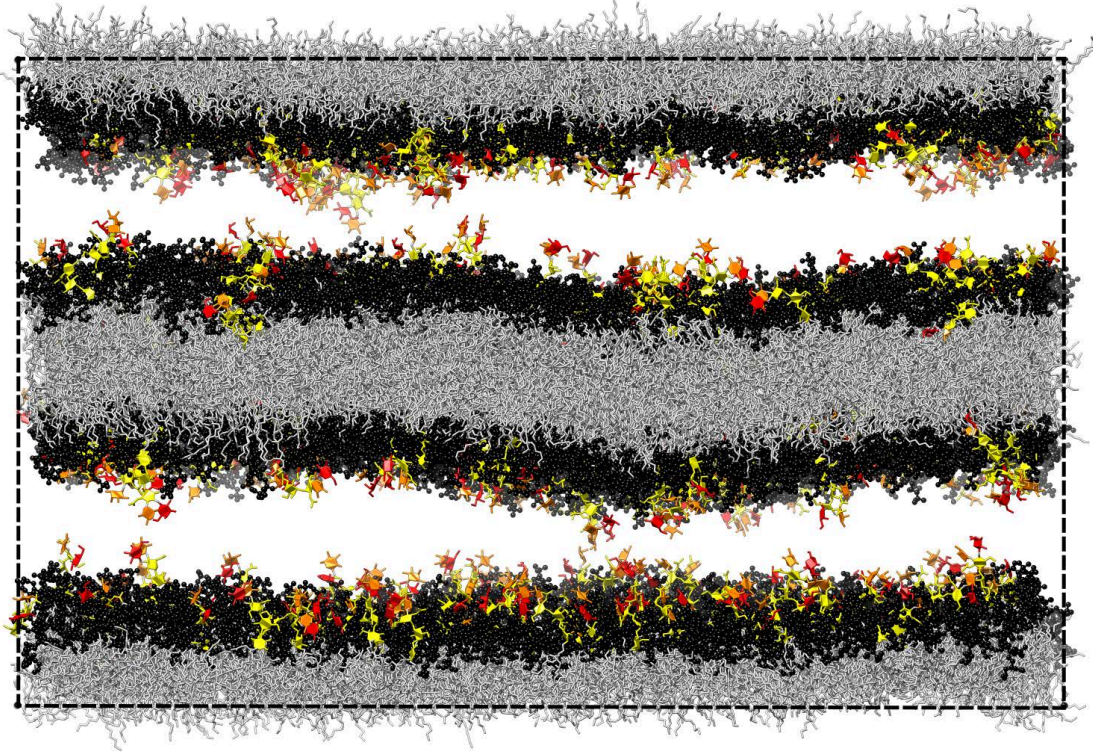


Figure 5.1: Last frame of one of the independent trajectories. Lipid head and tail groups are colored in black and gray, respectively. Fucose and galactose units of the LeX glycolipid are shown in red and orange, respectively. The rest of the glycolipid is colored in yellow. The simulation box is drawn in dashed lines.

Trajectory 1	990 ns	Trajectory 6	996 ns
Trajectory 2	954 ns	Trajectory 7	1014 ns
Trajectory 3	1078 ns	Trajectory 8	1107 ns
Trajectory 4	1122 ns	Trajectory 9	1108 ns
Trajectory 5	987 ns	Trajectory 10	1068 ns

Table 5.1: The length of ten independent trajectories for the apposing fluctuating membrane simulations

This chapter, which presents our results from the simulations of lipid-anchored saccharides anchored in apposing fluctuating membranes is organized as follows: we first

discuss the local separation, i.e. the distance between apposing membrane patches, and its standard deviation, relative membrane roughness. Then, we analyze the binding of lipid-anchored saccharides and report the binding constant K_{2D} . Finally, we discuss the clustering of lipid-anchored LeX in the context of correlations between the lipid-anchored LeX tails and the local separation.

5.1 Membrane fluctuations and the relative membrane roughness

In our simulations with apposing fluctuating membranes, the local separation l , i.e. the distance between apposing membrane patches changes both in space and time. Such fluctuations are readily visible from the last frames of the simulated trajectories (Fig. 5.2). The changing local separation in the trajectories results in a distribution of the local separations $P(l)$. The average separation, which is the experimentally observed distance between the apposing membrane leaflets can be obtained as the first moment (mean) of the distribution of the local separations $P(l)$. The relative membrane roughness ξ_{\perp}^* is defined as the standard deviation of the local separation and can be calculated as the second moment of the $P(l)$. Both the average separation and the relative membrane roughness are equilibrium properties of the membranes. Therefore, we first discuss the relaxation and equilibration of our trajectories.

In order to calculate the local separation l , we discretize each of the leaflet's xy -plane by applying a square grid composed of 16×16 grid cells. This discretization results in four grids. Our selection of the number of grid cells corresponds ≈ 1.5 nm length for the edges for the grid cells and ≈ 2.25 nm² average area of each cell. Given the area per lipid of POPC lipids at 303 K is 0.64 nm², every grid cell can accommodate up to four lipids. It is important to note that we are applying the same grid size to every leaflet such that the grids extend between the maximum x - and y -coordinates of the simulation box at each trajectory frame. We update the edge length of each grid cell for every trajectory frame to keep the total number of grid cells constant. We calculate the average z -position of each grid cell as the average z -coordinate of the center of mass of the lipid tails, including the tails of the lipid-anchored LeX within the same grid cell. The average z -position of the mid-plane grid cells for each membrane, then, can be calculated as the average z -position of the opposing grid cells of the same membrane. These two grids located at the mid-plane of each membrane form the basis of the calculation of the local separation. We calculate the local separation l as the distance between apposing mid-plane grid cells of the membranes. As we have two interfaces, we obtain two values for local separation l . The sum of the local separations for each interface l_1 and l_2 is the height of the simulation

*In the continuum mechanical model to describe the fluctuations of the interacting membranes,²⁵ the relative membrane roughness corresponds to membrane displacement correlation function $g_1(0)$.

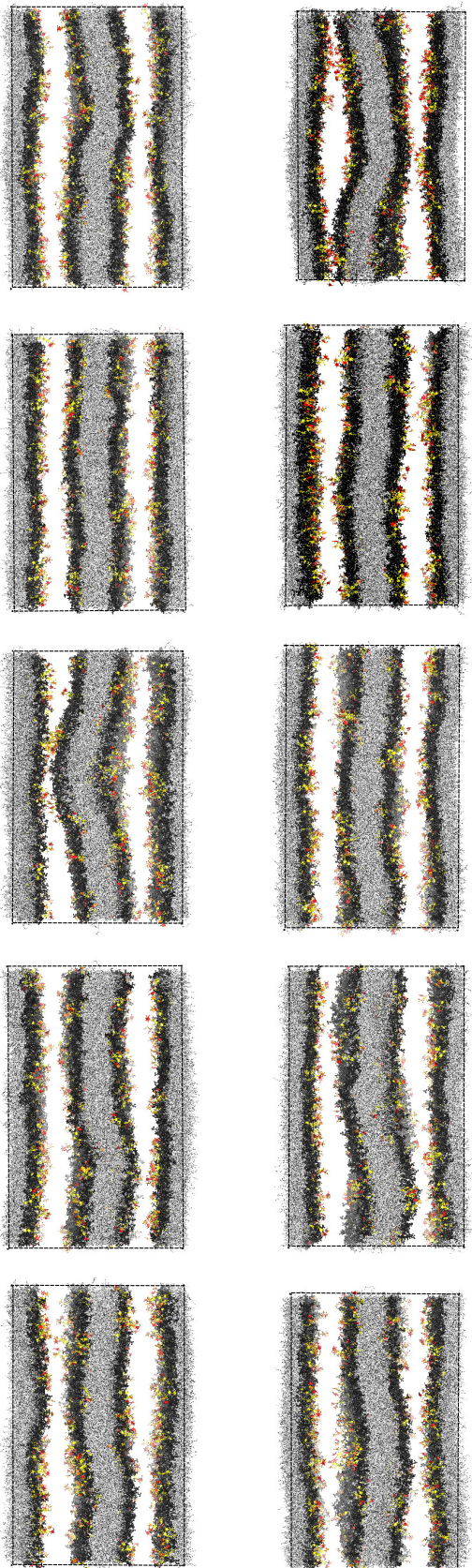


Figure 5.2: The snapshots of the last frames for each independent run. The simulation box is drawn in dashed lines. In order to increase the visibility of the both interfaces, we translate one of the leaflets by the box height in z -direction. Lipid head and tail groups are colored in black and gray, respectively. Fucose and galactose units of the lipid-anchored LeX are shown in red and orange, respectively. The rest of the lipid-anchored LeX is colored in yellow.

box. This results in 512 ($16 \times 16 \times 2$) values for the local separation at each trajectory frame. Finally, we obtain the distribution of the local separation $P(l)$ as the distribution of the local separation values l_1 and l_2 in every frame of our independent trajectories. The average separation \bar{l} and the relative membrane roughness ξ_{\perp} are obtained as the first and the second moments of the $P(l)$ for each trajectory separately.

The relative roughness is the standard deviation of the distribution of the local separation $P(l)$. It is an equilibrium property of the membranes and therefore calculated after averaging the local separation both in time and space. In order to check how the relative roughness evolves in time, we can calculate the instantaneous relative roughness as the standard deviation of the distribution of local separation for a given trajectory frame. Fig. 5.3 shows how the instantaneous relative membrane roughness varies as a function of time. Since each trajectory has been generated by initially planar membranes and heated up to 303 K, the initial relative roughness values are small (≈ 0.1 nm). As the trajectories evolve in time, the instantaneous relative roughness increases steadily and starts fluctuating after it reaches to the equilibrium point. We can define the relaxation time of the relative membrane roughness as the time required to reach to the equilibrium value. In our trajectories, we observe that the instantaneous relative membrane roughness reaches to its equilibrium value (horizontal dashed line in Fig. 5.3) approximately after discarding the first 150 ns of each trajectory (vertical dashed line in Fig. 5.3). That is, it takes approximately 150 ns for the instantaneous relative roughness to reach its equilibrium value. After discarding the first 150 ns of each trajectory, we calculate the relative membrane roughness as $\xi_{\perp} = 0.59 \pm 0.03$ nm. This result is in good agreement with the experimentally calculated relative membrane roughness ≈ 0.7 nm.

After discarding the first 150 ns of each trajectory as equilibration, we continue to calculate the distribution of the local separation $P(l)$. Fig. 5.4 shows how the local membrane separation is distributed for all trajectories. We use a bin size of 0.1 nm when calculating the distribution and obtain the errors as the standard error of the mean from ten independent trajectories. We observe that $P(l)$ can be well approximated by a Gaussian distribution

$$P(l) \approx \frac{\exp[-(l - \bar{l})^2 / 2\xi_{\perp}^2]}{\sqrt{2\pi}\xi_{\perp}} \quad (5.1)$$

where \bar{l} is the average membrane separation and ξ_{\perp} is the relative membrane roughness (red curve in Fig. 5.4). Both quantities can be calculated directly from the trajectories and from the best-fitting Gaussian distributions. After averaging over all trajectories, we find the average separation as $\bar{l} = 7.728 \pm 0.003$ nm. \bar{l} and ξ_{\perp} from the best-fitting Gaussian distributions yield $\bar{l}_{fit} = 7.719 \pm 0.003$ nm and $\xi_{\perp, fit} = 0.594 \pm 0.025$ nm, respectively. The good agreement between the calculated and fitted values confirms our observation that the distribution of local separation can be well approximated by a Gaussian distribution. Table 5.2 summarizes the calculated average membrane separation \bar{l} and the relative membrane roughness ξ_{\perp} both directly from the trajectories and the best-fitting

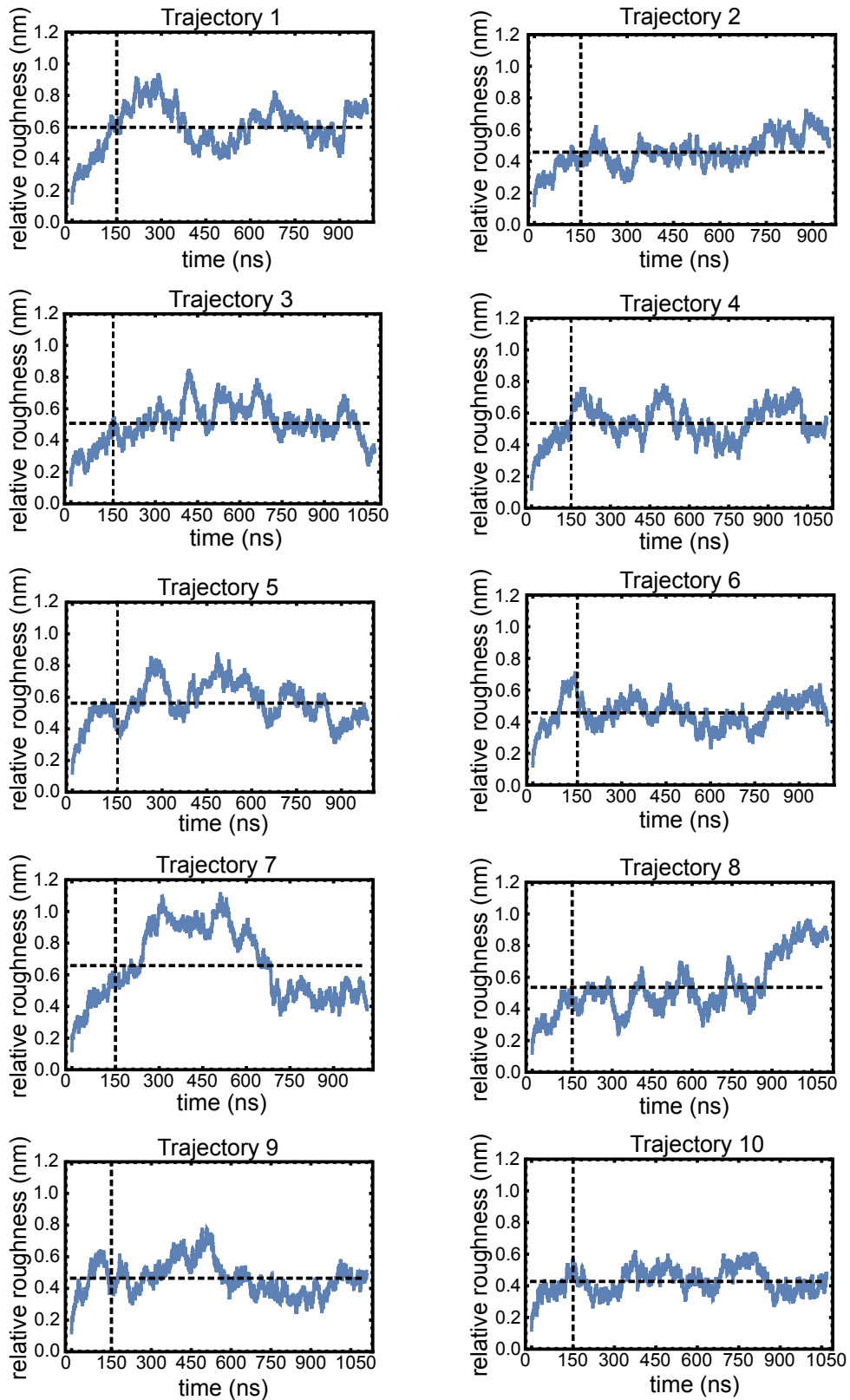


Figure 5.3: The relative membrane roughness ξ_{\perp} calculated for each trajectory. Vertical dashed line at 150 ns marks the portion of the discarded trajectories. Horizontal dashed line shows the mean relative membrane roughness per frame calculated from each trajectory after discarding the first 150 ns of the trajectory. All plots start from non-zero initial relative membrane roughness due to the heating step prior to the production runs.

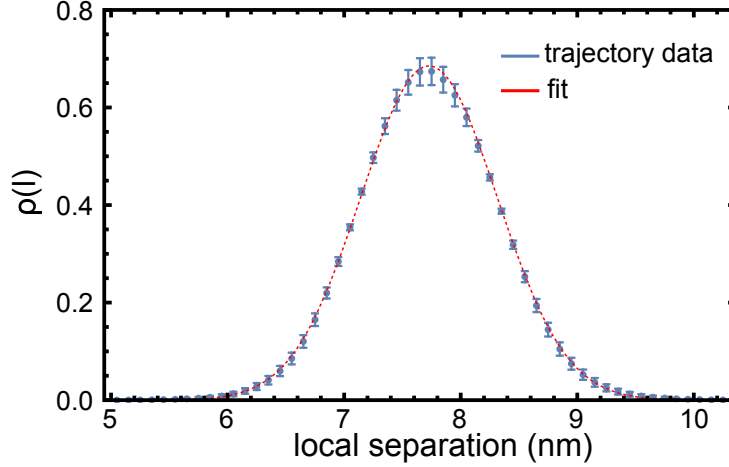


Figure 5.4: The probability distribution $P(l)$ of the local separation averaged from each trajectory (blue) and the best-fitting Gaussian distribution (red). We apply a 0.1 nm bin width when calculating $P(l)$. The errors are calculated as the standard error of the mean for each bin point over ten independent trajectories. The best-fitting Gaussian is obtained by fitting to the overall $P(l)$ from ten trajectories.

	Average local separation \bar{l} (nm)	Relative membrane roughness ξ_{\perp} (nm)
Data	7.728 ± 0.003	0.586 ± 0.029
Fit	7.719 ± 0.003	0.594 ± 0.025

Table 5.2: The average local separation \bar{l} and relative membrane roughness ξ_{\perp} calculated over ten independent trajectories (data) and best-fitting Gaussian distributions of each trajectory (fit). The errors are calculated as the standard error of the mean for each variable over ten independent trajectories.

Gaussian distributions after discarding the first 150 ns of the trajectories.

5.2 Binding of lipid-anchored saccharides

The binding of lipid-anchored saccharides in apposing fluctuating membranes differs from in planar membranes as the local separation between apposing membranes is not constant. Apposing lipid-anchored saccharides can only bind if i) the lipid-anchored saccharides from apposing membranes are in close vicinity of each other in xy -plane, ii) the local separation at that membrane patch allows lipid-anchored saccharides to interact.

The experimentally observable two-dimensional overall binding constant K_{2D} for the binding of lipid-anchored saccharides (of the same kind) is given as

$$K_{2D} = \frac{[L - L]_A}{[L]_A[L]_A} \quad (5.2)$$

where $[L-L]_A$ and $[L]_A$ are the surface concentrations of the bound (*trans*-engaged) and unbound lipid-anchored saccharides. Assuming *trans*-engaged lipid-anchored saccharides are formed with one single *trans*-bond, following Ch. 4.3 we can express Eq. 5.2 for 90 lipid-anchored saccharides at each leaflet as

$$K_{2D} = A \frac{n}{(90 - n)^2} \quad (5.3)$$

where A is the area of the simulation box and n is the number of *trans*-bonds approximated as the half of the number of *trans*-engaged lipid-anchored saccharides.

In our simulations of the lipid-anchored saccharides in apposing fluctuating membranes we have two interfaces where the *trans*-binding can occur. In order to calculate the binding constant K_{2D} using Eq. 5.3, we first calculate the number of *trans*-bonds per frame per interface. We observe that the number of *trans*-bonds per frame is small (≈ 0.25 *trans*-bonds per frame per interface) although we have a large number of lipid-anchored saccharides. We calculate the overall binding constant K_{2D} for each interface and trajectory separately. We obtain the K_{2D} as $0.024 \pm 0.009 \text{ nm}^2$ by averaging over all interfaces and trajectories. We calculate the error by propagating the error in the number of *trans*-bonds n using $err = (\partial K_{2D} / \partial n) s_n$ where s_n is the standard error of the mean of the number of *trans*-bonds over ten trajectories.

It is important to note that, at the average separation of 7.7 nm, we obtain the K_{2D} as $0.024 \pm 0.009 \text{ nm}^2$. Comparing this value to the $K_{2D}(l)$ of 7.5 nm local separation from Ch. 4.3 ($K_{2D}(7.5) = 0.0013 \pm 0.0001 \text{ nm}^2$) we see that the binding constant in apposing fluctuating membranes is significantly larger than in planar membranes with the same separation. This result demonstrates that membrane fluctuations play an important role in the *trans*-binding of the lipid-anchored saccharides at average membrane separations which are seemingly too large for effective binding.

In order to further investigate the binding of lipid-anchored saccharides, we calculate the distribution of the bound lipid-anchored saccharides as a function of the local separation. The binding of the lipid-anchored saccharides can only occur in the range of local separations that are similar to the length of the lipid-anchored saccharides. Consequently, there will be no bound states for very large separations ($l > 8.0 \text{ nm}$). Therefore, for the bound lipid-anchored saccharides, we expect to obtain a different distribution than of the lipids as shown in Fig. 5.4. To check this, we apply a square grid of $1.5 \times 1.5 \text{ nm}^2$ to each leaflet and calculate the local separation l at each grid cell as described before. Then, we obtain the lateral positions of the bound lipid-anchored saccharides and record the local separation at those particular grid cells. By applying a 0.2 nm bin size, we calculate the probability distribution function of the local separation of the lipid-anchored saccharides. Fig. 5.5 shows the probability distribution of the local separation at the grid cells with bound lipid-anchored saccharides. We see that the binding of lipid-anchored saccharides occur mostly in the range of 6.0 to 7.0 nm. For very small separations we

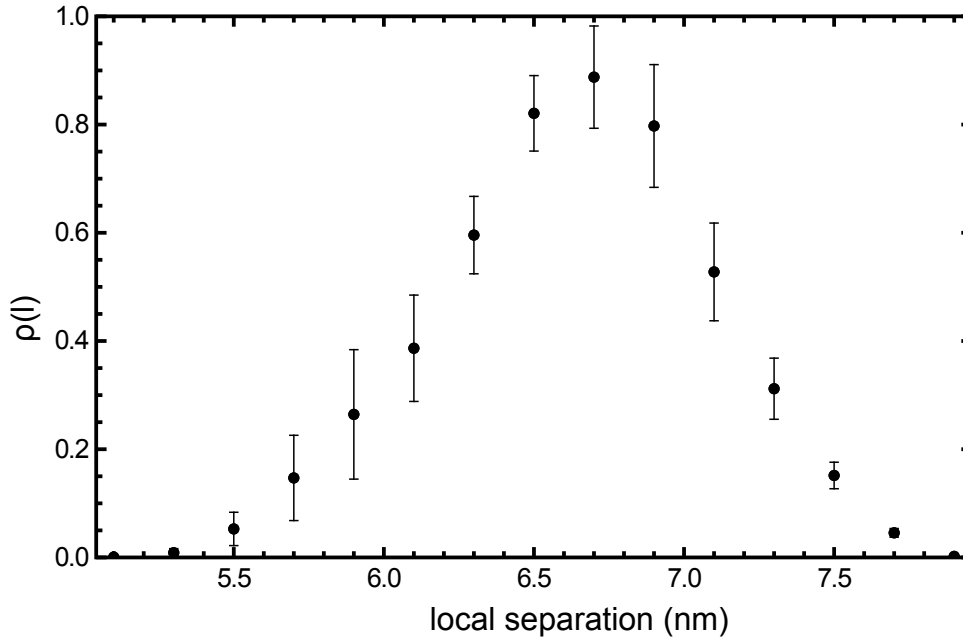


Figure 5.5: The probability distribution for the local separation at the sites of *trans*-bound LeX. Errors are calculated as the standard error of the mean over ten independent trajectories. We apply 0.2 nm bin size when calculating the mean values.

observe virtually no binding as the probability of having small separations is very small. Furthermore, at small local separations the steric repulsions between the lipid-anchored saccharides and the apposing membrane leaflet becomes very strong. These effects in turn make the binding at these small separations unlikely. At large local separations ($l > 7.0$ nm) we also observe low probability of binding as these separations are too large for the lipid-anchored saccharides to form stable bound states, as shown before (Ch. 4.3).

In the simulations of lipid-anchored saccharides in apposing fluctuating membranes, the local separation l is not constant but varies due to the thermal excitations. The overall binding constant, in this case, can also be expressed as³⁸

$$K_{2D} = \int K_{2D}(l)P(l)dl \quad (5.4)$$

where $K_{2D}(l)$ is the binding constant at a given local separation l and $P(l)$ is the equilibrium distribution of the local separation. This equation can be understood as for the overall binding with fluctuating local separations l , the binding at each local separation ($K_{2D}(l)$) will contribute to the overall binding with the probability of $P(l)$. The membrane fluctuations can also lead to the variations of the local orientation of the apposing membranes but contributions of these variations are generally small compared to the variations of the local separation and therefore not included here.⁵⁰

In our simulations of lipid-anchored saccharides in planar membranes (Ch. 4.3) we have calculated $K_{2D}(l)$. Furthermore, we also obtained the equilibrium distribution of

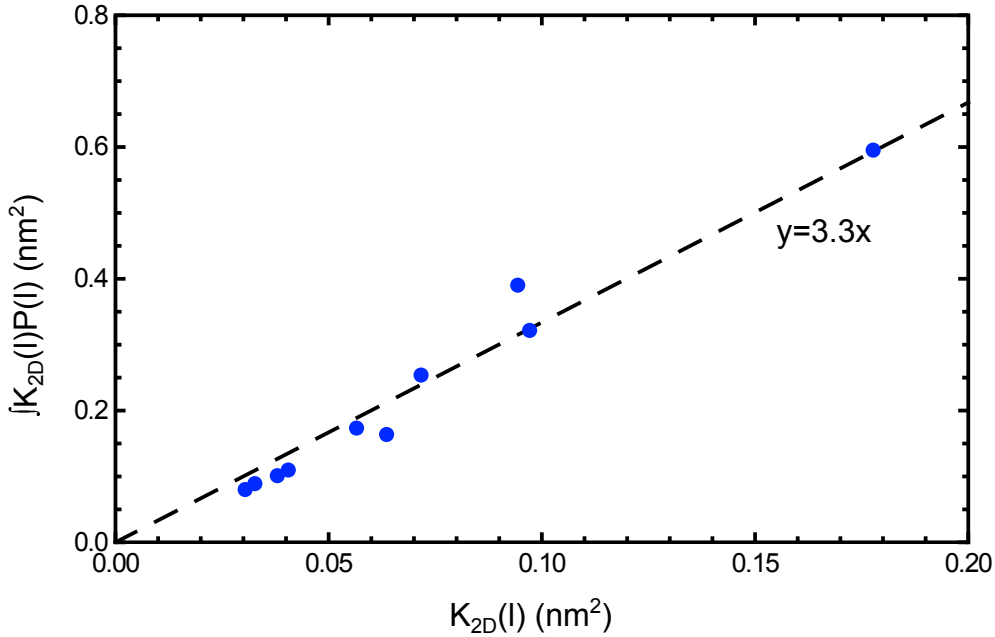


Figure 5.6: K_{2D} values calculated for each trajectory using Eq. 5.3 (x -axis) and Eq. 5.4 (y -axis). The black curve is the best-fitting linear function to the data and has a slope of 3.3 ($R^2 = 0.96$). Our results suggest that the binding constant K_{2D} is systematically overestimated in simulations with self-interacting membranes.

the local separation $P(l)$ (Fig. 5.4). In order to calculate K_{2D} using Eq. 5.4 we first multiply $P(l)$ with $K_{2D}(l)$ at every local separation l where $P(l)$ has a non-zero value. As we have used 0.1 nm bin size when calculating the $P(l)$ and $K_{2D}(l)$ has values only at 5.5, 6.0, 6.5, 7.0, and 7.5 nm, we obtain the intermediate values for the $K_{2D}(l)$ (both mean and error values) by interpolation. This method results in a discrete data set that contains $K_{2D}(l_i)P(l_i)$ at each l_i value (plus the error bars) with a bin size 0.1 nm. We calculate the integral Eq. 5.4 and obtain the binding constant to be $K_{2D}=0.070\pm 0.003$ nm².

The calculated values for the binding constant K_{2D} using Eq. 5.3 and Eq. 5.4 differ by a factor of ≈ 3 from each other (Fig. 5.6). For the simulations of lipid-anchored saccharides in apposing fluctuating membranes, we would expect to obtain similar (if not the same) values using two different approaches as the equivalence of the two methods have been previously demonstrated by Monte Carlo simulations.⁴⁶ However, Fig. 5.6 shows the K_{2D} values calculated for each trajectory from Eq. 5.4 (x -axis) and Eq. 5.3 (y -axis). The black line ($y = 3.3x$) is obtained by fitting the data points to a linear function and has a slope of 3.3. We observe that for all of the trajectories, the K_{2D} using Eq. 5.4 is 3.3 times larger than the K_{2D} calculated by Eq. 5.3. In other words, our planar membrane simulations systematically overestimate the binding constant K_{2D} by a factor of 3.3.

The discrepancy between the K_{2D} values calculated by two different methods needs further attention. Although the reason for the observed difference is not clear, we can

provide a hypothesis to explain it. Our results from Fig. 5.6 suggests that the binding constant $K_{2D}(l)$ is overestimated in self-interacting membranes by a factor of 3.3. From the spatial and correlation functions (see Appendix C) we know that our system size is larger and longer than the correlation length and time of the membrane fluctuations. Therefore, we think that the discrepancy between two results is due to the self-interacting membrane setup. It is possible that we are omitting some entropic factors in planar membrane simulations due to the self-interactions. In order to address this question, we are further simulating the the binding of saccharides anchored to two planar membranes rather than to a single self-interacting membrane. The results from these simulations, however, is beyond the scope of this thesis.

5.3 Saccharide concentrations at different local separations

Fluctuations of membranes due to thermal excitations changes the local separation between the apposing membranes. The varying local separation may result in favorable interactions between lipid-anchored saccharides by bringing them in close contact. It is possible that the lipid-anchored molecules can, either by themselves or by having *cis*-interactions, change the local separation between the apposing membranes.^{2,67-69}

In order to calculate the correlations between the lateral positions of the lipid-anchored saccharides and the local separation, we first apply a $1.5 \text{ nm} \times 1.5 \text{ nm}$ grid to each leaflet same as the discretization we apply for the calculation of the local separation. Then, we select grid cells with at least one lipid-anchored saccharide. We record the number of the lipid-anchored saccharide and the local separation for those grid cells and repeat this procedure for the entire trajectory. Finally, we calculate the average number of lipid-anchored saccharides for a given local separation by using a 0.1 nm bin size. The average number of lipid-anchored saccharides for a given local separation over ten independent trajectories, then, can be calculated as the mean over all trajectories. When a particular local separation l is not explored within a trajectory, we exclude that trajectory at the given local separation l from the calculations. With this procedure, we always get average number densities larger than 1.

Fig. 5.7 shows the average number of lipid-anchored saccharides as a function of the local separation. We observe that the average number of lipid-anchored saccharides between 5.4 nm and 10.0 nm local separations stay the same within the calculated errors. For very large and small local separations, we obtain relatively large errors, indicating that those local separations have not been explored by the lipid-anchored saccharides excessively. Around the local separation 5.2 nm , we observe a small number density for the lipid-anchored saccharides compared to the larger separations. The reason behind this observation can be attributed to the steric factors in which the lipid-anchored saccharides

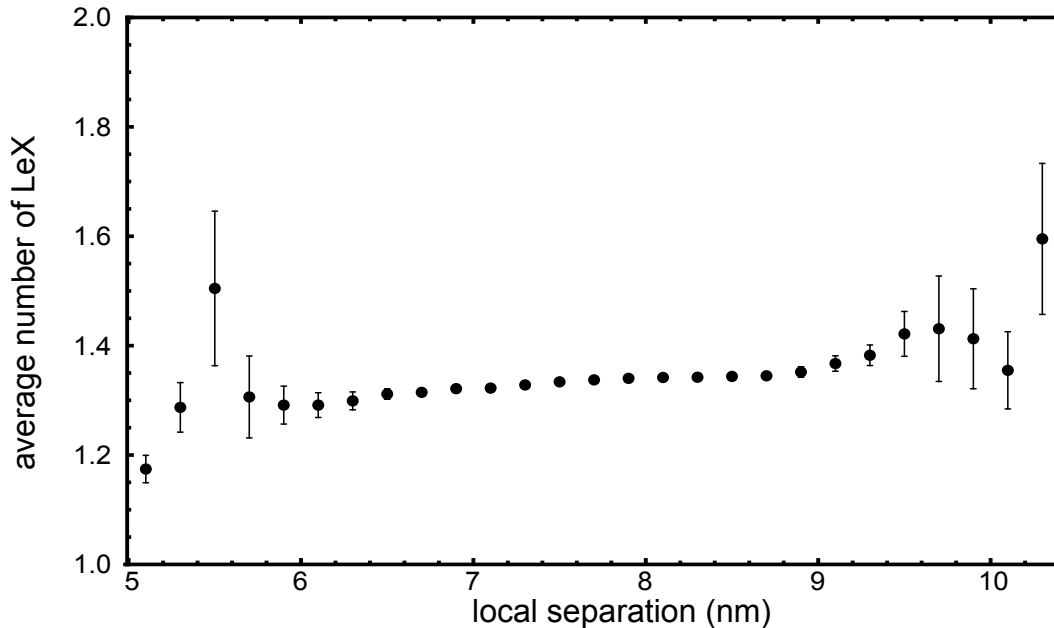


Figure 5.7: The average number density of lipid-anchored saccharides as a function of local separation. The errors are calculated as the standard error for each trajectory and then propagated through all trajectories. Mean values are calculated as the mean over all trajectories. We only consider non-empty grid cells when calculating the mean and the error, i.e. for trajectories in which the specific l have not been explored, we exclude those points from the calculations.

are experiencing strong steric repulsions from the apposing membrane leaflets. Overall, our results do not suggest any correlation between the location of the lipid-anchored saccharides and the local separation. This lack of correlation can be related to a rather weak binding of the lipid-anchored saccharides: the binding forces between the lipid-anchored saccharides are not strong enough induce a redistribution of the lipid-anchored LeX in the same membrane leaflet.

5.4 Summary

In this chapter we have studied the binding of lipid-anchored saccharides in apposing fluctuating membranes with simulations of two membranes. The most important aspect of these simulations is that the lipid bilayers can fluctuate, i.e. the distance between the apposing membrane patches can vary in time and space. With this system, we can study the binding of lipid-anchored LeX in fluctuating membranes and can further assess the importance of membrane fluctuations.

As we are trying to understand the molecular picture of binding that has been observed in the experiments, we set the average separation between the membrane mid-planes of the apposing membranes to 7.75 nm. We first show that the distribution of the local separation $P(l)$ can be well-approximated by a Gaussian distribution. We calculate the

average separation (\bar{l}) and the relative membrane roughness (ξ_{\perp}) from the first and second moments of the distribution $P(l)$ after discarding first 150 ns of the simulations. We observe that the calculated average separation and the relative membrane roughness, both from the trajectories and Gaussian distribution, are in good agreement with the experimental results.

We calculate the binding constant for the *trans*-interactions K_{2D} directly from the simulations. We see that at 7.7 nm local separation, the binding is stronger than in 7.5 nm local separation in planar membranes. This observation is important, as it shows that binding is significant even at large average separations for which the corresponding local separations would be too large for effective binding.

We further calculated the binding constant K_{2D} by integrating the $K_{2D}(l)P(l)$ for all observed local separations. We previously calculated the $K_{2D}(l)$ in planar membranes and we obtain $P(l)$ directly from the our simulations of the apposing fluctuating membranes. We show that the binding constant calculated with this method is around 3 times larger than the K_{2D} values we obtained directly from the simulations. The reason for this discrepancy could be the exclusion of entropic factors due to the self-interacting nature of the membranes. In order to further analyze this discrepancy, we are currently running more simulations of two single bilayers without self-interactions.

Last but not least, we study the possible correlations between the local lipid-anchored saccharide density and the local separation. Our results do not suggest the existence of such correlations.

Chapter 6

Forces on *trans*-bound saccharides in membrane adhesion

Cell adhesion is mediated by the *trans*-binding of membrane anchored receptors and ligands. From a mechanical perspective, it is the forces between the *trans*-bound receptors and ligands that hold the membranes together. The responses upon the force generation regulate many biological processes such as proliferation,⁷⁰ migration,⁷¹ differentiation,⁷² tumor progression⁷³ and tissue formation.⁷⁴

The experimental methods for assessing the adhesion forces can be roughly categorized into single-cell and single-molecule force spectroscopy.⁷⁵ These spectroscopic setups include optical and magnetic tweezers,^{76–79} micropipetting methods,⁸⁰ and atomic force microscopy (AFM).^{81–83} With these setups, forces ranging from ≈ 10 pN to a few hundred nanonewtons can be measured.

Over the last decades, due to the increasing evidence on the role of saccharide-saccharide interactions in membrane adhesion, ^{84–86} the force generation by the binding of saccharides became a new focus of research. A few challenges in the case of saccharides come from the highly diverse structure and low binding affinity of the saccharides.²² To address the force generation by the saccharides, most of the experimental studies anchor saccharides to self-assembled membranes or nanoparticles.^{87–89}

In one study that is particularly important to this work, researchers have investigated the adhesion forces by the LeX saccharide.²¹ In their experimental setup, they have used AFM to quantify the adhesion forces between individual LeX molecules using two dimensional self-assembled monolayers. They have functionalized the gold monolayers with the LeX trisaccharide using an aliphatic chain for anchoring. They also have functionalized the AFM cantilever tip with the LeX trisaccharide. With this setup, they have measured the adhesion forces using the force-distance curves. Their results yielded forces in the entire multiples of ≈ 20 pN, which in turn was assigned to be the binding force between

two LeX trisaccharides. To the best of our knowledge, the adhesion forces for the Lac2 saccharides have not been reported in the literature.

There are a few differences between our simulations and the above described experimental setup that needs attention. In our simulations, the lipid-anchored LeX contains five saccharide units (LeX trisaccharide plus lactose disaccharide). In addition, the glycerol moiety that acts a linker between the saccharide and the aliphatic lipid tails in our simulations is missing from the experimental setup. Consequently, a one-to-one comparison of the forces calculated from our simulations with the experimental setup is not strictly possible. Nevertheless, the mentioned experiments indicate the possible ranges of the forces generated by the LeX trisaccharide.

In this chapter, we present our calculations for the forces generated by the *trans*-binding of the lipid-anchored saccharides in planar membranes. We develop a linear model which assumes that the lipid-anchored saccharides are embedded into the membranes *via* harmonic springs. Through the deviations of the harmonic springs from their equilibrium lengths, we calculate the forces in the *trans*-binding. This chapter is organized as follows: first, we introduce our harmonic model for the force calculation. Second, we present the forces and the energies generated by the *trans*-engaged lipid-anchored saccharides in two different simulation setups. Finally, we report the pressure generated by the *trans*-binding of the lipid-anchored saccharides.

6.1 Harmonic modeling of forces and energies in *trans*-binding

In order to study the forces and energies during the *trans*-binding of the lipid-anchored saccharides, we focus on the fluctuations of the extension between the z -coordinates of the center of mass (COM) of the glycolipid linker and the COM of the lipid head groups (PC). The extension δz between the COM of the glycolipid linker can be obtained by

$$\delta z = z_{linker} - z_{PC} \quad (6.1)$$

where z_{linker} and z_{PC} correspond to the z -coordinates of the COM of the glycolipid linker and lipid PC head groups at a given time point. When there are no *trans*-bound states, the δz will fluctuate around its equilibrium position due to the thermal fluctuations. When there are *trans*-bound states, the fluctuations in the δz will differ from its fluctuations in the unbound states. To understand how the δz fluctuates in the unbound states, we use our simulations of the lipid-anchored saccharides at 8.0 nm local separation as a reference. At 8.0 nm local separation, neither single-*trans* (Ch. 4.1) nor ten-percent systems (Ch. 4.3) have any bound states. For all of these systems, we compute the δz throughout the trajectories and obtain the probability distribution of δz . Fig. 6.1 shows the probability distribution of δz at 8.0 nm local separation for different lipid-anchored

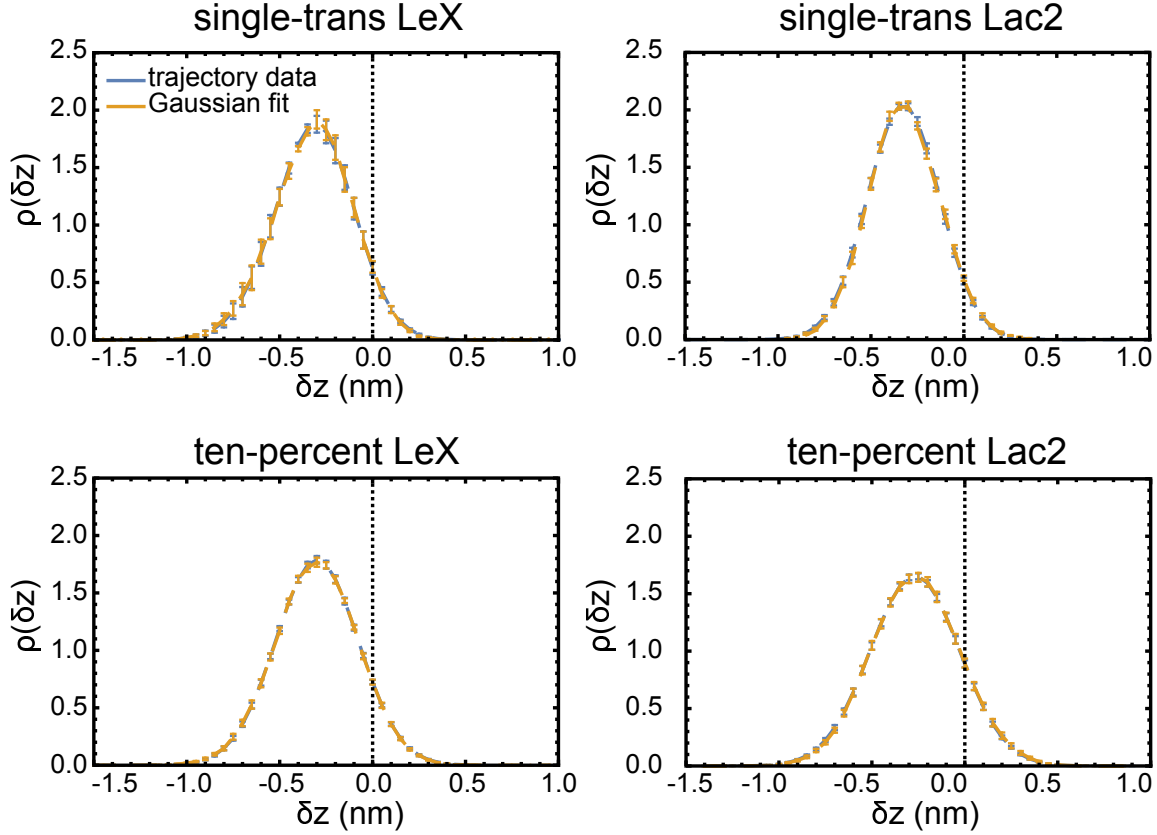


Figure 6.1: The probability distributions for the z-extensions (δz) between the center of mass of the glycolipid linker and the lipid PC head groups at 8.0 nm local separation for four systems studied in this work. We choose the 8.0 nm local separation because there are no bound states in this separation, meaning the fluctuations in the δz will not be affected by the *trans*-binding. The blue curve is calculated directly from the trajectories. The orange curve is calculated by fitting a Gaussian distribution to the trajectory data. The error bars are obtained as the standard error of the mean of the probability distribution over ten independent trajectories.

membrane systems. The blue data points are obtained from the trajectories and the orange data points are computed by fitting a Gaussian probability distribution to the trajectory data. For all systems, we observe that the probability distribution of the extension between the z-coordinates of the COM of the glycolipid linker COM and lipid PC head groups can be well approximated by a Gaussian distribution. This observation indicates that a harmonic approximation to the δz , for extensions or which the Gaussian distribution well approximates the data, is viable.

Following our observation from Fig. 6.1 that the probability distribution of the δz can be well approximated by a Gaussian distribution, we employ a harmonic model to obtain the forces and energies due to the *trans*-binding of the lipid-anchored saccharides. In our model, we assume that the lipid-anchored saccharides are embedded into the lipid membranes *via* harmonic springs (Fig. 6.2). We simply assume that there is a harmonic

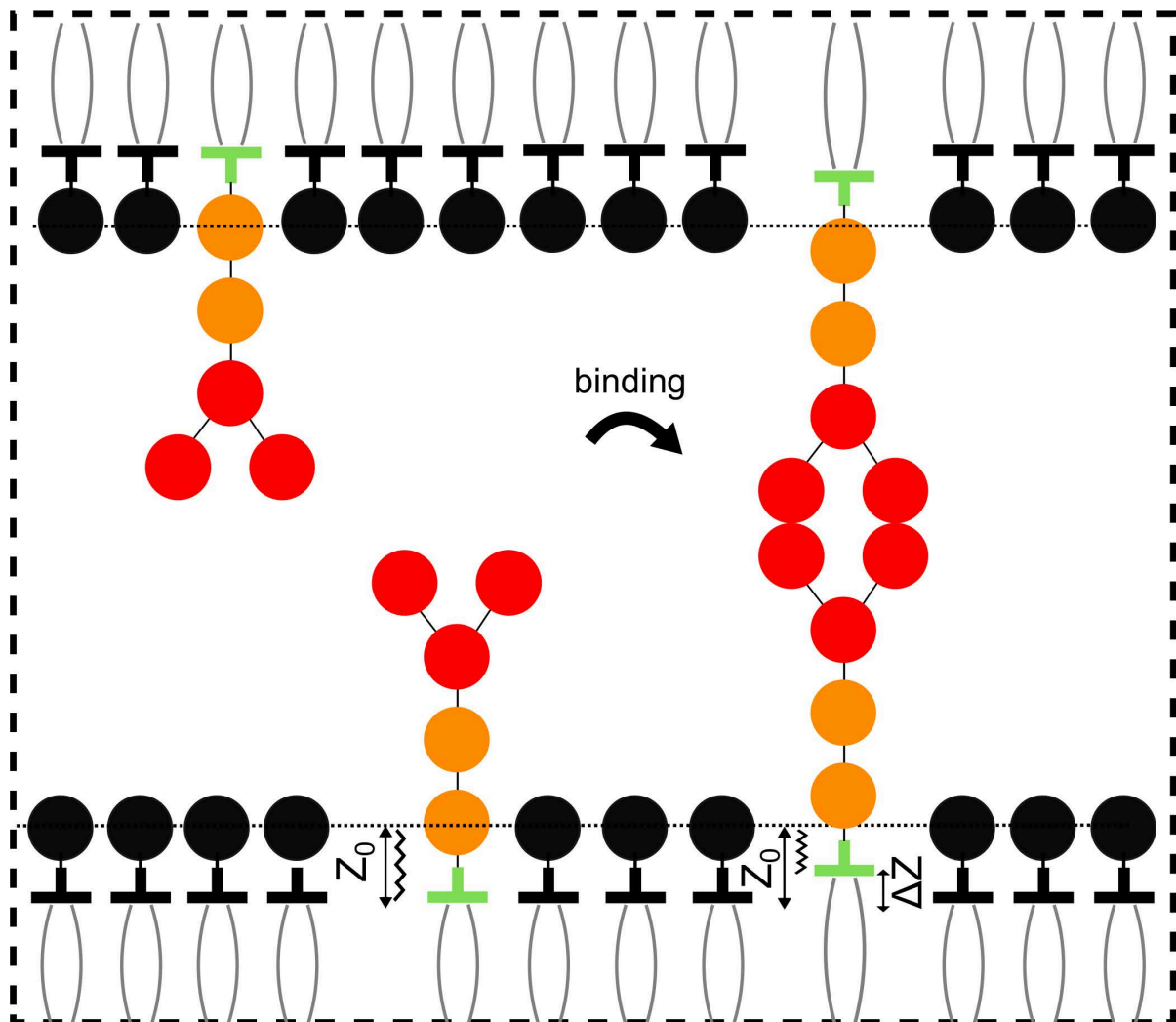


Figure 6.2: Schematic illustration of the force generation by the *trans*-binding of the lipid-anchored saccharides. For demonstration, we show the structure of the lipid-anchored LeX in red (galactose, fucose, and GlcNAc residues) and orange (galactose and glucose residues) beads. The black beads denote the lipid PC (phosphatidylcholine) head groups whereas the glycerol moiety (glycolipid linker) is shown in green. The same glycerol moiety in the lipids is colored in black. Horizontal dashed line corresponds to the z -coordinate of the center of mass of the lipid PC head groups. In our model, we assume that the lipid-anchored saccharides are embedded into the membrane *via* harmonic springs (the black "zig-zag"). The equilibrium length of the spring (z_0) is the mean length of the harmonic spring (δz) for the unbound lipid-anchored saccharides calculated at 8.0 nm local separation. If the local separation is large, the lipid-anchored saccharides can approach to each other due to the forces generated by the *trans*-binding. The forces and the energies on the harmonic springs can be calculated by measuring the deviation in the length of the harmonic spring from its equilibrium length ($\Delta z = \delta z - z_0$).

spring between the center of mass (COM) of the glycolipid linker and the COM of the lipid PC head groups. As a result of the thermal excitations the spring will fluctuate around its equilibrium length z_0 . However, due to the *trans*-binding of the lipid-anchored saccharides, spring can experience a force if the *trans*-binding changes the equilibrium position of the lipid-anchored saccharides. Our aim is to calculate the forces generated during *trans*-binding by measuring the deviations from the equilibrium length of the springs.

For a linear system, the potential energy on the spring is given by

$$V(\delta z) = \frac{k}{2}(\delta z - z_0)^2 \quad (6.2)$$

where δz is the instantaneous spring length defined as $\delta z = z_{linker} - z_{PC}$. In Eq. 6.2, z_0 and k are the equilibrium length of the spring and the spring constant, respectively. The force exerted by the spring in one dimension is the negative of the derivative of the potential with respect to z axis

$$F(\delta z) = -\frac{dV(\delta z)}{dz} = -k(\delta z - z_0) \quad (6.3)$$

When the system is coupled to a heat bath, the probability density of a certain observed spring length δz will be observed is given by the partition function as

$$\rho(\delta z) = \rho_0 \exp[-V(\delta z)/k_B T] \quad (6.4)$$

where ρ_0 , k_B , and T are the normalization factor, Boltzmann constant, and the temperature, respectively. For a harmonic system, the partition function will assume a Gaussian probability distribution as

$$\rho(\delta z) = \rho_0 \exp[-(\delta z - z_0)^2/2\sigma^2] \quad (6.5)$$

where σ is the standard deviation of the distribution.

Solving Eq. 6.4 and Eq. 6.5 simultaneously gives the expression for the spring constant k as

$$k = \frac{k_B T}{\sigma^2} \quad (6.6)$$

By inserting the expression for the spring constant k to Eq. 6.2 and Eq. 6.3, we obtain the potential and the force on the harmonic spring as

$$V(\delta z) = \frac{k_B T}{2\sigma^2}(\delta z - z_0)^2 \quad (6.7)$$

and

$$F(\delta z) = -\frac{k_B T}{\sigma^2}(\delta z - z_0) \quad (6.8)$$

		z_0 (nm)	k (pN/nm)
single-trans	LeX	-0.31 ± 0.03	0.098 ± 0.002
	Lac2	-0.31 ± 0.01	0.102 ± 0.002
ten-percent	LeX	-0.31 ± 0.01	0.085 ± 0.002
	Lac2	-0.36 ± 0.01	0.082 ± 0.001

Table 6.1: The calculated equilibrium length and the spring constant of the harmonic springs for the *single-trans* and *ten-percent* systems.

As a result, the forces and energies on the harmonic spring can be calculated by measuring the instantaneous (per trajectory frame) deviations in the length of the spring from its equilibrium value. Using the distributions shown in Fig. 6.1, we calculate the equilibrium length and the spring constant for the harmonic springs. The equilibrium length is given by the first moment of the Gaussian probability distribution, and the spring constant can be calculated from the standard deviation of the probability distribution using Eq. 6.6. Table 6.1 shows the equilibrium length and the spring constants for the harmonic springs in the planar membrane simulations.

There are two important remarks that we need to make. First, the energies calculated on the harmonic springs do not correspond to the binding energy of the lipid-anchored saccharides. All the energies we present in this chapter are the mechanical energies stored in the springs due to the change in the spring length from its equilibrium length. The binding energy, on the other hand, involves the reorientation of the atoms and the solvent due to the binding and such effects are not included in the mechanical energy stored in the springs. The second remark is that, as we obtain the equilibrium lengths of the springs negative, in our coordinate system positive forces will "push" the lipid-anchored saccharides into the membranes whereas negative forces will "pull" the lipid-anchored saccharides outside the membrane towards the opposing bilayer.

6.2 Forces and energies in *trans*-binding of lipid-anchored saccharides in planar membranes

After obtaining the equilibrium lengths and the spring constants for the harmonic springs, we calculate the forces and energies for the *trans*-bound lipid-anchored saccharides in planar membranes. In this section we first define the bound states and discuss the sensitivity of our results to the different definitions of the bound states. Then, we show that the deviations in the spring length due to the *trans*-binding in planar membranes are still within the linear range of our model. Finally, we calculate the forces and energies generated by the *trans*-bound saccharides in planar membranes.

We define the bound states, in consistency with our results on the binding of lipid-

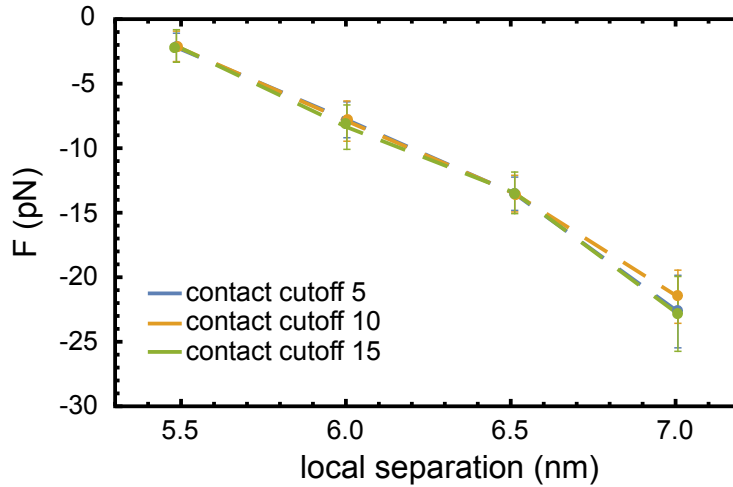


Figure 6.3: The forces generated by the *trans*-binding of the lipid-anchored LeX in single-*trans* configuration with different contact cutoff as a function of the local separation. For different cutoff values, we obtain similar forces. The errors are calculated as the standard error of the mean over ten independent trajectories.

anchored saccharides presented in this thesis, as the contiguous bound intervals in the trajectory with the observed maximum number of contacts is equal to or larger than 5. Although this definition is consistent with our previous definition of the bound states, it is instructive to check the sensitivity of our results to the definition of the bound states. Fig. 6.3 shows how the forces depend on the contact cutoff. Exemplary, we only show the results from the single-*trans* LeX system. For all of the local separations (from 5.5 nm to 7.0 nm with 0.5 nm increments), we observe that the calculated forces (according to the Eq. 6.8) do not change with changing the contact cutoff. Therefore, we conclude that the calculated forces do not sensitively depend on the number of contact cutoff within a reasonable range. In order to be consistent with our previous results, we choose the contact cutoff as 5.

Before we present our results for the forces and energies in *trans*-binding of the lipid-anchored saccharides, we analyze the magnitude of the fluctuations in the harmonic spring lengths in bound states in order to check that the length fluctuations are within the range of fluctuations we used to construct our harmonic model. Fig. 6.1 shows that the equilibrium fluctuations in the length of the springs can be well approximated by a Gaussian distribution in the range of -1.0 nm to 0.3 nm. In order to use our harmonic model, it is important to check if the spring lengths for the bound states fall within the same range -1.0 nm to 0.3 nm, as we then can use the same spring constants we presented in Table 6.1. Fig. 6.4 shows how the length of the harmonic spring δz is distributed for the bound states at different local separations. For comparison, we also show the length distributions we obtained at 8.0 nm local separation (Fig. 6.1). We observe that, for all of the planar membrane systems, the lengths of the harmonic springs at all local separations are within the range of the equilibrium length fluctuations of the harmonic

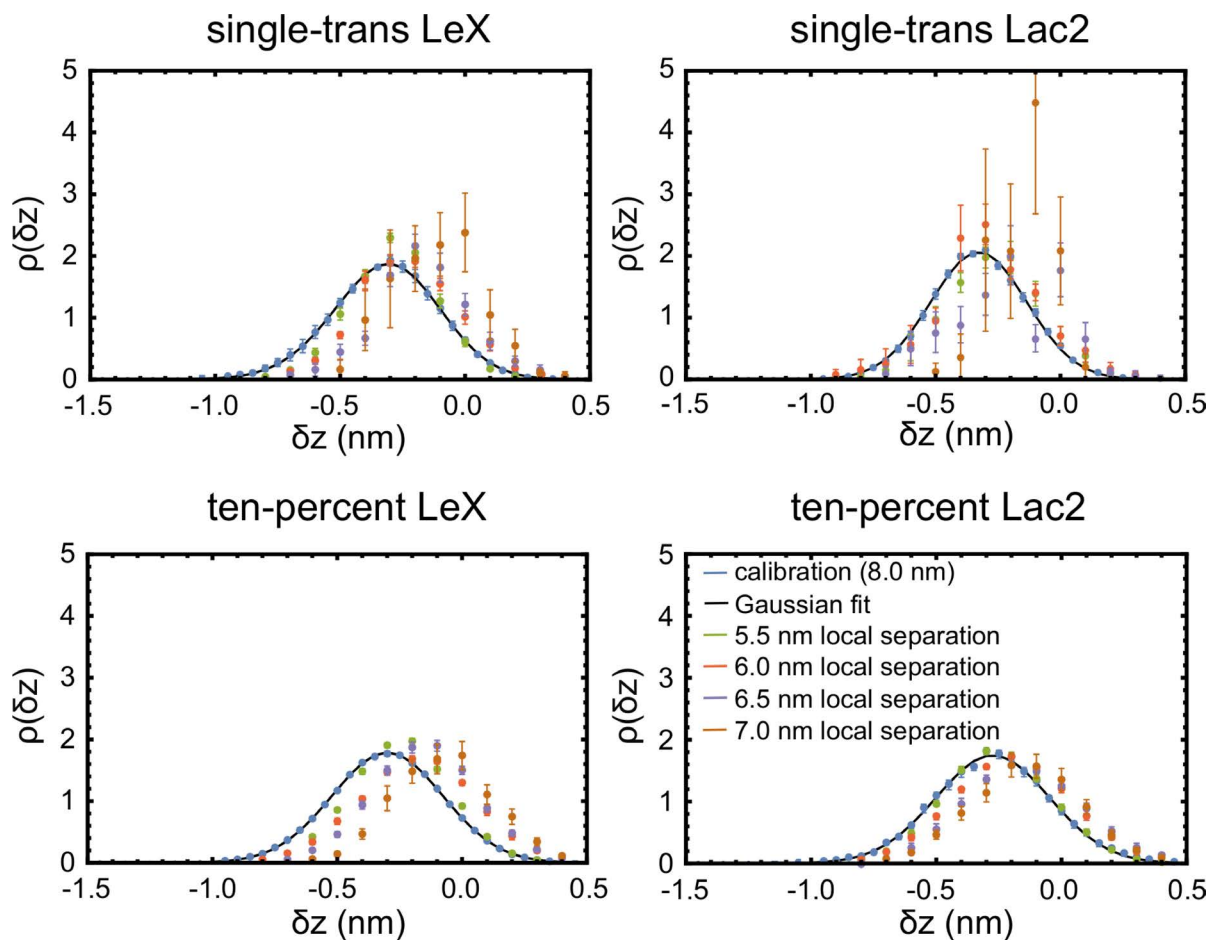


Figure 6.4: The probability distributions of the z -distance between the glycolipid linker and the center of mass of the lipid PC head groups (δz) for different local separations. For comparison, the probability distributions from the 8.0 nm local separation (the calibration calculations) are shown in blue (trajectory data) and black (the best-fitting Gaussian distributions). For all of the studied systems, except ten-percent lipid-anchored LeX, the lengths of the harmonic springs are within the ranges observed at the 8.0 nm local separation. For the ten-percent lipid-anchored LeX system, the probability distributions of the δz for 6.5 nm and 7.0 nm local separations extend beyond the harmonic range. However, these distributions also have very low probabilities beyond the harmonic range therefore we do not expect them to change our overall results. For the lipid-anchored Lac2 in single-*trans* system, we obtain large errors and we do not show half of the error bar in the data point -0.1 nm for 7.0 nm local separation for clarity. These results show that the forces and energies on the springs can be calculated with our harmonic model. The errors are calculated as the standard error of the mean over ten independent trajectories.

springs at 8.0 nm local separation. Only for the ten-percent LeX we have spring lengths in the bound states beyond 0.3 nm where our model fails to capture. However, these points also have very low probabilities, suggesting that failure of our model to capture the forces beyond 0.3 nm spring lengths will not change the overall results presented here. Therefore for all the systems and local separations, the forces and energies on the harmonic springs due to *trans*-binding can be calculated within range of our harmonic model.

For the calculation of the forces and energies, we start with the simplest case of the single-*trans* LeX and Lac2 in planar membranes (Ch. 4.1). We calculate the forces on the bound and unbound states from Eq. 6.8 by measuring the instantaneous (per frame) deviation of the harmonic spring δz from its equilibrium length (Table 6.1). Δz is defined as $\Delta z = \delta z - z_0$ and corresponds to the instantaneous difference of the harmonic spring length from its equilibrium value. Then, we average the forces on each bound and unbound lipid-anchored saccharides over the trajectories. For the energies on the harmonic springs, we first calculate the average δz for a given system over the trajectory, and then calculate the energy on the spring by using the Eq. 6.7. The reasoning behind this method is that, due to the equipartition theorem, there will be $k_B T/2$ energy on each spring just because of the thermal fluctuations. As the potential energy is quadratic, first calculating the energy on each spring and then averaging over the trajectory yields a residual energy of $k_B T/2$ due to the thermal fluctuations. In contrast, when we first average over the spring length δz and then over the deviations from the equilibrium length Δz eliminates the energy contribution from the thermal fluctuations. For all of the local separations, the errors in forces and energies are calculated as the standard error of the mean over ten independent trajectories and by propagating the error in δz , respectively.

Fig. 6.5 shows how the forces and energies depend on the local separation for the lipid-anchored LeX and Lac2 in single-*trans* configuration. Although we have the simulations at 7.5 nm local separation, there are very few bound states and therefore we obtain very large errors. Consequently, we exclude our data points at 7.5 nm local separation from this discussion. We first observe that the unbound states experience almost zero forces and energies. This result is expected as we calibrate our springs without the presence of bound states at 8.0 nm local separation and lack of *trans*-binding results in no significant deviations in the spring lengths beyond the thermal excitations. The bound states, on the other hand, experience significantly larger forces with the increasing local separation than the unbound states. This increase in the forces and energies with increasing local separation can be understood as follows: for small local separations, the height of the water layer between the opposing membrane leaflets ($\approx 1.7 - 2.2$ nm at 5.5 and 6.0 nm local separations) is comparable to the length of the lipid-anchored saccharides (≈ 1.8 nm). Therefore, when bound, lipid-anchored saccharides do not need to extend their z -positions. However, as the local separation increases, the lipid-anchored

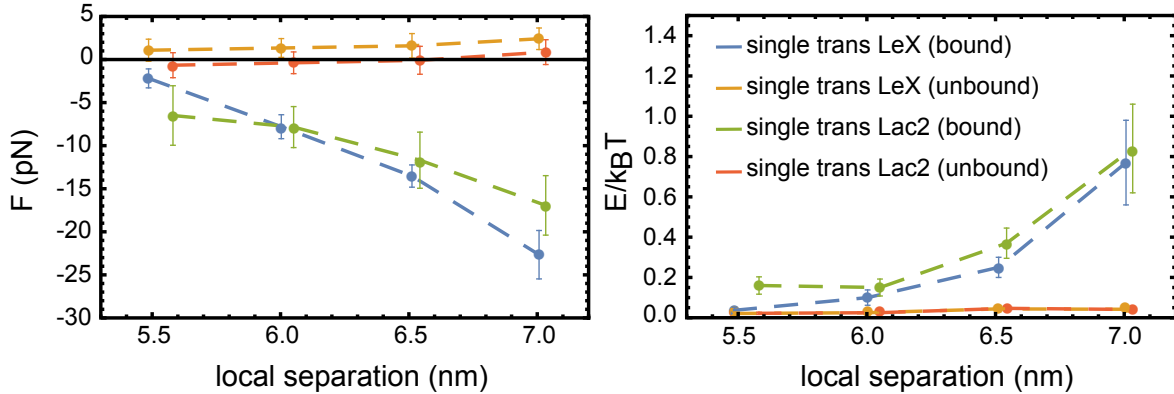


Figure 6.5: The forces (left) and the energies (right) generated the the *trans*-binding of the lipid-anchored LeX and Lac2 as a function of the local separation. The forces are calculated from Eq. 6.8 by measuring the deviations of the length of the harmonic springs from their equilibrium length and then averaging over the trajectories. For obtaining the energies, we first average the length of the harmonic springs over each trajectory and then we subtract the equilibrium length of the springs to eliminate the energy contributions from the thermal fluctuations. Then, we use Eq. 6.7 to calculate the energy on each spring. We obtain average energies by averaging the energies on each spring over the trajectories. The errors for the forces are calculated as the standard error of the mean. For the energies, the errors are calculated by propagating the error in the length of the harmonic springs.

saccharides must extend from their equilibrium z -position towards the opposing leaflet to bind. Larger the local separation, larger the extension in z -position must be. As a result, with increasing local separation the lipid-anchored saccharides experience larger forces that "pulls" them out of the membranes when they are bound. For the unbound states, no such "pulling" is obtained. Our second observation is that the forces and energies generated by the *trans*-binding in single-*trans* configuration is in the order of a few 10 pN and $0.5 k_B T$.

The single-*trans* system represents an isolated case of the binding of lipid-anchored saccharides because there are no *cis*- (in-plane) interactions. When the *cis*-interactions are present, the bound states of the lipid-anchored saccharides can be more complicated than simple *trans*-dimers. For a *trans*-trimer that consists of one *cis*-dimer and one *trans*-dimer for instance, the bound lipid-anchored saccharides can generate different forces than in the single *trans*-dimer case. In order to see if the generated forces by the *trans*-engaged saccharides is affected by the *cis*-interactions, we calculate the forces and energies generated by the lipid-anchored saccharides in ten-percent system (Ch. 4.3). In the ten-percent system, the lipid-anchored saccharides can form *trans*-engaged trimers, tetramers, etc. For instance, a *cis*-dimer formed by two lipid-anchored saccharides in the same leaflet can have *trans*-interactions with another lipid-anchored saccharide from the opposing leaflet, forming a trimer. In order to distinguish between these multimetric states, we further calculate the forces and energies generated by each single *trans*-dimer

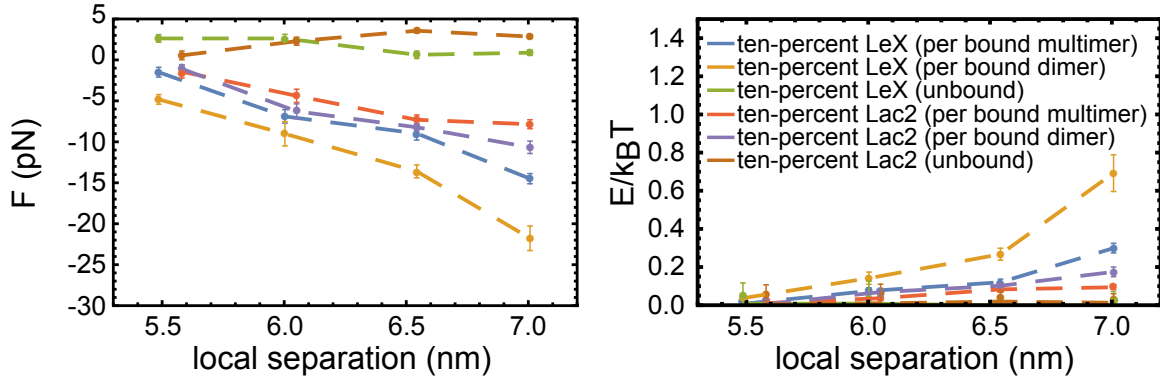


Figure 6.6: The forces (left) and the energies (right) calculated for the ten-percent system as a function of the local separation. For the multimers, we calculate the forces and energies for the *trans*-engaged dimers and higher multimers (trimers, tetramers, ...) separately. We calculate the errors as described in the caption of Fig. 6.5

(only two *trans*-engaged lipid-anchored saccharides) and higher multimers (we use the term "multimer" to denote trimers, tetramers, ...; not dimers). Fig. 6.6 shows our results for the forces and energies generated by the *trans*-engaged dimers, *trans*-engaged higher multimer (denoted as multimers), and the unbound states for the lipid-anchored LeX and Lac2. We observe that, similar to the single-*trans* system, the energies and forces generated per *trans*-engaged state increase with the local separation where the unbound states generate almost no force or energy.

Our second observation from the Fig. 6.6 is, for the ten-percent system, the *trans*-engaged dimers generate larger forces than higher *trans*-engaged multimers for the lipid-anchored LeX. In particular, at 6.5 and 7.0 nm local separations, *trans*-dimers generate ≈ 6 pN more force than the higher multimers. For the lipid-anchored Lac2, our results show similar behavior for the *trans*-engaged dimers and multimers to a lesser extent. One possible mechanism for obtaining lower forces for the lipid-anchored saccharide with higher multimers than in single-dimers is that the forces generated by the *trans*-binding can be shared among the lipid-anchored saccharides forming the multimer. As a result, the force generated per lipid-anchored saccharide can decrease compared to the cases with no *cis*-interactions. However, we do not further investigate his possible mechanism in this thesis.

In order to see how *cis*-interactions change the generated forces and energies compared to the single-*trans* system, we compare our results from Fig. 6.5 and Fig. 6.6. Fig. 6.7 shows the forces and energies generated by the *trans*-binding in single-*trans* and ten-percent systems. For the lipid-anchored LeX, we see that the *trans*-engaged dimers in ten-percent system generate similar forces and energies as the single-*trans* system. The higher multimers of the lipid-anchored LeX, on the other hand, generate lower forces and energies than the single-*trans* system. For the lipid-anchored Lac2, the comparison between the single-*trans* system and ten-percent system is difficult due to the rather

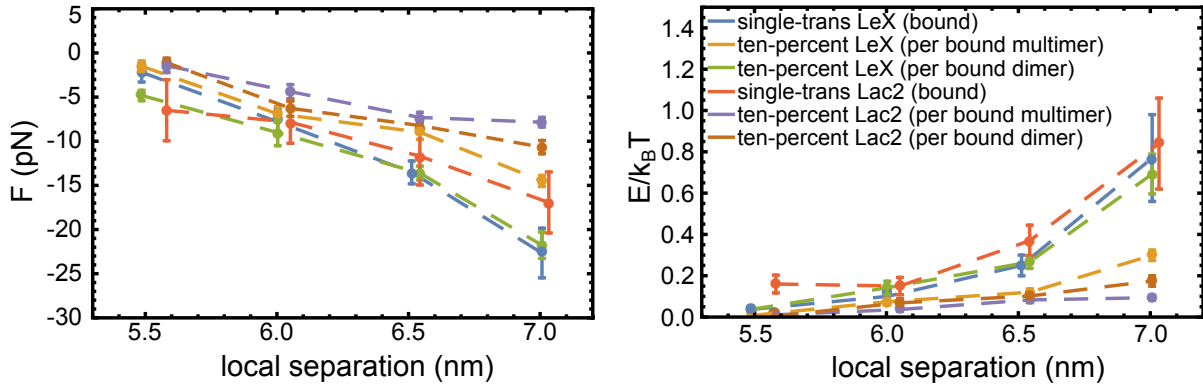


Figure 6.7: The forces (left) and the energies (right) for the bound states of the single-*trans* and ten-percent systems as a function of local separation. The values are adopted from Fig. 6.5 and Fig. 6.6

large errors obtained for the single-*trans* system. Our data suggests that, only at 5.5 nm and 7.0 nm local separations, lipid-anchored Lac2 in single-*trans* system generates larger forces than in the ten-percent system. For the other local separations, data points are not well resolved due to the rather large errors obtained from the single-*trans* system.

The pressure generated by the *trans*-binding of the lipid-anchored saccharides can be obtained by dividing the total force to the total surface area of the membranes. The pressure is particularly important as it can be directly obtained from the analysis of the neutron scattering data. As our ten-percent system, with the simultaneous *cis*- and *trans*-interactions, represents the experimental setups more realistically than the single-*trans* system, we discuss the pressure generated by the ten-percent system in detail. We calculate the pressure as the total force generated by the *trans*-engaged multimers per area. We obtain the average total force by simply multiplying the average force per bound multimer by the number of average multimers per trajectory frame (Fig. 6.6), which was already obtained before in Ch. 4.3. This procedure, after averaging over the trajectories, yields the average force generated by the *trans*-engaged multimers. The average pressure, then, can be calculated by dividing the average force by the area of the simulation box (in xy -plane). Fig. 6.8 shows how the pressure varies as a function of local separation. First, for all of the local separations, we obtain negative pressures which indicates that the overall interactions generated by the *trans*-binding of the lipid-anchored saccharides are attractive. That is, the opposing membranes are "pulled" to each other by the *trans*-binding. Second, we obtain a non-monotonic behavior for the pressure: for both of the lipid-anchored saccharides, the pressure has a minimum value at 6.0 nm local separation. The reason is, although the generated forces per bound multimer increase with the increasing local separation, the average number of *trans*-engaged multimers decrease as the increasing local separation makes the lipid-anchored saccharides less likely to engage in *trans*-interactions. Therefore, the total force contains two terms with opposite trends: the average force per bound multimer increases, but the

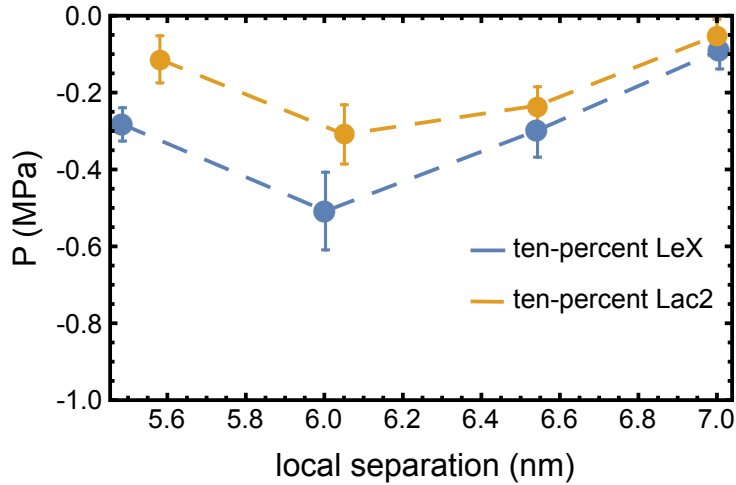


Figure 6.8: The pressure generated by the forces in *trans*-binding of the ten-percent system as a function of local separation. The pressure is calculated as the average total force per area. To calculate the total force we multiply the force per bound state by the average number of the bound states for a given local separation. The errors are calculated as the standard error of the mean of the pressure over ten independent trajectories.

number of *trans*-engaged multimers decreases with the increasing total separation. Our results show that, these two opposite trends yield the pressure to have its minimum at 6.0 nm local separation.

6.3 Summary

In this chapter, we present a simple harmonic model for the calculation of the forces and energies generated by the *trans*-binding of the lipid-anchored saccharides. Our model assumes that the lipid-anchored saccharides are embedded into the membranes *via* harmonic springs and that the forces generated by *trans*-binding of the lipid-anchored saccharides can be calculated by measuring the deviations of the harmonic springs from their equilibrium lengths. For the simulations with no *trans*-bound states, we show that the probability distribution of deviations in the position of the glycolipid linker with respect to the center of mass of the lipid head groups can be well approximated by a Gaussian distribution, consequently the forces and the energies can be calculated by using a harmonic model. Furthermore, we show that the magnitude of the deviations in the position of the glycolipid linker with respect to the center of mass of the lipid head groups, at all local separations except the ten-percent LeX system, lie within the range of our model. For the ten-percent LeX, we concluded that as the deviations beyond the range of our harmonic model have low probabilities, they do not affect our overall results.

For the single-*trans* system in which there is only one lipid-anchored saccharide in each membrane leaflet, we show that the average forces and energies generated by the *trans*-bound lipid-anchored saccharides increase with the increasing local separation. For

these systems, we calculate the maximum force to be 20 pN for the lipid-anchored LeX and 18 pN for the lipid-anchored Lac2. Our calculations yield maximum energies on the harmonic springs as $0.5 k_B T$.

When the *cis*- and *trans*-interactions are present, we show that the forces and energies generated by the *trans*-engaged multimers differ from the cases for the single-*trans* system without the *cis*-interactions. In order to distinguish between the generated forces by the *trans* engaged dimers and higher multimers, we treat them separately. For the both lipid-anchored LeX and Lac2, we observe that the forces and energies generated by the *trans*-engaged dimers and higher multimers increase with the increasing local separation. When we compare the results for the *trans*-engaged dimers and the higher multimers, we see that, in case of the lipid-anchored LeX, the *trans*-engaged dimers generate larger forces and energies than the higher multimers. One possible reason for that observations is the forces due to the *trans*-binding can be shared among the lipid-anchored saccharides in the higher multimers, resulting in overall lower forces. For the lipid-anchored Lac2, same results are obtained to a lesser extent. Among the lipid-anchored saccharides, the lipid-anchored LeX generates larger forces than the lipid-anchored Lac2. In comparison to the single-*trans* system, our results show that the *trans*-dimers of the lipid-anchored LeX, regardless of the existence of the *cis*-interactions generate similar forces. For the lipid-anchored Lac2, forces generated by the *trans*-dimers in the presence of *cis*-interactions are lower than the single-*trans* system at 5.5 nm and 7.0 nm local separations, however due to the rather large errors from the single-*trans* system, the comparisons at other local separations is difficult. As both *cis*- and *trans*- interactions are present in the experimental setups, it is reasonable to say that both lipid-anchored LeX and Lac2 will generate lower forces than the cases where there are no *cis*-interactions in the system.

In terms of the magnitude of the forces and energies, we get the largest forces to be around 20 pN for the lipid-anchored LeX and 15 pN for the lipid-anchored Lac2. These forces are well within the range of rupture forces of the lipid-anchored LeX observed in single-molecule force spectroscopy experiments described in the beginning of this chapter. The energy on the harmonic springs is in the order of $0.5 k_B T$ for the both systems.

Finally, we calculate the pressures generated by the forces in *trans*-binding. For both of the lipid-anchored saccharides, we obtain the minimum of the pressure curve at 6.0 nm local separation. The reason is that although the forces per bound state increases with the local separation, the average number of *trans*-bound states decreases. Therefore, these opposite trends in increasing forces and decreasing number of *trans*-bound states yield a minimum pressure at medium-range local separations. Our results imply that, it is the 6.0 nm local separation where the pressure is the minimum. Furthermore, we observe that the pressure is always negative for both of the lipid-anchored saccharides. This result suggests that the interactions caused by the *trans*-binding of the lipid-anchored saccharides is attractive, i.e. the overall effect of the *trans*-binding pulls the opposing

membranes to each other.

Overall, we present a simple harmonic model which can be utilized to calculate the forces and energies generated by the *trans*-binding of the lipid-anchored saccharides. Our results yield forces and energies well within the experimentally observed rupture forces of the lipid-anchored saccharides. To the best of our knowledge, this is the first study that comparatively analyzes the forces and the energies in *trans*-binding of the lipid-anchored LeX and Lac2.

Appendix A

Parametrization of MD Force Fields for Saccharides and Membranes

A.1 Parametrization of Amber Lipid14 Force Field for TIP5P Water Model

Amber Lipid 14 force field²⁸ has been developed using TIP3P water³⁴ as the solvent model. Amber Lipid 14 force field well reproduces L_o/L_d transition temperatures, area per lipid values, diffusion constants, bilayer thicknesses, and X-ray form factors. DMPC, DLPC, DOPC, POPC, LOPC are the available lipids in this force field with a PC head group.

Following the modifications to the original GLYCAM06h²⁹ force field of Sauter and Grafmueller,³⁶ we use TIP5P water model³⁰ throughout this work in order to capture carbohydrate-carbohydrate interactions accurately. As force fields heavily depend on the used water model, we need to validate the compatibility of Lipid 14 with TIP5P water.

In order to test the compatibility of Lipid14 with TIP5P water model, we run a set of simulations with identical initial structures, both in TIP3P and TIP5P, using the methods described at the end of this section. We calculate the area per lipid (APL) from the simulations, and observe a large decrease in APL for POPC in TIP5P at 303 K. This observation indicates that Lipid14 force field overestimates L_o/L_d transition temperature for POPC membranes in TIP5P (Fig. 2.3) and cannot be used with TIP5P. Therefore, we parametrize Lipid14 force field in order to attune with the TIP5P water model.

For the parametrization of the Lipid14 force field, we only use POPC lipids (Fig. A.1) and consider adjusting Lennard-Jones interactions between non-hydrogen PC head group atoms and TIP5P water. We apply a homogeneous scaling factor (using ParmEd⁹⁰) α_ϵ to the Lennard-Jones well depth ϵ , starting from 1.2 to 1.55, keeping equilibrium distances

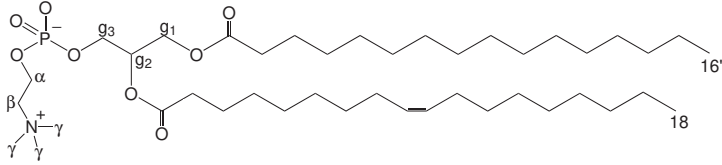


Figure A.1: Structure of the POPC lipid. Carbon atoms of particular interest in the order parameter calculations are labelled.

Atom Type Pairs	Scaling factor α_ϵ						
	Original	1.2	1.3	1.4	1.45	1.5	1.55
cC-OW	0.105830	0.1270	0.1376	0.1482	0.1535	0.1587	0.1640
oC-OW	0.149	0.1796	0.1946	0.2095	0.2170	0.2245	0.2320
oS-OW	0.1386	0.1663	0.1801	0.1940	0.2009	0.2078	0.2148
cA-OW	0.1323	0.1588	0.1720	0.1852	0.1918	0.1985	0.2051
oT-OW	0.1386	0.1663	0.1807	0.1940	0.2009	0.2078	0.2148
pA-OW	0.1789	0.2147	0.2326	0.2504	0.2594	0.2683	0.2773
nA-OW	0.1649	0.1979	0.2144	0.2309	0.2391	0.2474	0.2556
oP-OW	0.1497	0.1796	0.1946	0.2095	0.2170	0.2245	0.2320

Table A.1: First column is the atom type in PC head group, as used in Lipid14 force field. Original values from Lipid14 corresponds to the unmodified atom type-OW well-depth ϵ for TIP5P water model. Each column contains the scaling factor used and the obtained value for ϵ

σ_{ij} constant; our initial tests with $\alpha_\epsilon = 2.0$ yielded too high APL values therefore we restrain our search within $1.0 < \alpha_\epsilon < 2.0$. With this method, we are keeping lipid-lipid interactions intact, and only altering lipid-water interactions to account for the changes introduced by varying the water model.

Our aim with the parametrization is to reproduce the experimental observables like area per lipid, deuterium order parameters, and lateral diffusion constant of the POPC bilayer as described by original Lipid14 force field for TIP3P water model. Therefore, we use Lipid14 results as the target values for the parametrization, but provide experimental values for further comparison. Atom types considered in the parametrization as well as initial and scaled magnitude of $\epsilon_{i,j}$ are given in Table A.1.

We obtain the initial POPC membrane structure from CHARMM-GUI web interface⁹¹ with 64 lipids in each leaflet, and 50 water molecules per lipid (n_w). We minimize the structure initially for 100000 steps with steepest descent algorithm, and further for 100000 steps with conjugent gradient algorithm at constant volume. Next, we heat the entire system from 0 K to 200 K in 50000 steps at constant volume while applying harmonic constraint to the lipid positions with a $10 \text{ kcal mol}^{-1} \text{ \AA}^{-1}$ force constant. We proceed to the second heating process, from 200 K to 303 K in 100000 steps, with the same harmonic constraints, at constant 1 bar pressure with semi-isotropic pressure

coupling along xy dimensions. Heated structures are equilibrated for 100 ns at 303 K temperature and 1 bar pressure, with Langevin dynamics, Berendsen barostat,⁹² semi-isotropic pressure coupling, and zero surface tension. We perform production runs for 150 ns on ten independent trajectories, and save trajectories with 10 ps frequency. For all steps, we apply a 10 Å cutoff for the non-bonded interactions. In total, for every α_ϵ we obtain a 1.5 μ s trajectory.

For the simulations, we use GPU-accelerated Amber 16 MD engine.⁹³ We apply SHAKE^{35,94} algorithm in the heating, equilibration, and production stages to fix the distances of bonds involving hydrogen atoms.

In order to determine which α_ϵ reproduces the Lipid14 results, we first calculate the APL value for a given scaling factor by simply dividing the area of the box in xy -dimensions to the number of lipids per bilayer ($n_l = 64$). We observe a monotonic increase on APL values as a function of increasing α_ϵ (Fig. 2.5). This result is expected, as with increasing α_ϵ , water-head group interactions become stronger and the lipid bilayer transitions to the liquid disordered state. Around $\alpha_\epsilon = 1.4$, we reach the original TIP3P value, which itself approximates the experimentally observed APL.

We continue with calculating the electron density profiles of the lipid head and tail groups in the direction of the membrane normal. First, we align and center the trajectories such that center of mass of the PC head groups lie at the $z = 0$ plane, and by using 0.25Å resolution, we calculate the electron density of each unit. Results are shown in Fig. 2.6. In TIP5P model, head and tail group peaks are located further than in TIP3P, indicating that the bilayer is more structured in TIP5P with lipid tails assuming a nearly linear conformation. As the scaling factor α_ϵ increases, bilayer thickness (distance between PC head group peaks) decreases, and again around $\alpha_\epsilon = 1.4$, TIP3P results are reproduced.

Next, we calculate the order parameters for the lipid tails and head groups (Fig. A.2). Order parameters are given by $S_{CH} = \langle 3\cos^2\theta - 1 \rangle / 2$ where θ is the angle between C-H vector and the bilayer normal, and can be obtained very precisely from NMR experiments. The calculated order parameters are in good agreement with the TIP3P results. Significant change in the tail order parameters from $\alpha_\epsilon = 1.2$ to $\alpha_\epsilon = 1.4$ is an indication of the liquid ordered-liquid disordered phase transition. Although the match between experimental values (where available) and calculated S_{CH} values is not perfect, our results still match well with the original Lipid14 results. However, the agreement between original Lipid14 order parameters and experimental values is poor. This is a known issue with Lipid14 force field and discussed in more detailed elsewhere.³³ Our results suffer from the same problem as the original Lipid14, however fixing these problems would require a substantial reparametrization of the Lipid14 force field that goes beyond the scope of this work.

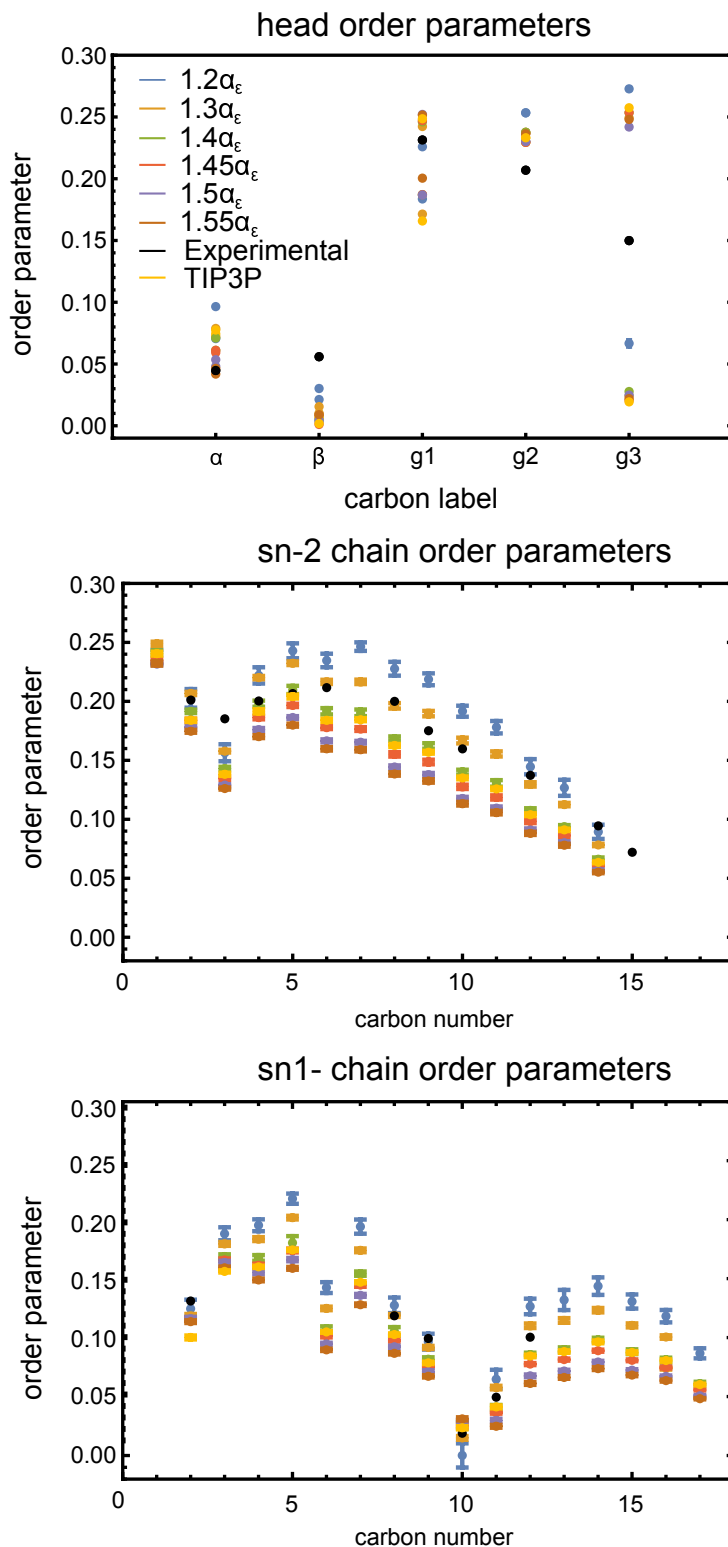


Figure A.2: Order parameters, from top the bottom, for PC head group, sn-1 & sn-2 tail chains. Trajectories are imaged beforehand to prevent unreasonable C-H bond distances due to periodic boundaries. Errors are calculated as the standard error of the mean from ten independent trajectories.

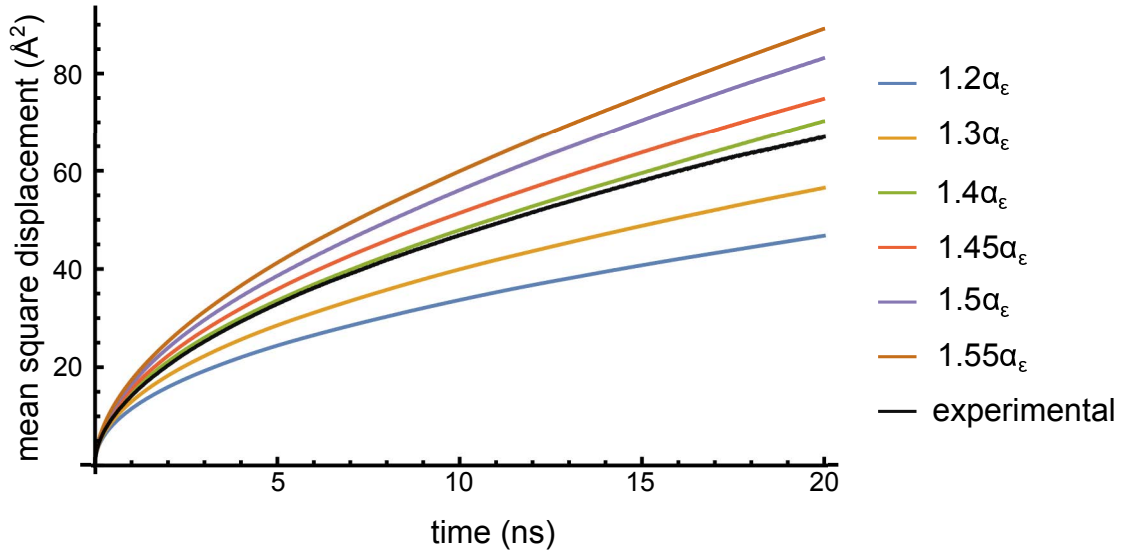


Figure A.3: Mean-squared-displacement (MSD) vs. time for different α_ϵ . MSD curves are calculated for and averaged over each lipid separately after removing the center of mass motion of the corresponding leaflets.

Overall, our parametrization yields structural parameters that overlap very well with the original Lipid14 force field.

The lateral diffusion constant is an important dynamical property and a measure of how far a given molecule translates in a given time interval. We calculate the diffusion constants for each α_ϵ by using mean-square displacement (MSD) and Einstein relation $2nD = \lim_{x \rightarrow \infty} \frac{MSD}{t}$. First, we separate the trajectories for upper and lower leaflet. To eliminate the caterpillar effect,⁹⁵ we subtract the center of mass motion of each leaflet. Then, we partition the trajectories into 20 ns fragments each of which have time origins separated by 20 ps. For each short trajectory, we calculate the MSD profiles separately for each lipid. We fit regions between 10 ns and 20 ns to a linear curve, and calculate the slope. Finally, by using Einstein relation we obtain the diffusion constants. MSD profiles for each α_ϵ , as well as for TIP3P, are given in Fig. A.3. At $\alpha_\epsilon = 1.4$, we reproduce the lateral diffusion constant in TIP3P. The discrepancies between calculated and experimental D_{xy} has been discussed in detail elsewhere,⁹⁶ but to summarize i) NPT ensemble, due to the temperature control is inadequate for reproducing correct experimental values, and ii) finite-size effects alter the D_{xy} . Overcoming these obstacles, one needs to perform production simulations in NVE ensemble, with large membrane patches. However, due to the time constraints on the project, we did not perform any further simulations.

Additionally, we calculate isothermal compressibility modulus, volume per lipid, and bilayer thickness for each α_ϵ (TableA.2). For $\alpha_\epsilon = 1.4$, we obtain the best match between calculated bilayer properties and original Lipid14 TIP3P values.

α_ϵ	APL (\AA^2)	VPL (\AA^3)	Luzatti Thickness (\AA)	K (mNm^{-1})	D_{xy} ($\text{\AA}^2/s$)
1.2	59.3 ± 0.2	1199 ± 1	38.2 ± 0.3	6442 ± 1744	3.51 ± 0.09
1.3	61.7 ± 0.1	1199 ± 1	36.7 ± 0.1	673 ± 35	4.41 ± 0.09
1.4	65.7 ± 0.1	1198 ± 1	35.1 ± 0.1	962 ± 292	5.81 ± 0.12
1.45	67.7 ± 0.1	1197 ± 1	34.3 ± 0.1	659 ± 29	6.18 ± 0.19
1.5	70.1 ± 0.1	1195 ± 1	33.6 ± 0.1	645 ± 31	7.12 ± 0.12
1.55	72.2 ± 0.1	1193 ± 1	33.1 ± 0.1	633 ± 18	7.66 ± 0.21
TIP3P	66.2 ± 0.1	1203 ± 1	35.4 ± 0.1	553 ± 53	5.82 ± 0.12
Exp.	64.3^{53}	1256^{56}	36.8^{56}	$180-330^{97}$	10.7^{98}

Table A.2: Calculated parameters for each α_ϵ . Errors are the standard error of the mean, calculated from ten independent trajectories. Experimental results are also given.

Overall, our results with $\alpha_\epsilon = 1.4$ yields to best overlap with the original Lipid14 force field. We can correctly reproduce the bilayer phase, APL value, bilayer thickness and diffusion constants for the pure POPC bilayer at 303 K using $\alpha_\epsilon = 1.4$. In this work, we use the $\alpha_\epsilon = 1.4$ for all membrane simulations.

A.2 Assigning Point Charges for the Glycolipid Linker

In MD simulations, partial atomic charges are used to calculate the electrostatic potential. For a non-polarizable force field, like Lipid14, these charges are fixed and do not change throughout the simulation.

In the glycolipids we used in this work, there is a glycerol moiety that connects the saccharide head group to the lipid tails. This moiety also exists in Lipid14, as a part of the head group residue. The only difference between them is that in Lipid14 glycerol moiety is connected to the highly charged phosphate atom of the zwitterionic PC head group, whereas in the glycolipids it is connected to the neutral saccharide unit. Therefore, in terms of the atomic charges of the same glycerol moiety, we would expect to have different point charges.

In our procedure for obtaining the partial charges for the glycolipid linker, we first generate the three-dimensional structure of the linker using Avogadro⁹⁹ (Fig. A.4). $-CH3$ methyl groups with the carbon numbers $C4$, $C7$, and $C8$ (and hydrogens attached to them) are known as the "capping" residues and are not part of the glycolipid linker. The reason for using these capping residues is that the glycolipid linker is attached to the saccharides (*via* the $O3$ atom) and to the lipid tails (*via* the $C6$ and $C5$ atoms), however including saccharides and lipid tails for the quantum mechanical charge derivation is computationally time consuming. Therefore, we replace saccharides and lipid tails with $-CH3$ methyl residues. Capping residues, as a result, function to mimic the saccharides and lipid tails.

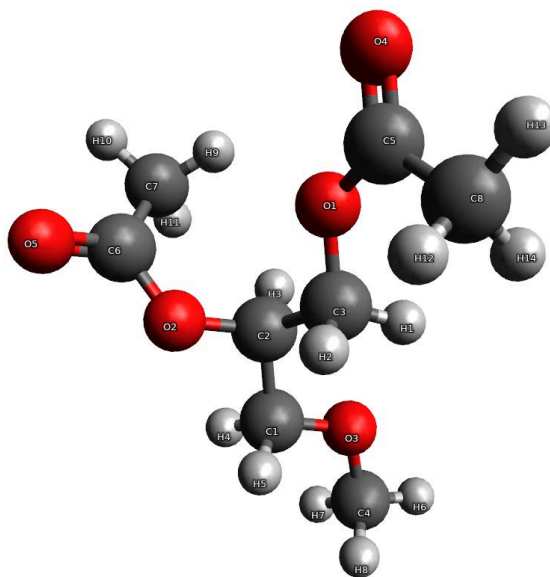


Figure A.4: Structure of the glycolipid linker generated by the Avogadro package.⁹⁹

In order to recalculate the partial charges, we apply restrained electrostatic potential (RESP) method, along with the established Amber protocol.⁵⁷ The idea behind RESP is to generate point charges on a given system that would mimic the overall quantum mechanical charge distribution.

After obtaining the structure of the glycolipid linker with the capping residues, we perform an initial geometry optimization with Universal Force Field (UFF)¹⁰⁰ using the steepest descent algorithm. Then, we apply two further geometry optimizations, first at MP2/6-31g, and second at HF/6-31g levels of theory using Gaussian03¹⁰¹ software. The same levels of theory are also used in Lipid14 and Glycam06 force fields to obtain the partial charges. Therefore, our choice of the basis sets allow our partial charges to be compatible both with Lipid14 and Glycam06. Up until this point, we do not assign any partial charges as the quantum mechanical calculations use to total electron density.

In order to obtain the partial charges, we use the optimized structures obtained from Gaussian03 software to calculate the electrostatic potential (ESP) surface using Antechamber package.¹⁰² Before we continue to generate the partial charges for the glycolipid linker, we first assign the partial charges for the capping residues using Lipid14 and Glycam06 force fields: in Lipid14 force field, hydrogens have $0.0528 e^-$ partial charge whereas in Glycam06 force field hydrogens have no partial charge. As the *C4* methyl residue mimic the saccharides, we assign hydrogens attached to *C4* (*H6*, *H7*, *H8*) zero partial charges. *C7* and *C8* methyl residues are to mimic lipid tails. Therefore we assign hydrogens bonded to *C7* and *C8* (*H9*, *H10*, *H11*, *H12*, *H13*, *H14*) $0.0528e^-$ partial charges. For the *C4* atom, we use $0.194 e^-$ partial charge as in the Glycam06 force field. For the *C7* and *C8* atoms, we use $-0.1584 e^-$ partial charge as in the Lipid14 force field.

Atom	Optimized	Lipid14	$ \Delta e_{optimized}^{-1} - e_{Lipid14}^{-1} $
O3	-0.3529	-0.4224	0.0695
O2	-0.4777	-0.4195	0.0582
O5	-0.5576	-0.5969	0.0393
O1	-0.4660	-0.4550	0.1100
O4	-0.5653	-0.5997	0.0344
C1	-0.0534	+0.015	0.0684
C2	-0.0498	+0.0914	0.1412
C3	+0.1193	+0.0159	0.1034
C5	+0.7890	+0.7836	0.0053
C6	+0.7793	+0.7704	0.0089

Table A.3: Original and recalculated partial charges (e^{-1}) for the glycolipid linker

With these assignments of the partial charges, we make sure that capping residues with *C7* and *C8* mimic the lipid tails, and capping residue with *C4* mimics the saccharides. This initial assignment of the partial charges to the capping residues can be considered as the constraints on the partial charges of the glycolipid linker. For the rest of the partial charge calculations, we keep the partial charges on the capping residues constant. Using these constraints, we obtain the initial set of RESP charges using Antechamber package. This initial set of RESP charges correspond to the one single structure of the glycolipid linker.

One complication we encounter here needs special attention: by design, the Antechamber package expects the residue to be connected to at most two units through head and tail atoms, just like in amino acid chains. However, in our case we have three connecting units. Therefore, for the RESP fitting we employ six iterations, in each of which we change the definitions of the head and tail atoms provided to the software. We then calculate the RESP charges as the arithmetic average of the obtained charges from each iteration.

For the second iteration of RESP fitting, we perform an MD simulation of the linker, using NPT ensemble, in TIP5P water, at 303 K temperature and 1 bar pressure for 1 μ s. The purpose of this step is to obtain a set of conformations of the glycolipid linker in water and recalculate the partial charges (using the initial set as the starting point) to capture the overall conformations of the glycolipid linker. We extract 100 random conformations from the simulation, and apply the same RESP fitting over *all* of the conformations. By this, we obtain a generalizable set of charges that is averaged over many different conformations. It is important to note that this averaging is not an arithmetic average: The Antechamber software generates an overall charge distribution using 100 conformations, and then calculates the partial charges that corresponds to this overall charge distribution. Table A.3 shows the optimized partial charges for the

glycolipid linker, and the original charges from the Lipid14 force field. The original charges from the Lipid14 force field correspond to the partial charges that we would have used if we did not perform a charge optimization.

An error estimate for the charges can be performed by increasing the number of conformations from 100 and checking the convergence of the individual charges. However, due to the time constraints and the computational costs the error estimation is beyond the scope of this thesis.

For the bonded parameters, we adopt a hybrid approach where the parameters for the lipid ends are obtained from Lipid14 force field, and for the carbohydrate end from Glycam06 force field. The following page contains the Amber compatible *frcmod* and *prep* files that show the atom types, partial charges, and the bonded parameters for the glycolipid linker.

frmod (force field) file for the glycolipid linker. Following file is compatible to use with AMBER. It contains the atom types, bond, angle, and dihedral parameters that are used for constructing the glycolipid linker. This file contains bonded parameters for the glycolipid linker that are not available in AMBER Lipid14 and Glycam06h force fields.

```

frmod file for glycolipid linker
MASS
Os 16.000      0.434      same as o
Cg 12.010      0.878      same as c3
H1 1.008       0.135      same as h1
cC 12.010      0.360      same as cc
oC 16.000      0.434
BOND
Cg-Os 316.70   1.423      same as c3-oh, penalty score= 3.8
Cg-H1 330.60   1.097      same as c3-h1, penalty score= 0.0
Cg-Cg 300.90   1.538      same as c3-c3, penalty score= 0.0
cC-Os 405.90   1.347      same as cc-oh, penalty score= 3.8
cC-oC 622.90   1.225      same as c2- o, penalty score= 4.9
Cg-Os 316.70   1.423      same as c3-oh, penalty score= 3.8
cC-cD 328.3    1.5080     Lipid14 v2.0 (GAFF c -c3)
ANGLE
H1-Cg-Os 50.930  110.260    same as h1-c3-oh, penalty score= 2.0
Cg-Cg-Os 67.470  110.190    same as c3-c3-oh, penalty score= 2.0
Cg-Cg-H1 46.390  109.560    same as c3-c3-h1, penalty score= 0.0
Cg-Cg-Cg 62.860  111.510    same as c3-c3-c3, penalty score= 0.0
H1-Cg-H1 39.240  108.460    same as h1-c3-h1, penalty score= 0.0
cC-Os-Cg 0.000   0.000      ATTN, need revision
Os-cC-oC 74.687  123.410    Calculated using oh-ca- o, penalty score= 25.5
Cg-Os-Cg 50.00   111.60     Copy of Cg-Os-Cg from GLYCAM06
Os-Cg-Os 100.00  112.00     Dimethoxymethane, 1,1 Dimethoxyethane
Os-Cg-Cg 70.00   108.50     Copy of Os-Cg-Cg from GLYCAM06
cC-cD-cD 63.790  110.530    Lipid14 v2.0 (GAFF c -c3-c3)
cC-cD-hL 47.200   109.680    Lipid14 v2.0 (GAFF c -c3-hc)
Os-Cg-Cg 70.00   108.50     Copy of Os-Cg-Cg from GLYCAM06
cD-cC-Os 69.260  111.960    Lipid14 v2.0 (GAFF c3-c -os)
cD-cC-oC 68.030  123.110    Lipid14 v2.0 (GAFF c3-c -o )
DIHE
Os-Cg-Cg-OS 9  1.400  0.000  3.000  same as X -c3-c3-X , penalty score= 0.0
H1-Cg-Cg-Os 9  1.400  0.000  3.000  same as X -c3-c3-X , penalty score= 0.0
Cg-Cg-Cg-Os 9  1.400  0.000  3.000  same as X -c3-c3-X , penalty score= 0.0
Cg-Cg-Os-cC 3  0.500  0.000  3.000  same as X -c3-oh-X , penalty score=173.0
Cg-Cg-Cg-H1 9  1.400  0.000  3.000  same as X -c3-c3-X , penalty score= 0.0
H1-Cg-Cg-H1 9  1.400  0.000  3.000  same as X -c3-c3-X , penalty score= 0.0
oC-cC-Os-Cg 2  2.100  180.000  2.000  same as X -c2-oh-X , penalty score=405.0
H1-Cg-Os-cC 3  0.500  0.000  3.000  same as X -c3-oh-X , penalty score=173.0
Cg-Os-Cg-Cg 1  0.16  0.0  3.000  SCEE=1.0 SCNB=1.0 Ethyl methyl ether, Isopropyl methyl ether for OLS,OLT
H1-Cg-Os-Cg 1  0.27  0.0  3.000  SCEE=1.0 SCNB=1.0 Protein Linkage: Methoxymethane, Isobutyl methyl ether
Cg-Os-Cg-Cg 1  0.16  0.0  3.000  SCEE=1.0 SCNB=1.0 Ethyl methyl ether, Isopropyl methyl ether for OLS,OLT
cD-cD-cC-Os 1  -0.1226  180.000  -1.000  SCEE=1.2 SCNB=2.0 Lipid14 v2.10 (paramfit)
cD-cD-cC-Os 1  -0.2054  180.000  -2.000  SCEE=1.2 SCNB=2.0 Lipid14 v2.10 (paramfit)
cD-cD-cC-Os 1  0.1802  0.000  -3.000  SCEE=1.2 SCNB=2.0 Lipid14 v2.10 (paramfit)
cD-cD-cC-Os 1  0.5107  0.000  -4.000  SCEE=1.2 SCNB=2.0 Lipid14 v2.10 (paramfit)
cD-cD-cC-Os 1  0.1355  0.000  5.000  SCEE=1.2 SCNB=2.0 Lipid14 v2.10 (paramfit)
hL-cD-cC-Os 1  0.000  180.0  2.000  SCEE=1.2 SCNB=2.0 Lipid14 v2.0 (GAFF X -c -c3-X )
Cg-Os-cC-cD 1  2.700  180.000  2.000  SCEE=1.2 SCNB=2.0 Lipid11 v1.0 (GAFF X -os-c -X )
IMPROPER
NONBON
Os 1.6612  0.2100  same as o
Cg 1.9080  0.1094  same as c3
H1 1.3870  0.0157  same as h1
cC 1.9080  0.0860  same as cc

```

prep (library) file for the glycolipid linker. Following file is compatible to use with AMBER. It contains the atom types, atom names, charges, masses, and the connectivity of the atoms in the glycolipid linker.

```
0 0 2
prep file for glycolipid linker
linker.res
LNK INT 0
CORRECT OMIT DU BEG
0.0000
 1 DUMM DU M 0 -1 -2 0.000 .0 .0 .00000
 2 DUMM DU M 1 0 -1 1.449 .0 .0 .00000
 3 DUMM DU M 2 1 0 1.523 111.21 .0 .00000
 4 O1 Os M 3 2 1 1.540 111.208 -180.000 -0.352904
 5 C1 Cg M 4 3 2 1.509 133.936 -110.920 -0.053350
 6 H4 H1 E 5 4 3 1.098 111.702 -26.775 0.109381
 7 H5 H1 E 5 4 3 1.097 107.602 95.244 0.109381
 8 C3 Cg M 5 4 3 1.590 112.794 -146.762 0.049795
 9 O4 Os S 8 5 4 1.430 109.474 77.258 -0.477720
10 C7 cC S 9 8 5 1.401 125.364 72.314 0.779349
11 O5 oC E 10 9 8 1.222 127.575 -14.191 -0.557600
12 H14 H1 E 8 5 4 1.097 101.934 -37.422 0.152475
13 C4 Cg M 8 5 4 1.588 119.910 -151.550 0.119341
14 H9 H1 E 13 8 5 1.096 118.781 48.226 0.085075
15 H10 H1 E 13 8 5 1.098 109.455 -70.732 0.085075
16 O2 Os M 13 8 5 1.430 102.868 168.598 -0.465964
17 C5 cC M 16 13 8 1.351 118.762 176.427 0.788975
18 O3 oC E 17 16 13 1.202 125.844 4.113 -0.565310
LOOP
IMPROPER
 05 O4 C7 +M
 03 O2 C5 +M
DONE
STOP
```

Appendix B

Simulations of saccharides and membranes

B.1 Simulations of saccharides in water

We obtain the initial saccharide structures from Glycam Carbohydrate Builder⁵² (Fig. 2.1). We translate one of the saccharide monomers by 12 Å in all dimensions, and solvate the entire system with 14 Å cushion of TIP5P water (Table B.1). We minimize the initial structure for 5000 steps with steepest descent, and an additional 5000 steps with conjugent gradient algorithm. We heat the entire system from 0 K to 303 K in 50000 steps at constant volume, and use Langevin thermostat to control the temperature. After heating, we equilibriate the system for 2 ns using *sander*,⁹³ before switching to Amber GPU engine. For the production runs, we simulate each trajectory for 2 μ s, with 2 fs timesteps, 10 Å non-bonded cutoff, using Monte-Carlo barostat¹⁰³ and Langevin thermostat, at 303 K temperature and 1 bar pressure, employing SHAKE algorithm to restrain the length of hydrogen containing bonds. We simulate 50 independent trajectories for LeX, 40 for Lac2, and 20 for Lac1. With this procedure, we obtain in total 100 μ s trajectory for LeX, 40 μ s for Lac2, and 40 μ s Lac1 (Table. B.1).

	Simulation Time	n_W
LeX	50x2 μ s	4287
Lac1	20x2 μ s	6007
Lac2	40x2 μ s	8504

Table B.1: Total simulation time and number of water molecules for saccharide simulations in water

B.2 Simulations of lipid-anchored saccharides

B.2.1 Simulations of lipid-anchored saccharides in planar membranes

This section contains the details of the simulations of lipid anchored saccharides in planar membranes.

B.2.1.1 Simulations of single-*trans* system

We obtain the initial membrane structures from CHARMM-GUI. For all saccharides (Fig. 2.9), we consider a membrane patch composed of 72 POPC lipids. We replace one lipid molecule in each of the leaflets with the lipid-anchored saccharide, and adjust the local separation according to the Eq.(2.1). We vary the local separation from 5.5 nm to 8.0 nm for LeX and 5.5 nm to 7.5 nm for Lac2 with 0.5 nm increments (Table B.2). Two snapshots from the simulations of LeX at 5.5 nm and 7.5 nm separations are given in Fig. 2.11.

We perform a two-step minimization: first we minimize the solvent by fixing the solute molecules with harmonic constraints with a force constant 500 kcal mol⁻¹ Å⁻¹, for 2500 steps with steepest descent and 2500 steps with the conjugate gradient algorithm. Then, we remove the constraints on the solute, and perform the same minimization again. We apply a three-step heating for the entire system: first, we heat the system from 0 K to 100 K at constant volume, while holding the lipids and lipid anchored saccharides with harmonic constraints with a force constant 20 kcal mol⁻¹ Å⁻¹. In the second step, we heat the system from 100 K to 200 K in 10000 steps at constant volume, but this time we relax the harmonic constraints to a force constant of 10 kcal mol⁻¹ Å⁻¹. For the third heating step, we heat the system from 200 K to 303 K in 10000 steps, at constant pressure, using semi-isotropic pressure coupling and zero surface tension, using Langevin thermostat and Berendsen barostat with the same harmonic constraints of the second step. We use $\tau = 3$ ps for the pressure relaxation time and 5.0 ps⁻¹ for the collision frequency.

	5.5 nm	6.0 nm	6.5 nm	7.0 nm	7.5 nm	8.0 nm
n_w (LeX)	1264	1722	2107	2493	2878	3263
n_w (Lac2)	1373	1753	2132	2512	2891	N.A.

Table B.2: Number of water molecules (n_w) for each local separation in single-trans simulations.

Each system is equilibrated for 100 ns at 303 K and 1 bar. For the production runs, we consider ten independent trajectories. Each trajectory is simulated at 303 K and 1 bar, with 5.0 ps^{-1} collision frequency, $\tau=3 \text{ ps}$ pressure relaxation time, using Berendsen barostat, Langevin thermostat and semi-isotropic pressure coupling for $1 \mu\text{s}$. For all steps we employ SHAKE algorithm to restrain the lengths of the bonds involving hydrogen atoms, and use 2 fs. time step in the integrator. We obtain $10 \mu\text{s}$ trajectory for LeX and Lac2.

B.2.1.2 Simulations of single-*cis* system

We obtain the initial membrane structure from CHARMM-GUI web interface with 64 POPC lipids in each leaflet. Then, we replace two POPC lipids in one leaflet with two lipid anchored saccharides.

As there are no *trans*-interactions, we choose a single local separation of 8.0 nm.

We perform the minimization, heating and equilibration in the same way as described in Ch.B.2.1. For the production runs, we simulate the systems for $2 \mu\text{s}$ using 25 independent initial structures for LeX and Lac2. In the end, we obtain $50 \mu\text{s}$ data for two lipid-anchored saccharides in *cis*-configuration

B.2.1.3 Simulations of ten-percent system

Systems we describe in Ch.B.2.1-B.2.1.2 are isolated examples of single *trans*- and *cis*-interactions, and do not include more complicated cases where lipid anchored saccharides can interact both in the same and between different leaflets. The overall effect of such interactions cannot be explained by just considering single *trans*- and *cis*-interactions. In order to account for both *cis*- and *trans*- interactions simultaneously, we construct a single POPC bilayer with 10% of the lipids at each leaflet are replaced by lipid anchored saccharides. In order to reduce the membrane undulations to the minimal level, we consider 100 lipids per leaflet.

We vary the thickness of the water layer by Eq. 2.1, and adjust the local separation between periodic images from 5.5 nm to 8.0 nm for LeX and from 5.5 nm to 7.5 nm for Lac2, all with 0.5 nm increments.

	5.5 nm	6.0 nm	6.5 nm	7.0 nm	7.5 nm	8.0 nm
n_w (LeX)	3247	4298	5348	6398	7449	8499
n_w (Lac2)	3247	4274	5302	6330	7357	N.A.

Table B.3: Number of water molecules (n_w) for each local separation in ten-percent simulations

We perform the minimization, heating, and equilibration in the same way as described in Ch. B.2.1. For the production runs, we simulate each system by 1 μ s with using ten independent initial structures. With that, we obtain in total 10 μ s trajectory for each separation, and for each lipid anchored saccharide.

B.2.2 Simulations of lipid-anchored saccharides in apposing fluctuating membranes

In all the systems we describe in Ch. B.2.1- B.2.1.3, we employed a self-interacting single bilayer system that fixes the local separation between the membrane and its periodic images. Due to the self-interacting nature of the system, the local separation is equal to the average separation and membrane fluctuations do not change these quantities. On the other hand, as discussed in Chapter 1, membrane fluctuations have an important role in the binding of lipid-anchored saccharides. In this section, we describe our simulation setup that allows membrane fluctuations to change the local separation between the membranes.

In order to include membrane fluctuations, we consider two lipid bilayers, doped with 10% glycolipids. Such a system involves two membranes that can fluctuate during the simulations. We construct the two bilayer system by first building a single bilayer with 100 POPC lipids in each leaflet. We replace ten lipids by lipid anchored LeX and replicate this system nine times to obtain a single bilayer that contains 810 POPC lipids and 90 lipid anchored LeX in each leaflet. Then we duplicate this single bilayer, and translate it by 7.7 nm in z -direction to generate the second bilayer. We adjust the water thickness such that *average* mid-plane separation is 7.7 nm, as this is the experimentally observed preferred separation.²⁵ A snapshot from the simulation is given in Fig. 2.13.

We minimize and heat the system as described in Ch. B.2.1. Only difference is that, in order to increase the computational efficiency, we employ hydrogen mass repartitioning method (HMR)¹⁰⁴ and use 3 fs time step in the simulations. For production runs, we consider ten independent trajectories, each of which are \approx 1000 ns long. We discard first 150 ns of the trajectories as the equilibration step.

Appendix C

The correlation length and time of the apposing fluctuating bilayer simulations

To check if our simulated systems of apposing fluctuating membranes (Ch. 5) are large enough to yield uncorrelated fluctuations for the local separations, we calculate the correlation function between the local separation fluctuations (height) as a function of distance. The spatial correlation function for the local separation fluctuations, assuming isotropy of the membrane system, can be calculated via

$$\rho_{spatial}(\Delta x) = \langle (x)(x + \Delta x) \rangle - \langle x \rangle^2 \quad (\text{C.1})$$

where $l(x)$ and $l(x + \Delta x)$ are the local separations at the positions x and $x + \Delta x$ for a given time point. For a large enough system size, the spatial correlation function should converge to zero at large enough Δx values; that is for large enough system the local separation fluctuations at distant parts of the membrane must be uncorrelated from each other. In order to calculate the spatial correlation function, we discretize the the membrane surface by applying a 16×16 grid and obtain 256 data points for each trajectory frame. This choice of grid size results in grid size of $\approx 1.5 \times 1.5 \text{ nm}^2$. For every grid cell, we calculate the local separation as the distance between the mid-planes of the apposing membrane leaflets. For a given grid cell with the indices i, j , we calculate the product $l_{i,j}(x)l_{i+n,j}(x)$ and $l_{i,j}l_{i,j+n}(x)$ where n is the discrete increment, ranging from 0 to 16. In our particular square grid, i, j can have values in between 1 to 16. We repeat this calculation for all possible i, j points, first average over the spatial coordinates and then over the entire trajectory, to obtain the spatial correlation function $\rho_{spatial}(n)$ for a given discrete increment n . Finally, we vary the n from 0 to 16 and applying the periodic boundary conditions (if $i + n > n_{max}$, then $i + n = i + n - n_{max}$ where n_{max} is the largest grid cell index 16) to calculate the spatial correlation function over all possible

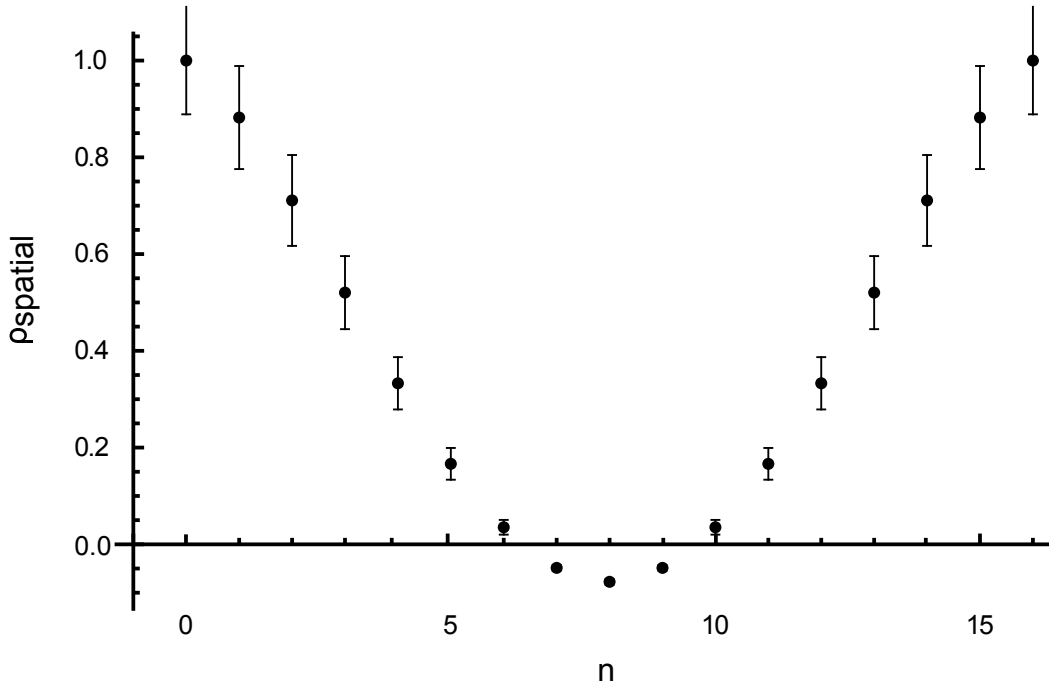


Figure C.1: The spatial-correlation function $\rho_{spatial}$ for the local separation as a function of discrete increment n . Every n -value is separated by 1.5 nm. The errors are calculated as the standard error of the mean over ten independent trajectories.

discrete n values. Fig. C.1 shows the spatial correlation function $\rho_{spatial}$ averaged over ten independent trajectories as a function of n . We normalize $\rho_{spatial}$ such that the correlation value at $\Delta x = 0$ (the auto-correlation) is 1. We observe that the spatial correlation function decreases with increasing n . At $n = 8$, the spatial correlation function has a minimum and increases for higher n values. The reason for this behavior is that as the system is periodic, the largest correlation length is $n_{max}/2$. Therefore, the correlations at the point n and $n + n_{max}$ are the same. Since we have 16 grid cells in each x - and y -directions, the correlation function is symmetric around $n = 16/2 = 8$. We observe that the correlation function reduces to zero at $n = 6$, and assumes negative values beyond that point. This observation verifies that the size of our apposing fluctuating membrane system is large enough such that the spatial correlations between the local separation are uncorrelated. For a larger system, we would expect the spatial correlation function to fluctuate around zero.

The correlations between the local separation can also be calculated in time. The time-correlation function for the local separation fluctuations is given as

$$\rho_{time}(\Delta t) = \langle (t)(t + \Delta t) \rangle - \langle t \rangle^2 \quad (C.2)$$

for a given time points t and $t + \Delta t$. The time correlation function indicates if the simulated trajectories are long enough "forget" the initial configuration. We calculate the time-correlation function for the local separation similar to the calculation of spatial

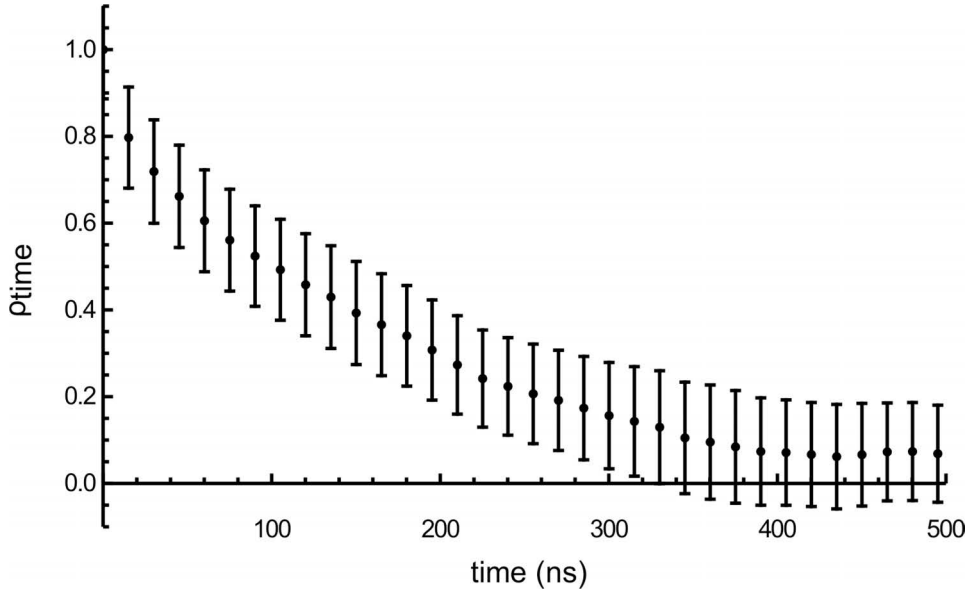


Figure C.2: The time-correlation function ρ_{time} for the local separation as a function of simulation time t . As the trajectories have different lengths, we calculate the correlations up to 500 ns. The errors are calculated as the standard error of the mean for every time point over ten independent trajectories.

correlation function. The only difference is that, in time-correlation we are looking for the correlations in time. Therefore, we calculate the correlations between a given grid cell at a given time point t and at the other time points $t + \Delta t$ for the same grid cell. Then, we average the time-correlation function over all grid cells and all possible time points for a given Δt . Finally, we average the time-correlation function over ten independent trajectories. As we have trajectories with different lengths, we average the time-correlation function up to the time point t for the shortest trajectory. Fig. C.2 shows the averaged time-correlation function ρ_{time} as a function of time. We normalize ρ_{time} such that the correlations at time $t = 0$ is 1. From Fig. C.2 we observe that the time-correlation function decreases with increasing time and reaches to zero \approx after 400 ns. After 400 ns, the time-correlation function fluctuates around zero within the error estimates. This observation indicates that the fluctuations in the local separation for a given grid cell "forget" their initial values \approx after 400 ns. As all the trajectories are longer than 400 ns, we can conclude that our trajectories are long enough for local separation fluctuations for a given grid cell to become uncorrelated.

Bibliography

- [1] Ü. Coskun and K. Simons, “Cell membranes: the lipid perspective,” Structure, vol. 19, no. 11, pp. 1543–1548, 2011.
- [2] G. Van Meer, D. R. Voelker, and G. W. Feigenson, “Membrane lipids: where they are and how they behave,” Nature reviews Molecular cell biology, vol. 9, no. 2, p. 112, 2008.
- [3] M. Edidin, “Lipids on the frontier: a century of cell-membrane bilayers,” Nature Reviews Molecular Cell Biology, vol. 4, no. 5, p. 414, 2003.
- [4] M. E. Taylor and K. Drickamer, Introduction to glycobiology. Oxford university press, 2011.
- [5] J. Costerton, R. Irvin, and K. Cheng, “The bacterial glycocalyx in nature and disease,” Annual Reviews in Microbiology, vol. 35, no. 1, pp. 299–324, 1981.
- [6] S. Weinbaum, J. M. Tarbell, and E. R. Damiano, “The structure and function of the endothelial glycocalyx layer,” Annu. Rev. Biomed. Eng., vol. 9, pp. 121–167, 2007.
- [7] U. Rutishauser and L. Sachs, “Cell-to-cell binding induced by different lectins.,” The Journal of cell biology, vol. 65, no. 2, pp. 247–257, 1975.
- [8] R. L. Schnaar, “Glycolipid-mediated cell–cell recognition in inflammation and nerve regeneration,” Archives of biochemistry and biophysics, vol. 426, no. 2, pp. 163–172, 2004.
- [9] C. L. Nilsson, Lectins: proteins that interpret the sugar code. ACS Publications, 2003.
- [10] I. Eggens, B. Fenderson, T. Toyokuni, B. Dean, M. Stroud, and S.-I. Hakomori, “Specific interaction between lex and lex determinants. a possible basis for cell recognition in preimplantation embryos and in embryonal carcinoma cells.,” Journal of Biological Chemistry, vol. 264, no. 16, pp. 9476–9484, 1989.

- [11] N. Kojima and S.-i. Hakomori, "Cell adhesion, spreading, and motility of gm3-expressing cells based on glycolipid-glycolipid interaction.," Journal of Biological Chemistry, vol. 266, no. 26, pp. 17552–17558, 1991.
- [12] I. Bucior, S. Scheuring, A. Engel, and M. M. Burger, "Carbohydrate-carbohydrate interaction provides adhesion force and specificity for cellular recognition," J Cell Biol, vol. 165, no. 4, pp. 529–537, 2004.
- [13] M. R. Wormald, C. J. Edge, and R. A. Dwek, "The solution conformation of the le x group," Biochemical and biophysical research communications, vol. 180, no. 3, pp. 1214–1221, 1991.
- [14] S. Pérez, N. Mouhous-Riou, N. E. Nifant'ev, Y. E. Tsvetkov, B. Bachet, and A. Imberty, "Crystal and molecular structure of a histo-blood group antigen involved in cell adhesion: the lewis x trisaccharide," Glycobiology, vol. 6, no. 5, pp. 537–542, 1996.
- [15] S.-i. Hakomori, "Tumor malignancy defined by aberrant glycosylation and sphingo (glyco) lipid metabolism," Cancer research, vol. 56, no. 23, pp. 5309–5318, 1996.
- [16] H. Gooi, T. Feizi, A. Kapadia, B. Knowles, D. Solter, and M. Evans, "Stage-specific embryonic antigen involves α ? 3 fucosylated type 2 blood group chains," Nature, vol. 292, no. 5819, p. 156, 1981.
- [17] N. Kojima, B. A. Fenderson, M. R. Stroud, R. I. Goldberg, R. Habermann, T. Toyokuni, and S.-I. Hakomori, "Further studies on cell adhesion based on le x-le x interaction, with new approaches: Embryoglycan aggregation of f9 teratocarcinoma cells, and adhesion of various tumour cells based on le x expression," Glycoconjugate journal, vol. 11, no. 3, pp. 238–248, 1994.
- [18] G. I. Csonka, C. P. Sosa, and I. G. Csizmadia, "Ab initio study of lowest-energy conformers of lewis x (lex) trisaccharide," The Journal of Physical Chemistry A, vol. 104, no. 15, pp. 3381–3390, 2000.
- [19] C. Gourmala, Y. Luo, F. Barbault, Y. Zhang, S. Ghalem, F. Maurel, and B. Fan, "Elucidation of the lewisx-lewisx carbohydrate interaction with molecular dynamics simulations: A glycosynapse model," Journal of Molecular Structure: THEOCHEM, vol. 821, no. 1, pp. 22–29, 2007.
- [20] R. Zucca, M. Boero, C. Massobrio, C. Molteni, and F. Cleri, "Interacting lewis-x carbohydrates in condensed phase: A first-principles molecular dynamics study," The Journal of Physical Chemistry B, vol. 115, no. 43, pp. 12599–12606, 2011.

-
- [21] C. Tromas, J. Rojo, J. M. de la Fuente, A. G. Barrientos, R. García, and S. Penadés, “Adhesion forces between lewisx determinant antigens as measured by atomic force microscopy,” Angewandte Chemie International Edition, vol. 40, no. 16, pp. 3052–3055, 2001.
- [22] J. M. de la Fuente, P. Eaton, A. G. Barrientos, M. Menéndez, and S. Penadés, “Thermodynamic evidence for ca^{2+} -mediated self-aggregation of lewis x gold glyconanoparticles. a model for cell adhesion via carbohydrate- carbohydrate interaction,” Journal of the American Chemical Society, vol. 127, no. 17, pp. 6192–6197, 2005.
- [23] F. Pincet, T. Le Bouar, Y. Zhang, J. Esnault, J.-M. Mallet, E. Perez, and P. Sinay, “Ultraweak sugar-sugar interactions for transient cell adhesion,” Biophysical journal, vol. 80, no. 3, pp. 1354–1358, 2001.
- [24] C. Gourier, F. Pincet, E. Perez, Y. Zhang, J.-M. Mallet, and P. Sinaÿ, “Specific and non specific interactions involving le x determinant quantified by lipid vesicle micromanipulation,” Glycoconjugate journal, vol. 21, no. 3-4, pp. 165–174, 2004.
- [25] E. Schneck, B. Demé, C. Gege, and M. Tanaka, “Membrane adhesion via homophilic saccharide-saccharide interactions investigated by neutron scattering,” Biophysical journal, vol. 100, no. 9, pp. 2151–2159, 2011.
- [26] E. Schneck, F. Rehfeldt, R. G. Oliveira, C. Gege, B. Demé, and M. Tanaka, “Modulation of intermembrane interaction and bending rigidity of biomembrane models via carbohydrates investigated by specular and off-specular neutron scattering,” Physical Review E, vol. 78, no. 6, p. 061924, 2008.
- [27] M. F. Schneider, R. Zantl, C. Gege, R. R. Schmidt, M. Rappolt, and M. Tanaka, “Hydrophilic/hydrophobic balance determines morphology of glycolipids with oligolactose headgroups,” Biophysical journal, vol. 84, no. 1, pp. 306–313, 2003.
- [28] C. J. Dickson, B. D. Madej, Å. A. Skjervik, R. M. Betz, K. Teigen, I. R. Gould, and R. C. Walker, “Lipid14: the amber lipid force field,” Journal of chemical theory and computation, vol. 10, no. 2, pp. 865–879, 2014.
- [29] K. N. Kirschner, A. B. Yongye, S. M. Tschampel, J. González-Outeiriño, C. R. Daniels, B. L. Foley, and R. J. Woods, “Glycam06: a generalizable biomolecular force field. carbohydrates,” Journal of computational chemistry, vol. 29, no. 4, pp. 622–655, 2008.
- [30] M. W. Mahoney and W. L. Jorgensen, “A five-site model for liquid water and the reproduction of the density anomaly by rigid, nonpolarizable potential functions,” The Journal of Chemical Physics, vol. 112, no. 20, pp. 8910–8922, 2000.

- [31] A. Catte, M. Girysh, M. Javanainen, C. Loison, J. Melcr, M. S. Miettinen, L. Monticelli, J. Määttä, V. S. Oganessian, O. S. Ollila, *et al.*, “Molecular electrometer and binding of cations to phospholipid bilayers,” Physical Chemistry Chemical Physics, vol. 18, no. 47, pp. 32560–32569, 2016.
- [32] O. S. Ollila and G. Pabst, “Atomistic resolution structure and dynamics of lipid bilayers in simulations and experiments,” Biochimica et Biophysica Acta (BBA)-Biomembranes, vol. 1858, no. 10, pp. 2512–2528, 2016.
- [33] A. Botan, F. Favela-Rosales, P. F. Fuchs, M. Javanainen, M. Kandukuri, W. Kulig, A. Lamberg, C. Loison, A. Lyubartsev, M. S. Miettinen, *et al.*, “Toward atomistic resolution structure of phosphatidylcholine headgroup and glycerol backbone at different ambient conditions,” The Journal of Physical Chemistry B, vol. 119, no. 49, pp. 15075–15088, 2015.
- [34] W. L. Jorgensen, J. Chandrasekhar, J. D. Madura, R. W. Impey, and M. L. Klein, “Comparison of simple potential functions for simulating liquid water,” The Journal of chemical physics, vol. 79, no. 2, pp. 926–935, 1983.
- [35] S. Miyamoto and P. A. Kollman, “Settle: An analytical version of the shake and rattle algorithm for rigid water models,” Journal of computational chemistry, vol. 13, no. 8, pp. 952–962, 1992.
- [36] J. Sauter and A. Grafmueller, “Solution properties of hemicellulose polysaccharides with four common carbohydrate force fields,” Journal of Chemical Theory and Computation, vol. 11, no. 4, pp. 1765–1774, 2015.
- [37] J. Sauter and A. Grafmueller, “Predicting the chemical potential and osmotic pressure of polysaccharide solutions by molecular simulations,” Journal of chemical theory and computation, vol. 12, no. 9, pp. 4375–4384, 2016.
- [38] J. Hu, R. Lipowsky, and T. R. Weikl, “Binding constants of membrane-anchored receptors and ligands depend strongly on the nanoscale roughness of membranes,” Proceedings of the National Academy of Sciences, vol. 110, no. 38, pp. 15283–15288, 2013.
- [39] P. Schuck, “Use of surface plasmon resonance to probe the equilibrium and dynamic aspects of interactions between biological macromolecules,” Annual review of biophysics and biomolecular structure, vol. 26, no. 1, pp. 541–566, 1997.
- [40] S. Meier and S. R. Beeren, “Simultaneous determination of binding constants for multiple carbohydrate hosts in complex mixtures,” Journal of the American Chemical Society, vol. 136, no. 32, pp. 11284–11287, 2014.

-
- [41] T. E. Williams, S. Nagarajan, P. Selvaraj, and C. Zhu, “Quantifying the impact of membrane microtopology on effective two-dimensional affinity,” Journal of Biological Chemistry, vol. 276, no. 16, pp. 13283–13288, 2001.
- [42] M. L. Dustin, L. M. Ferguson, P.-Y. Chan, T. A. Springer, and D. E. Golan, “Visualization of cd2 interaction with lfa-3 and determination of the two-dimensional dissociation constant for adhesion receptors in a contact area,” The Journal of Cell Biology, vol. 132, no. 3, pp. 465–474, 1996.
- [43] G. Kaplanski, C. Farnarier, O. Tissot, A. Pierres, A. Benoiel, M. Alessi, S. Kaplanski, and P. Bongrand, “Granulocyte-endothelium initial adhesion. analysis of transient binding events mediated by e-selectin in a laminar shear flow,” Biophysical journal, vol. 64, no. 6, pp. 1922–1933, 1993.
- [44] S. E. Chesla, P. Selvaraj, and C. Zhu, “Measuring two-dimensional receptor-ligand binding kinetics by micropipette,” Biophysical journal, vol. 75, no. 3, pp. 1553–1572, 1998.
- [45] M. L. Dustin, S. K. Bromley, M. M. Davis, and C. Zhu, “Identification of self through two-dimensional chemistry and synapses,” Annual review of cell and developmental biology, vol. 17, no. 1, pp. 133–157, 2001.
- [46] G.-K. Xu, J. Hu, R. Lipowsky, and T. R. Weikl, “Binding constants of membrane-anchored receptors and ligands: A general theory corroborated by monte carlo simulations,” The Journal of chemical physics, vol. 143, no. 24, p. 12B613_1, 2015.
- [47] B. Różycki, R. Lipowsky, and T. R. Weikl, “Segregation of receptor–ligand complexes in cell adhesion zones: phase diagrams and the role of thermal membrane roughness,” New journal of Physics, vol. 12, no. 9, p. 095003, 2010.
- [48] B. Różycki, T. R. Weikl, and R. Lipowsky, “Adhesion of membranes via switchable molecules,” Physical Review E, vol. 73, no. 6, p. 061908, 2006.
- [49] E. Reister, T. Bihl, U. Seifert, and A.-S. Smith, “Two intertwined facets of adherent membranes: membrane roughness and correlations between ligand–receptors bonds,” New Journal of Physics, vol. 13, no. 2, p. 025003, 2011.
- [50] J. Hu, G.-K. Xu, R. Lipowsky, and T. R. Weikl, “Binding kinetics of membrane-anchored receptors and ligands: Molecular dynamics simulations and theory,” The Journal of chemical physics, vol. 143, no. 24, p. 12B612_1, 2015.
- [51] T. R. Weikl, M. Asfaw, H. Kroboth, B. Różycki, and R. Lipowsky, “Adhesion of membranes via receptor–ligand complexes: Domain formation, binding cooperativity, and active processes,” Soft Matter, vol. 5, no. 17, pp. 3213–3224, 2009.

- [52] G. Woods, "Glycam web. complex carbohydrate research center, university of georgia, athens, ga. (<http://glycam.org>)," 2005-2018.
- [53] N. Kučerka, M.-P. Nieh, and J. Katsaras, "Fluid phase lipid areas and bilayer thicknesses of commonly used phosphatidylcholines as a function of temperature," *Biochimica et Biophysica Acta (BBA)-Biomembranes*, vol. 1808, no. 11, pp. 2761–2771, 2011.
- [54] N. Kučerka, Y. Liu, N. Chu, H. I. Petrache, S. Tristram-Nagle, and J. F. Nagle, "Structure of fully hydrated fluid phase dmpc and dlpc lipid bilayers using x-ray scattering from oriented multilamellar arrays and from unilamellar vesicles," *Biophysical journal*, vol. 88, no. 4, pp. 2626–2637, 2005.
- [55] J. F. Nagle, R. Zhang, S. Tristram-Nagle, W. Sun, H. I. Petrache, and R. M. Suter, "X-ray structure determination of fully hydrated l alpha phase dipalmitoylphosphatidylcholine bilayers," *Biophysical journal*, vol. 70, no. 3, pp. 1419–1431, 1996.
- [56] N. Kučerka, S. Tristram-Nagle, and J. F. Nagle, "Structure of fully hydrated fluid phase lipid bilayers with monounsaturated chains," *The Journal of membrane biology*, vol. 208, no. 3, pp. 193–202, 2006.
- [57] C. I. Bayly, P. Cieplak, W. Cornell, and P. A. Kollman, "A well-behaved electrostatic potential based method using charge restraints for deriving atomic charges: the resp model," *The Journal of Physical Chemistry*, vol. 97, no. 40, pp. 10269–10280, 1993.
- [58] T. R. Patel, S. E. Harding, A. Ebringerova, M. Deszczynski, Z. Hromadkova, A. Toga, B. S. Paulsen, G. A. Morris, and A. J. Rowe, "Weak self-association in a carbohydrate system," *Biophysical journal*, vol. 93, no. 3, pp. 741–749, 2007.
- [59] D. E. Koshland Jr, "The key–lock theory and the induced fit theory," *Angewandte Chemie International Edition in English*, vol. 33, no. 23-24, pp. 2375–2378, 1995.
- [60] J. L. Morrison, R. Breitling, D. J. Higham, and D. R. Gilbert, "A lock-and-key model for protein–protein interactions," *Bioinformatics*, vol. 22, no. 16, pp. 2012–2019, 2006.
- [61] T. R. Weikl and C. von Deuster, "Selected-fit versus induced-fit protein binding: kinetic differences and mutational analysis," *Proteins: Structure, Function, and Bioinformatics*, vol. 75, no. 1, pp. 104–110, 2009.
- [62] E. Schneck, *Generic and Specific Roles of Saccharides at Cell and Bacteria Surfaces: Revealed by Specular and Off-specular X-ray and Neutron Scattering*. Springer Science & Business Media, 2010.

-
- [63] D. Lingwood, B. Binnington, T. Róg, I. Vattulainen, M. Grzybek, Ü. Coskun, C. A. Lingwood, and K. Simons, “Cholesterol modulates glycolipid conformation and receptor activity,” Nature chemical biology, vol. 7, no. 5, p. 260, 2011.
- [64] A. Schlaich, B. Kowalik, M. Kanduč, E. Schneck, and R. R. Netz, “Physical mechanisms of the interaction between lipid membranes in the aqueous environment,” Physica A: Statistical Mechanics and its Applications, vol. 418, pp. 105–125, 2015.
- [65] J. N. Israelachvili, Intermolecular and surface forces. Academic press, 2011.
- [66] H. Krobath, B. Rózycki, R. Lipowsky, and T. R. Weigl, “Binding cooperativity of membrane adhesion receptors,” Soft Matter, vol. 5, no. 17, pp. 3354–3361, 2009.
- [67] R. Dasgupta, M. S. Miettinen, N. Fricke, R. Lipowsky, and R. Dimova, “The glycolipid gm1 reshapes asymmetric biomembranes and giant vesicles by curvature generation,” Proceedings of the National Academy of Sciences, vol. 115, no. 22, pp. 5756–5761, 2018.
- [68] R. Lipowsky, “Spontaneous tubulation of membranes and vesicles reveals membrane tension generated by spontaneous curvature,” Faraday discussions, vol. 161, pp. 305–331, 2013.
- [69] H. T. McMahon and J. L. Gallop, “Membrane curvature and mechanisms of dynamic cell membrane remodelling,” Nature, vol. 438, no. 7068, p. 590, 2005.
- [70] A. J. Garcia, M. D. Vega, and D. Boettiger, “Modulation of cell proliferation and differentiation through substrate-dependent changes in fibronectin conformation,” Molecular biology of the cell, vol. 10, no. 3, pp. 785–798, 1999.
- [71] M. P. Sheetz, D. P. Felsenfeld, and C. G. Galbraith, “Cell migration: regulation of force on extracellular-matrix-integrin complexes,” Trends in cell biology, vol. 8, no. 2, pp. 51–54, 1998.
- [72] A. J. Engler, S. Sen, H. L. Sweeney, and D. E. Discher, “Matrix elasticity directs stem cell lineage specification,” Cell, vol. 126, no. 4, pp. 677–689, 2006.
- [73] M. J. Paszek, N. Zahir, K. R. Johnson, J. N. Lakins, G. I. Rozenberg, A. Gefen, C. A. Reinhart-King, S. S. Margulies, M. Dembo, D. Boettiger, *et al.*, “Tensional homeostasis and the malignant phenotype,” Cancer cell, vol. 8, no. 3, pp. 241–254, 2005.
- [74] B. M. Gumbiner, “Cell adhesion: the molecular basis of tissue architecture and morphogenesis,” Cell, vol. 84, no. 3, pp. 345–357, 1996.

- [75] M. Goktas and K. G. Blank, “Molecular force sensors: from fundamental concepts toward applications in cell biology,” *Advanced Materials Interfaces*, vol. 4, no. 1, p. 1600441, 2017.
- [76] N. Walter, C. Selhuber, H. Kessler, and J. P. Spatz, “Cellular unbinding forces of initial adhesion processes on nanopatterned surfaces probed with magnetic tweezers,” *Nano letters*, vol. 6, no. 3, pp. 398–402, 2006.
- [77] M. Tanase, N. Biais, and M. Sheetz, “Magnetic tweezers in cell biology,” *Methods in cell biology*, vol. 83, pp. 473–493, 2007.
- [78] P. Honarmandi, H. Lee, M. J. Lang, and R. D. Kamm, “A microfluidic system with optical laser tweezers to study mechanotransduction and focal adhesion recruitment,” *Lab on a chip*, vol. 11, no. 4, pp. 684–694, 2011.
- [79] S. Romero, A. Quatela, T. Bornschlöggl, S. Guadagnini, P. Bassereau, and G. T. Van Nhieu, “Filopodium retraction is controlled by adhesion to its tip,” *J Cell Sci*, pp. jcs-104778, 2012.
- [80] E. Evans, K. Ritchie, and R. Merkel, “Sensitive force technique to probe molecular adhesion and structural linkages at biological interfaces,” *Biophysical journal*, vol. 68, no. 6, pp. 2580–2587, 1995.
- [81] J. Helenius, C.-P. Heisenberg, H. E. Gaub, and D. J. Muller, “Single-cell force spectroscopy,” *Journal of cell science*, vol. 121, no. 11, pp. 1785–1791, 2008.
- [82] J. Friedrichs, K. R. Legate, R. Schubert, M. Bharadwaj, C. Werner, D. J. Müller, and M. Benoit, “A practical guide to quantify cell adhesion using single-cell force spectroscopy,” *Methods*, vol. 60, no. 2, pp. 169–178, 2013.
- [83] K. Haase and A. E. Pelling, “Investigating cell mechanics with atomic force microscopy,” *Journal of The Royal Society Interface*, vol. 12, no. 104, p. 20140970, 2015.
- [84] S.-i. Hakomori, “Carbohydrate-carbohydrate interaction as an initial step in cell recognition,” *Pure and applied chemistry*, vol. 63, no. 4, pp. 473–482, 1991.
- [85] D. Spillmann and M. M. Burger, “Carbohydrate-carbohydrate interactions in adhesion,” *Journal of cellular biochemistry*, vol. 61, no. 4, pp. 562–568, 1996.
- [86] D. Spillmann and M. M. Burger, “Carbohydrate-carbohydrate interactions,” *Carbohydrates in Chemistry and Biology*, pp. 1061–1091, 2000.
- [87] A. Touhami, B. Hoffmann, A. Vasella, F. A. Denis, and Y. F. Dufrêne, “Probing specific lectin-carbohydrate interactions using atomic force microscopy imaging and force measurements,” *Langmuir*, vol. 19, no. 5, pp. 1745–1751, 2003.

-
- [88] Q. Lu, J. Wang, A. Faghijnejad, H. Zeng, and Y. Liu, "Understanding the molecular interactions of lipopolysaccharides during e. coli initial adhesion with a surface forces apparatus," Soft Matter, vol. 7, no. 19, pp. 9366–9379, 2011.
- [89] A. Atabek and T. A. Camesano, "Atomic force microscopy study of the effect of lipopolysaccharides and extracellular polymers on adhesion of pseudomonas aeruginosa," Journal of bacteriology, vol. 189, no. 23, pp. 8503–8509, 2007.
- [90] <http://parmed.github.io/ParmEd>
- [91] S. Jo, T. Kim, V. G. Iyer, and W. Im, "Charmm-gui: a web-based graphical user interface for charmm," Journal of computational chemistry, vol. 29, no. 11, pp. 1859–1865, 2008.
- [92] H. J. Berendsen, J. v. Postma, W. F. van Gunsteren, A. DiNola, and J. Haak, "Molecular dynamics with coupling to an external bath," The Journal of chemical physics, vol. 81, no. 8, pp. 3684–3690, 1984.
- [93] D. C. et.al., "Amber 2017," 2017.
- [94] J.-P. Ryckaert, G. Ciccotti, and H. J. Berendsen, "Numerical integration of the cartesian equations of motion of a system with constraints: molecular dynamics of n-alkanes," Journal of Computational Physics, vol. 23, no. 3, pp. 327–341, 1977.
- [95] C. Anézo, A. H. de Vries, H.-D. Höltje, D. P. Tieleman, and S.-J. Marrink, "Methodological issues in lipid bilayer simulations," The Journal of Physical Chemistry B, vol. 107, no. 35, pp. 9424–9433, 2003.
- [96] J. E. Basconi and M. R. Shirts, "Effects of temperature control algorithms on transport properties and kinetics in molecular dynamics simulations," Journal of chemical theory and computation, vol. 9, no. 7, pp. 2887–2899, 2013.
- [97] H. Binder and K. Gawrisch, "Effect of unsaturated lipid chains on dimensions, molecular order and hydration of membranes," The Journal of Physical Chemistry B, vol. 105, no. 49, pp. 12378–12390, 2001.
- [98] A. Filippov, G. Orädd, and G. Lindblom, "Influence of cholesterol and water content on phospholipid lateral diffusion in bilayers," Langmuir, vol. 19, no. 16, pp. 6397–6400, 2003.
- [99] M. D. Hanwell, D. E. Curtis, D. C. Lonie, T. Vandermeersch, E. Zurek, and G. R. Hutchison, "Avogadro: an advanced semantic chemical editor, visualization, and analysis platform," Journal of cheminformatics, vol. 4, no. 1, p. 17, 2012.

- [100] A. K. Rappé, C. J. Casewit, K. Colwell, W. Goddard Iii, and W. Skiff, “Uff, a full periodic table force field for molecular mechanics and molecular dynamics simulations,” Journal of the American chemical society, vol. 114, no. 25, pp. 10024–10035, 1992.
- [101] M. J. Frisch, G. W. Trucks, H. B. Schlegel, G. E. Scuseria, M. A. Robb, J. R. Cheeseman, J. A. Montgomery, Jr., T. Vreven, K. N. Kudin, J. C. Burant, J. M. Millam, S. S. Iyengar, J. Tomasi, V. Barone, B. Mennucci, M. Cossi, G. Scalmani, N. Rega, G. A. Petersson, H. Nakatsuji, M. Hada, M. Ehara, K. Toyota, R. Fukuda, J. Hasegawa, M. Ishida, T. Nakajima, Y. Honda, O. Kitao, H. Nakai, M. Klene, X. Li, J. E. Knox, H. P. Hratchian, J. B. Cross, V. Bakken, C. Adamo, J. Jaramillo, R. Gomperts, R. E. Stratmann, O. Yazyev, A. J. Austin, R. Cammi, C. Pomelli, J. W. Ochterski, P. Y. Ayala, K. Morokuma, G. A. Voth, P. Salvador, J. J. Dannenberg, V. G. Zakrzewski, S. Dapprich, A. D. Daniels, M. C. Strain, O. Farkas, D. K. Malick, A. D. Rabuck, K. Raghavachari, J. B. Foresman, J. V. Ortiz, Q. Cui, A. G. Baboul, S. Clifford, J. Cioslowski, B. B. Stefanov, G. Liu, A. Liashenko, P. Piskorz, I. Komaromi, R. L. Martin, D. J. Fox, T. Keith, M. A. Al-Laham, C. Y. Peng, A. Nanayakkara, M. Challacombe, P. M. W. Gill, B. Johnson, W. Chen, M. W. Wong, C. Gonzalez, and J. A. Pople, “Gaussian 03.”
- [102] J. Wang, W. Wang, P. A. Kollman, and D. A. Case, “Automatic atom type and bond type perception in molecular mechanical calculations,” Journal of molecular graphics and modelling, vol. 25, no. 2, pp. 247–260, 2006.
- [103] M. P. Allen and D. J. Tildesley, Computer simulation of liquids. Oxford university press, 2017.
- [104] C. W. Hopkins, S. Le Grand, R. C. Walker, and A. E. Roitberg, “Long-time-step molecular dynamics through hydrogen mass repartitioning,” Journal of chemical theory and computation, vol. 11, no. 4, pp. 1864–1874, 2015.

List of Figures

2.1	Structures of the simulated saccharides	12
2.2	Structure of the POPC lipid	14
2.3	Area per lipid of pure POPC in TIP3P and TIP5P waters	14
2.4	Electron density profiles for the pure POPC in TIP3P and TIP5P water models	15
2.5	Area per lipid as a function of the scaling factor	16
2.6	Electron density profiles as a function of the scaling factor	17
2.7	Structure of the glycolipid anchor	18
2.8	Illustration of the self-interacting single bilayer system	21
2.9	Structures of the lipid-anchored saccharides	22
2.10	Snapshot from the simulation of LeX in single- <i>cis</i> configuration	23
2.11	Two snapshots from the simulation of LeX in single- <i>trans</i> configuration at 5.5 nm and 7.5 nm local separations	24
2.12	Two snapshots from the ten-percent system of LeX at 5.5 nm (left) and 7.5 nm (right) separations	24
2.13	A snapshot from the double bilayer simulation	25
3.1	Structures of the soluble saccharides with dihedral definitions	27
3.2	The dihedral distributions of the soluble saccharides	28
3.3	Number of contacts as a function of time for two LeX saccharides in water	30
3.4	The average contact maps for the soluble saccharides	31
3.5	Probability distribution of the number of contacts and maximum number of contacts in a given bound interval as a function of the lifetime	32
3.6	Three-dimensional binding constant K_{3D} as a function of contact cutoff .	33

3.7	Relative frequencies of the contacts formed between saccharide residues	35
3.8	Spatial distributions of the soluble saccharides in bound states	36
4.1	The number of contacts as a function of time for the lipid-anchored LeX and Lac2	41
4.2	Probability distributions of the number of contacts as a function of number of contacts in single- <i>trans</i> system	42
4.3	Two-dimensional binding constant $K_{2D}^{trans}(l)$ as a function of local separation	43
4.4	Spatial distribution of the bound lipid-anchored saccharides in single- <i>trans</i> system	45
4.5	Average tilt angle for the bound lipid-anchored LeX and Lac2 as a function of local separation in single- <i>trans</i> system	46
4.6	Snapshots from the simulations of two lipid-anchored saccharides in <i>cis</i> -configuration	47
4.7	Number of contacts as a function of the time for the lipid-anchored LeX and Lac2	48
4.8	The probability distribution of the number of contacts and the maximum number of contacts in a given bound interval as a function of the lifetime	49
4.9	Two-dimensional binding constant K_{2D}^{cis} as a function of applied contact cutoff	50
4.10	Spatial distributions of the bound lipid-anchored saccharides in <i>cis</i> -configuration	51
4.11	Average number of contacts between lipid-anchored saccharide units in bound states	52
4.12	Snapshots from the simulations of 10% mol concentration of the lipid-anchored LeX and Lac2 in planar membranes	54
4.13	The number of <i>cis</i> - and <i>trans</i> -bonds as a function of time for the lipid-anchored LeX and Lac2	55
4.14	Two-dimensional effective binding constant $K_{2D}^{eff}(l)$ for the ten-percent simulations of the lipid-anchored LeX and Lac2	57
4.15	Average tilt angles for the lipid-anchored LeX and Lac2 as a function of local separation	58
4.16	Electron density profiles along the z axis for the ten-percent and single- <i>trans</i> lipid-anchored LeX and Lac2 systems	60

5.1	Last frame of the one of the apposing fluctuating membrane simulations .	66
5.2	The snapshots of the last frames for each run of the apposing fluctuating membrane simulations	68
5.3	The relative membrane roughness in apposing fluctuating membranes . .	70
5.4	The probability distribution of the local separation for the apposing fluctuating membranes	71
5.5	Probability distribution for the local separation of the bound states in apposing fluctuating membranes	73
5.6	Two-dimensional binding constant K_{2D} for the apposing fluctuating membranes	74
5.7	Average number density of the lipid-anchored saccharides as a function of local separation in apposing fluctuating membranes	76
6.1	Probability distributions for the z -extensions between the glycolipid linker and lipid head groups at 8.0 nm local separation	80
6.2	Schematic illustration of the force generation by the <i>trans</i> -binding of the lipid-anchored saccharides	81
6.3	Forces generated by the <i>trans</i> binding of the lipid-anchored LeX in single- <i>trans</i> configuration with different cutoff for the number of contacts as a function of the local separation	84
6.4	Probability distributions of the z -distance between the glycolipid linker and the center of mass of the lipid head groups as a function of local separation	85
6.5	Forces and energies generated by the <i>trans</i> -binding of the lipid-anchored LeX and Lac2 as a function of the local separation	87
6.6	Forces and energies for the ten-percent system as a function of local separation	88
6.7	Forces and energies for the bound states of the single- <i>trans</i> and ten-percent systems as a function of local separation	89
6.8	Pressure generated by the <i>trans</i> -binding of the ten-percent system as a function of local separation	90
A.1	Structure of the POPC lipid	94
A.2	Order parameters for the lipid head and tail of pure POPC	96
A.3	Mean-square-displacement vs. time as a function of scaling factor	97

A.4	Structure of the glycolipid linker	99
C.1	Spatial correlation function for the local separation as a function of the discrete increment in apposing fluctuating membranes	109
C.2	Time-correlation function for the local separation as a function of simulation time for the apposing fluctuating membranes	110

List of Tables

3.1	Binding constant for soluble saccharides	34
4.1	Average box height for the simulations	41
4.2	Two-dimensional binding constant $K_{2D}^{trans}(l)$ for the lipid-anchored LeX and Lac2 in single- <i>trans</i> system	43
4.3	Two-dimensional binding constants K_{2D}^{cis} for the lipid-anchored LeX and Lac2	52
4.4	Average box height for the ten-percent simulations	55
5.1	Length of ten independent trajectories for the apposing fluctuating membrane simulations	66
5.2	The average local separation and relative membrane roughness of the apposing fluctuating membranes	71
6.1	The calculated equilibrium length and the spring constant of the harmonic springs for the single- <i>trans</i> and ten-percent systems.	83
A.1	Lennard-Jones well-depth as a function of scaling factor	94
A.2	Calculated membrane properties as a function of the scaling factor	98
A.3	Original and recalculated partial charges (e^{-1}) for the glycolipid linker	100
B.1	Total simulation time and number of water molecules for saccharide simulations in water	105
B.2	Number of water molecules (n_w) for each local separation in single- <i>trans</i> simulations.	106
B.3	Number of water molecules (n_w) for each local separation in ten-percent simulations	107

Declaration of ownership

I declare that this thesis titled "Membrane Adhesion Mediated *via* Lipid-Anchored Saccharides" and the work presented in it are my own. I confirm that:

- This work was done wholly while in candidature for a research degree at the University of Potsdam;
- Where I have consulted the published work of others, this is always clearly attributed;
- Where I have quoted from the work of others, the source is always given. With the exception of such quotations, this thesis is entirely my own work.

Potsdam, 31.12.2018

Batuhan Kav